THE UNIVERSITY OF QUEENSLAND

Bachelor of Engineering Thesis

Design of Asymmetric Shape-Transition Hypersonic Inlets

Student Name: Reid JONES

Course Code: MECH4500

Supervisor: Dr. Rowan Gollan

Submission date: 27 October 2017

A thesis submitted in partial fulfilment of the requirements of the Bachelor of Engineering degree in Mechanical and Aerospace Engineering

UQ Engineering

Faculty of Engineering, Architecture and Information Technology

Abstract

Scramjet engines suffer performance penalties at off-design conditions, due to the fact that the engine is designed for one particular set of flight characteristics. Thermal compression has been suggested as one way of addressing poor off-design performance. For thermal compression to occur in the combustor, the incoming airflow must be of a non-uniform pressure distribution. This paper investigates the generation of a non-uniform compression field at the combustor entrance by designing an asymmetric inlet with uneven compression ratios.

A complicating factor is that scramjet engines must be carefully body-integrated onto the vehicle forebody to maximise air capture and reduce drag. Any attempt at designing an inlet suitable for thermal compression must body-integrated.

One challenge in designing an asymmetric inlet is the current selection of 3D surface modelling tools available to designers. The secondary goal of this project is to improve the current surface generation method for CFD analysis by identifying a new tool to carry out the design process. Ideally, the modelling process should be rapid and user-friendly. The tools selected for this project were 3DReshaper®, Blender™ and MeshLab.

This project follows through the design of an asymmetric inlet using a combination of these tools, with a view to providing a non-uniform pressure distribution at the combustor entrance. The ease and usability of the modelling method was evaluated, and found to provide no real improvement over the current method. One tool, Rhinoceros®, has been identified as having potential for future investigation, due to its mesh-to-NURBS surface conversion functionality.

The inlet design was tested in an Eilmer4 CFD simulation, and was found to be successful in generating non-uniform pressure distribution at

the outlet (Figure i). However, an unanticipated shock effect was noted in the inlet, which reduced the effectiveness of the non-uniformity. This effect was due to a shock reflection off the cowl closure point, indicating that a greater understanding of cowl placement is necessary when designing this type of inlet.

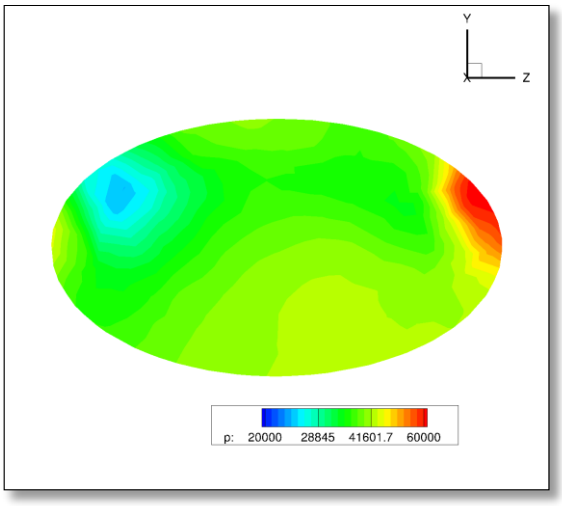

Figure i – Non-uniform pressure distribution at the inlet exit due to asymmetric inlet shape.

Several avenues for future research have been identified. Foremost is an investigation into the cowl closure behaviour contributing to the unwanted shock in the inlet. In addition, testing of new modelling techniques to overcome the problems identified with Blender™ and 3DReshaper® is recommended. Creating a stronger, quicker, easier design process will enable iterative designs to be created and assist in resolving the reflected shock issue. Once this has been completed, a full system analysis can be carried out to determine whether this type of thermal compression inlet has any positive effect on scramjet engine performance.

Acknowledgements

I cannot describe to you my sensations on the near prospect of my undertaking. It is impossible to communicate to you a conception of the trembling sensation, half pleasurable and half fearful, with which I am preparing to depart. […] I am practically industrious – painstaking, a workman to execute with perseverance and labour – but besides this there is a love for the marvellous, a belief in the marvellous, intertwined in all my projects, which hurries me out of the common pathways of men, even to the wild sea and unvisited regions I am about to explore.

~ Mary Shelley, *Frankenstein*

* * *

It ought to go without saying, but nevertheless,
I cannot overstate my gratitude for the utterly outstanding and generous wisdom and support of my thesis supervisor,
Dr. Rowan Gollan.
Without your knowledge and guidance, I would have been well and truly lost at sea.

I wish also to acknowledge the work of Mr. Jens Kunze for his invaluable assistance in preparing the CFD simulation for this project. Your contribution is very much appreciated.

Thanks to my friends, family and colleagues for their ongoing support.

And most of all, a million thanks to Ammy, for everything.

Table of Contents

List of Figures

List of Tables

Chapter 1

Introduction

1.1 Motivation

The University of Queensland's (UQ) Centre for Hypersonics is involved in designing and building scramjets for hypersonic flight testing. Due to the extreme pressure and temperature conditions encountered during hypersonic flight, scramjet engine inlets must necessarily be body-integrated to reduce external drag.

Currently, all known hypersonic inlets offer a uniform pressure distribution at the combustor entrance. Thus, engines are designed for one optimal design condition which meets the requirements of this pressure distribution. This offers challenges in operation over a range of flight speeds: the engine performs well at the design flight speed, but suffers degraded performance across other flight speeds.

One idea for improving engine performance across a range of flight speeds involves using Thermal Compression (TC). Thermal Compression introduces a non-uniform pressure distribution in the combustor inlet. Incorporating TC into a body-integrated inlet presents a challenge for designers, but one way of achieving this uneven flow field may be through asymmetric inlet design. An asymmetric inlet shape is expected to enforce unequal compression ratios onto the incoming air flow.

Since the concept was first presented by Antonio Ferri in the 1960s [1], little work has been done to investigate the efficiency of TC in a scramjet inlet. Some progress has been made in recent years with Mathew Bricalli's numerical study [2], but as yet no extensive simulations are known to have been attempted. It is hoped that using asymmetry and TC to generate a non-uniform pressure distribution will significantly improve engine performance over a range of flight speeds, at the expense of some top-end performance.

However, the task of generating an asymmetric inlet is replete with challenges. In large part, these challenges revolve around building a 3D surface model suitable for Computational Fluid Dynamics (CFD) analysis. CFD has become increasingly important in the engineering design process over the past several decades, thanks to ongoing advances in computer technology and processing power. This is especially true in cutting edge fields such as the aerospace industry, in which new designs routinely push the envelope, and real world testing becomes prohibitively expensive. The field of CFD continues to expand rapidly, allowing more and more innovative designs and simulations to be considered.

However, in order to take advantage of increasingly complex CFD analyses, surface models capable of supporting the analysis must be generated. Designers at the Centre for Hypersonics are able to create a point cloud describing an inlet shape [3], which can be converted into a surface, but the conversion process itself currently represents a significant bottle-neck in the process. Surface modelling tools in the CAD and animation families are not designed with CFD in mind, which makes modelling of complex surface shapes both labour- and time-intensive. Removal or streamlining of this bottle-neck would be expected to generate significant gains in productivity.

1.2 Project Goal

The primary aim of this project is to determine whether an asymmetric TC inlet can successfully produce a non-uniform pressure distribution at the combustor entrance, thus creating the conditions required for thermal compression in the chamber. If successful, this will pave the way for future studies to be conducted to determine whether such a thermal compression engine can offer any improvements in scramjet performance.

To achieve this goal, an asymmetric 3D TC inlet will be modelled. The modelling process informs the secondary goal of the thesis, which is to develop a rapid, user-friendly surface-building process which removes the current design bottle-neck. The inlet shape will be generated using the university's existing Shape-Transitioning InLEt (Stile) software [4]. A 3D modelling

software package must then be identified which can rapidly and accurately convert the point cloud into a CFD-suitable surface.

Once such a surface has been generated, the pressure distribution in the inlet will be analysed through a CFD simulation to determine its suitability in creating the preconditions for TC combustion in the chamber.

1.3 Thesis Outline

The dual aims of this thesis – developing a body-integrated TC inlet for CFD analysis, and developing a user-friendly 3D modelling method in support of the primary goal – will be carried out systematically. The paper opens with a discussion of the background and relevant literature, then carries on to the development of the tools necessary to achieve the goals. Once the toolbox has been filled, allowing a satisfactory TC inlet to be built, an analysis of the inlet will be carried out. The logical flow of the paper encourages the reader to develop a deeper understanding of the pre-existing situation, the steps taken to improve it, and the implications of the project outcome. A brief chapter breakdown is provided below:

Chapter 2 *Background*

An overview of the literature introducing the array of concepts relevant to this project. The chapter begins with an overview of scramjets and scramjet inlet design, then elaborates on the concept of thermal compression in scramjet engines. The discussion then moves to the relevance of CFD in the contemporary design environment, and finally to the field of 3D modelling and surface topology.

Chapter 3 *Project Aim*

The project aim explicitly sets out the primary and secondary goals of the project – developing a body-integrated TC inlet, and a user-friendly method of modelling this inlet – and how those goals will be achieved.

Chapter 4 *Development of a Body-Integrated TC Inlet*

Chapter 4 begins with a discussion of the greater conceptual fundamentals of the TC design challenge, sets up the related design decisions and scope, and presents the process used to develop an asymmetric TC inlet point cloud.

Chapter 5 *Rapid, User-Friendly 3D Modelling Process*

Chapter 5 is specific to the 3D modelling tools selected for use in the surface modelling stage of the project. It presents a detailed methodology related to building a CFD-appropriate surface in 3DReshaper®, Blender™ and Meshlab.

Chapter 6 *CFD Analysis of Asymmetric TC Inlet*

Chapter 6 outlines the process used to carry out a CFD analysis on the asymmetric 3D surface, as well as the simulation flow conditions.

Chapter 7 *Results*

Chapter 7 presents the results of the work described in Chapters 4, 5 and 6. Results include discussions on the effectiveness of the surface generation tools and processes, as well as the performance of the TC inlet design.

Chapter 8 *Conclusion and Recommendations*

The conclusion summarises the findings of the report, and discusses avenues for further research.

Chapter 2

Background

An asymmetric scramjet inlet design may have implications for improving overall scramjet performance. By taking advantage of thermal compression (TC) in the combustor, asymmetry may broaden the operational envelope of a scramjet vehicle. In addition, since scramjet engines are necessarily integrated into the vehicle itself [3, 5, 6], having high-performing asymmetric engines may open up the field to allow consideration of more novel aircraft designs. The expanding fields of Computational Fluid Dynamics (CFD), and other simulation and design tools, present opportunities for a more thorough study on optimal aircraft design. Successful asymmetric inlet design may allow these design studies to progress without the limitations imposed by symmetrical body-integrated engines. This chapter explores the background information relating to scramjets (Section 2.1), inlet design (Section 2.2), thermal compression (Section 2.3), CFD for scramjet design (Section 2.4) and 3D surface modelling (Section 2.5).

2.1 Scramjets: An Introduction

In the limited space available here, it is not possible to provide a complete history of the supersonic combustion ramjet (scramjet), but Curran's review of the first forty years of scramjet research [7] provides a thorough grounding for the interested reader. The following highlights were heavily informed by his work.

The concept of supersonic ramjet combustion has been around since as early as 1946, with Roy's proposal to add heat to a supersonic stream by means of a standing wave [7, 8]. The concept of supersonic combustion was explored in 1957 by MacKay and Weber [9], whose study became one of the theoretical cornerstones of scramjet research [7]. In the late 1950s and early 1960s, this concept had been demonstrated experimentally by Nicholls [10]

and Gross & Chinitz [11], who both succeeded in showing stabilised detonation waves in supersonic airstreams.

The field of scramjet research opened up considerably during this time period, with research in inlet, combustor and outlet configurations coming out of McGill University [7, 12], and broad-scope theoretical studies from Johns Hopkins [13]. Of particular note is the work of Antonio Ferri, who verified that steady combustion had been attained in a Mach 3.0 stream [7, 14].

At hypersonic speeds (above approximately Mach 5), scramjets demonstrate a much higher specific impulse than rockets (Figure 2.1). Unlike rockets – which carry their own oxidiser on board, accounting for a sizeable proportion of their total launch mass – scramjets are air-breathing engines. This largely accounts for their improved performance, and presents an opportunity to revolutionise current access-to-space methods by operating as second-stage launch vehicles for small payloads [15] .

One of the benefits of a scramjet as a second-stage vehicle is that, as an aircraft, rather than a rocket, a scramjet-powered flight vehicle has control surfaces for manoeuvrability. This gives it the potential to be operated with

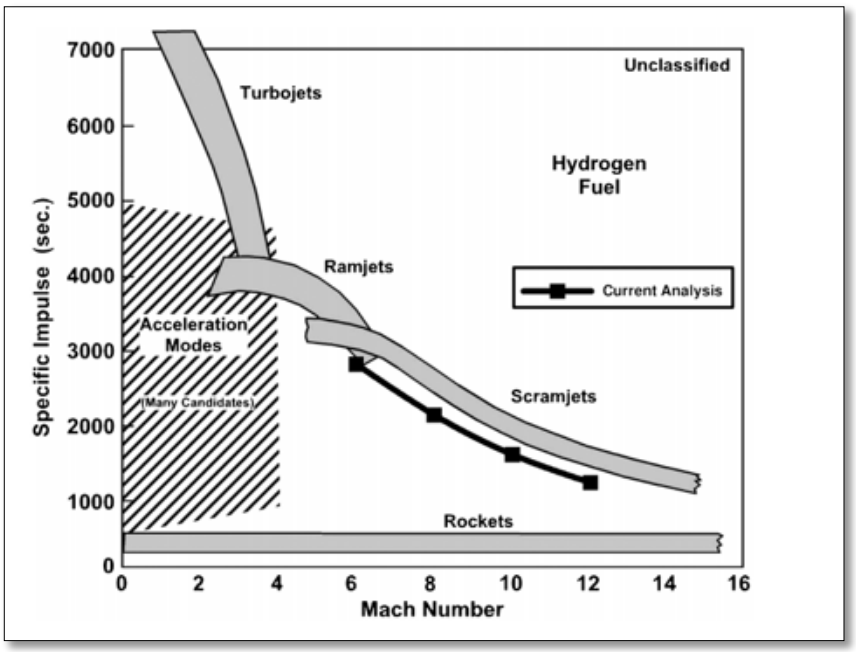

Figure 2.1 – Comparative specific impulses of various aircraft. For flight conditions within the hypersonic region, scramjets demonstrate a higher specific impulse than conventional rockets. Image sourced from Sutton & Biblarz (2011) [16].

trajectory and landing control [17] (see Creagh [18] for a discussion of the stability and manoeuvrability of the HyShot vehicle). A 1960s design trade-off study by Allen [19] found that a reusable second-stage scramjet concept showed promise in terms of fuel efficiency and payload-carrying capability.

Despite this, scramjet technology remains experimental. The first confirmation that scramjets were capable of producing more thrust than drag came from UQ in 1995 [20], which opened the research field to further development of full flight testing. The first successful supersonic combustion test flight was carried out by the university's HyShot programme in 2002, with further HyShot testing being carried out until 2007 [21]. Following on from HyShot, the new Hypersonic International Flight Research and Experimentation (HIFiRE) programme (a joint venture between the United States Department of Defence and Australia's Defence Science and Technology Group (DSTG)) has carried out a series of scramjet flight tests between 2009 and the present [22]. Several other international programmes, such as NASA's Hyper-X and Fastt projects also continue to work on experimental scramjet design [23-25].

2.2 Scramjet Inlet Design

Early hypersonic engine concepts, such as NASA's 1960s Hypersonic Ramjet Experiment (HRE) (Figure 2.2), built on existing ramjet theory by using axis-symmetric, circular cross-section engines [26], which were intended to be mounted to the airframe, a la existing ramjet technology [27]. As Heiser and Pratt comment, the drag caused by the struts used to mount the engines, was high enough to cancel out any thrust they generated [27].

Indeed, drag is a serious issue in scramjet design. At hypersonic speeds, it is preferred to fly at high altitudes to reduce drag, but as a scramjet is an air-breathing engine, the low density conditions at altitude can cause performance issues [27]. One proposed method of resolving this is the idea of enriching the oxygen flow from an on-board supply. This is a field of research in itself, and beyond the scope of this work, but Razzaqi's 2011 analysis [28] provides a good starting point for the interested reader.

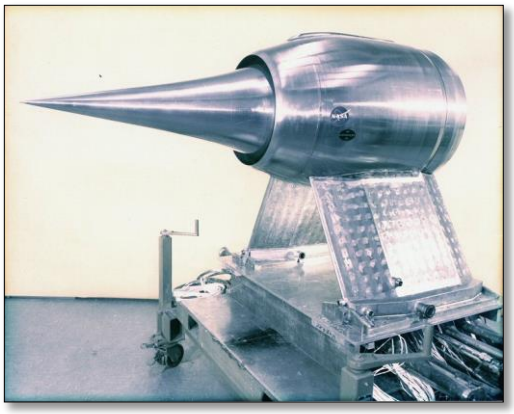

Figure 2.2 – NASA's HRE engine, an axis-symmetric, circular design intended to be mounted externally onto the vehicle frame. Image sourced from NASA – HRE (2017) [29].

A key solution to both problems of increased drag and reduced air intake was to build a thoughtfully body-integrated engine which featured less friction-generating surface area, and also took advantage of the geometrical features of the vehicle. In body-integrated engines, the forebody surface is used as a compression plane to increase the capture area of the intake and counter the decreased air density; the afterbody acts as a free expansion surface to expand the flow and generate thrust – and all this in addition to the reduction in drag gained by removing extraneous vehicle geometry [30].

Early designs consisted of a flat-bottomed vehicle capable of housing one or more rectangular engine modules [31], with transition to a rectangular combustor entrance [5]. Pinckney's rectangular-to-circular inlet study estimated that a circular combustor inlet area would use less material and, therefore result in weight savings of up to 28% [5]. Combustor efficiency studies in the 1960s by Hartill [32], Kiersey and Snow [33] and Kutshenreuter [34] found that circular and elliptical throat designs performed well, but contemporary computation tools were unable to handle the complex flow fields [6]. Pinckney [5] and Simmons and Wiedner [35] both made developments in rectangular-to-circular transition inlets using streamline tracing to define the flow field between the rectangular inlet and circular combustor interface.

Smart's 1999 study of a rectangular-to-elliptical shape-transition (REST) inlet [6] built upon that foundation, using streamline tracing and

cross-sectional lofting to define the flow characteristics. A streamline-trace was carried out on the inviscid flow field, which was then corrected to account for boundary layer conditions. Smart's design process involved first constructing a suitable compressive flow field, then defining a capture shape within that field, and finally performing a streamline trace to give the resultant surface shape of the capture area (Figure 2.3).

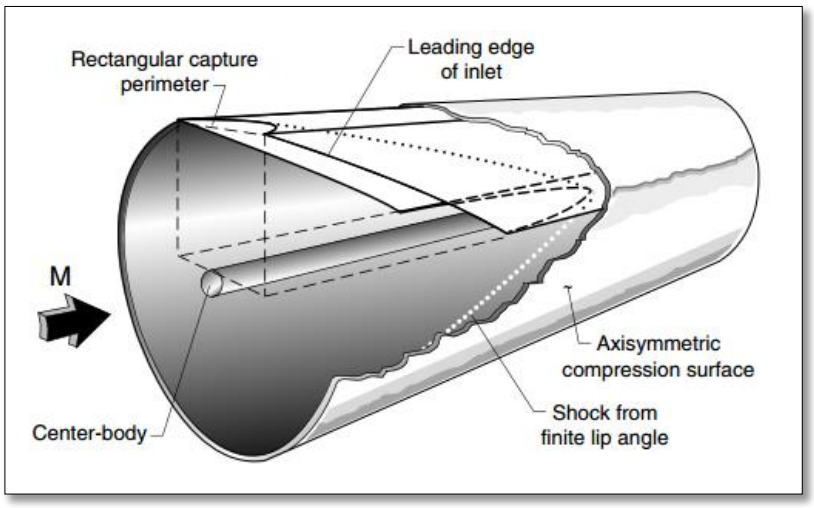

Figure 2.3 – Rectangular-to-elliptical shape transition (REST) inlet design methodology. The capture shape is placed in the compressive flow field, and a streamline trace is performed to determine the final shape. Image sourced from Gollan & Smart (2013) [3].

This process is itself performed for three different capture scenarios. First, a rectangular cross-section (designated by Smart as A) is traced to the cowl entrance. Second, shape B – similar to A, but with radiused corners – is traced. This provides the geometry of the cross-section at the cowl closure. And third, an elliptical cross-section of the same area as A is generated, designated shape C [6]. The resultant cross-sectional shape-transition inlet is shown in Figure 2.4. Once the cross-sectional geometry has been defined, the sections are joined by a mathematical lofting procedure. Finally, corrections are made to the model to account for viscous boundary layer effects [6].

The REST inlet was shown to work well on vehicles with a flat underside, as described above. However, new concept shapes in the scramjet design space suggest that a flat-bodied vehicle may not be the optimum shape,

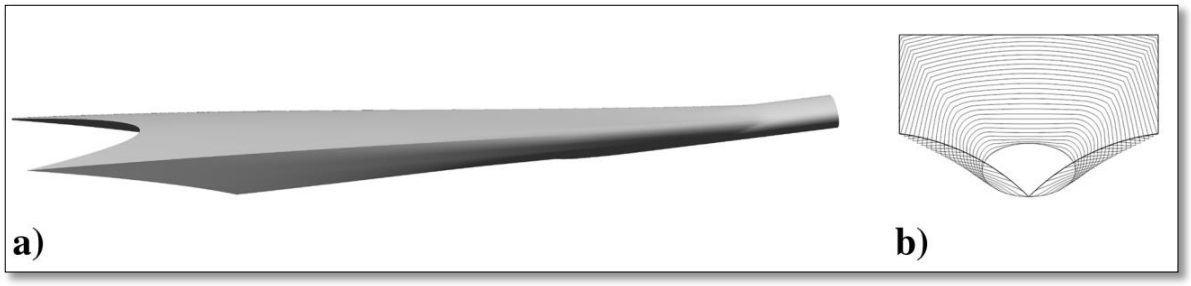

Figure 2.4 – REST shape-transition inlet showing a) perspective view, and b) cross-sections. Image sourced from Gollan & Smart (2013) [3].

after all [3]. Two ongoing design projects which have steered away from the flat-bodied design are NASA's Hyper-X research vehicle (Figure 2.5) [36] and UQ's SPARTAN concept vehicle (Figure 2.6) [37].

Figure 2.5 – NASA's Hyper-X research vehicle, using a so-called 'waverider' configuration. Image sourced from NASA – Hyper-X (2017) [36].

The Hyper-X programme is investigating the so-called 'waverider' body shape, which is preferred for its increased lift-to-drag (L/D) ratio (a side-effect of the 'wave' shape which produces an attached or nearly-attached bow shock, used to optimise flow) [38-41]. The disadvantage of the waverider shape is the requirement for a very flat, thin vehicle, which reduces its useful volume. Whilst this may not be of utmost important in flight testing and proof-of-concept studies, it becomes more so in terms of practical application of the vehicle as a payload-carrying tool [40].

UQ's SPARTAN concept scramjet is based on a conical-forebody design, akin to the model tested by Paull in 1995 [42]. The conical forebody generates shock waves which are captured and processed by a series of modular, symmetrical engines.

Figure 2.6 – UQ's SPARTAN concept scramjet, with a modular array of engines surrounding the conical body section. Image sourced from *Making Their Mach* (2017) [37].

Neither the Hyper-X nor the SPARTAN feature the flat underside described above, and, as such, a traditional REST inlet is not capable of handling the design challenges arising as a result [3]. For instance, as described by Gollan [3], generating modular REST engines to fit on a conical vehicle requires the airframe itself to be modified, and to therefore lose its conical shape. Additionally, the gaps between the engines allow airflow to be lost, and, worse, this airflow then contributes to external drag on the vehicle.

Gollan [3] has modified Smart's REST design process to enable use on a class of vehicle bodies without flat underside surfaces. Specifically intended for use on a conical vehicle, the Stile software [4] uses a truncated Busemann diffuser to shape the flow, allowing a shape-transition inlet to be formed which conforms to the conical airframe and which can be used to construct a modular array around the vehicle (Figure 2.7).

Shape-transition inlets are fixed-geometry, with the capture area ratios defined by the flow field characteristics and design flight Mach number [4]. As such, any variation in flight conditions causes changes to the flow field, resulting in a sub-optimal compression ratio, particularly at low flight Mach numbers. This has negative implications for low-speed ignition at the beginning of the second stage trajectory, as well as overall efficiency up to the

operational design point. Some attempt has been made to address this limitation by altering the position of the cowl closure point.

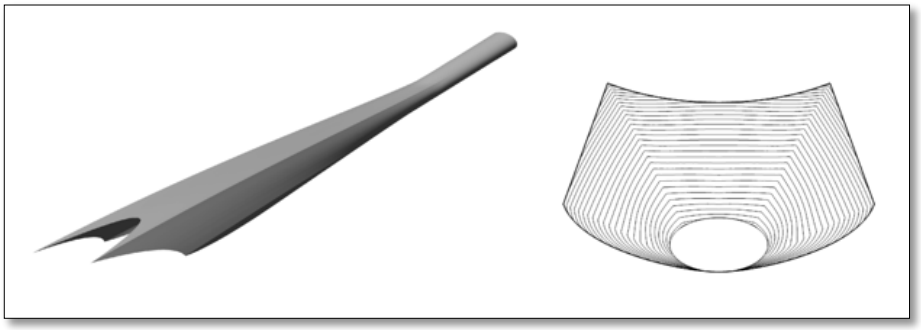

Figure 2.7 – Modified shape-transition inlet for a vehicle with a conical airframe. Image sourced from Gollan & Smart (2013) [3].

Trexler [43] noted as early as 1975 that the configuration of the cowl closure played a role in allowing some flow to spill out ahead of the closure point. This produced a variable-geometry-like behaviour in the fixed-geometry inlet and allowed for more efficient ignition and combustion at lower Mach numbers. Kumar [44] built upon this by experimenting with changes to the angle of sidewall sweep approaching the cowl closure point, and found that allowing more air to spill out ahead of the cowl could improve lower-speed performance. Sun [45], rather than focussing on the sidewall sweep, experimented with moving the location of the cowl closure point itself to facilitate air spillage at lower Mach numbers. This was also found to allow low-speed ignition, but resulted in unfavourable performance penalties at the design condition [46]. Inlet designs currently being developed at the Centre for Hypersonics make use of altered cowl closure points to improve low-Mach number performance[1].

Moving the cowl closure point does play a role in improving self-starting performance, but the question arises: is there a better solution? Two possible alternatives have been put forward, being variable geometry inlets, or a thermal compression design. These concepts will be discussed further in Chapter 2.3.

[1] From personal communication with members at UQ's Centre for Hypersonics.

2.3 Thermal Compression

Antonio Ferri became an early leader in the field of scramjet research during his time at General Applied Science Laboratories (GASL), where he carried out research in diffusive combustion [47], and, with Fox, turbulent mixing of air and fuel in the compression chamber [1]. One known issue with scramjets is that, due to the complex interactions during combustion, such as the very high speeds necessitating burn times in the order of one millisecond [48], they do not perform well over a range of flight speeds [49, 50]. This problem was identified early on, and Ferri, having already tackled the above fundamentals, turned his attention to finding a solution. His proposed solution [51] was to use three-dimensional engine geometry coupled with compression and combustion effects in a technique which went on to be called thermal compression (TC).

Ferri and Fox posited that a thermal compression engine required non-uniform flow to be delivered to the combustor [1]. In the engine, combustion occurring in a high-compression region is used to generate increased compression in an adjacent low-compression region. By taking advantage of the non-uniform compression field, engine performance is high even though compression from the inlet is low [2], because reducing the contraction ratio of the inlet reduces the spillage introduced by moving the cowl closure point. This combination improves performance due to the increased airflow capture, as well as improving the engine's starting characteristics due to the TC effect [52].

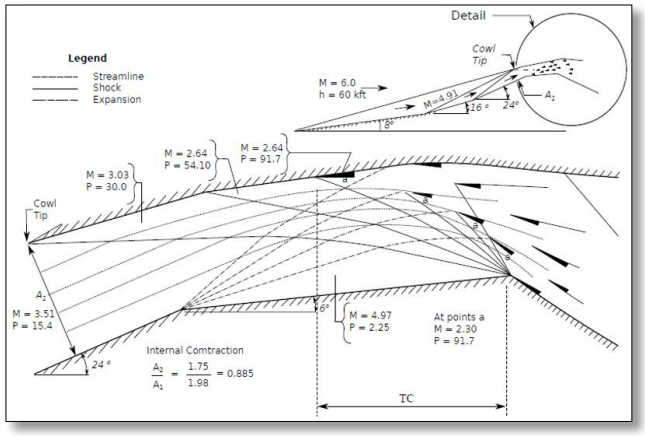

Figure 2.8 – A TC inlet, using non-uniform compression fields to ignite the engine, Ferri (1973) [51]. (Image Sourced from Bricalli (2015) [52].

Due to the complex fluid and combustion dynamics involved, and the limited computational power available at the time he presented this theory, Ferri's TC work remained largely untested. However, an analytical assessment by Billig et al in 1968 [53] went some way to validating the theory, and posited that a variable-geometry inlet operating with TC produced a higher specific impulse (I_{sp}) across the full range from Mach 5 to Mach 12, with performance showing a marked increase at the lower speed range (Figure 2.9).

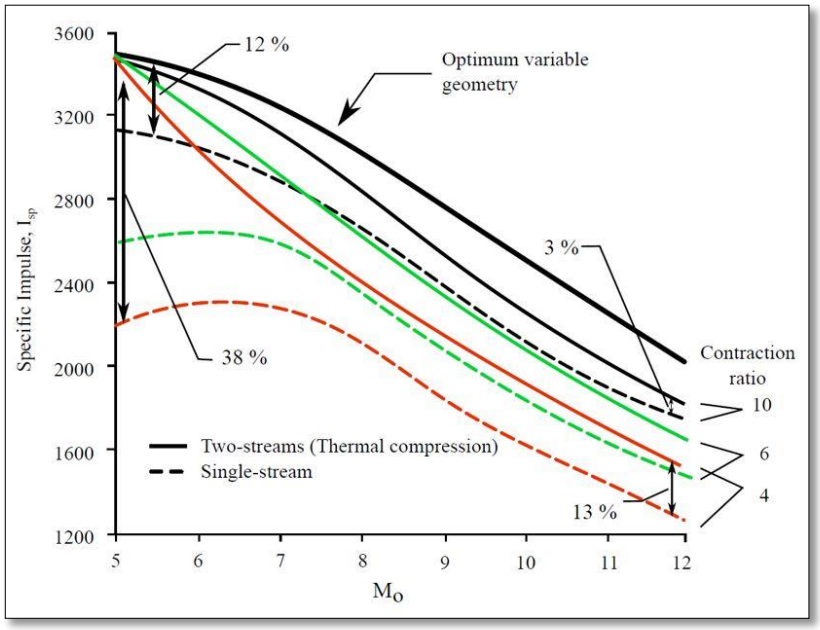

Figure 2.9 – Analytically derived solution for a variable-geometry inlet by Billig et al [53]. Performance at lower Mach numbers is significantly improved by the inclusion of TC.
Image sourced from Bricalli (2015) [52].

The complex flow interactions occurring in a variable-geometry TC combustor presented a significant road-block in carrying out further analysis, and the theory lay dormant for some time as others attempted to find solutions to the problem of efficient hypersonic flight over a range of Mach numbers. The US Air Force sponsored testing of a 'low-speed fixed geometry supersonic combustion ramjet' in 1961 which was designed to operate from Mach 3 to 12 [7], but no satisfactory solution was found. Similarly, NASA's National Aerospace Plane (NASP) programme, initiated in 1986 and terminated in 1993 due to budget considerations, was an attempt to design a single-stage-to orbit

vehicle capable of horizontal take-off, up to a flight Mach number of 25 [54]. More recently, France and Russia developed a partnership intended to design a varying-geometry vehicle capable of flight over a range from ~Mach 1.5 to Mach 12 [25]. The so-called Wide Range Ramjet (WRR) features mechanically moving inlet walls which alter the geometry to optimise air flow for varying flight speeds. However, challenges identified with the design include the extra weight added by the mechanical parts, as well as problems with moving the extremely hot surfaces during flight [25].

Recent advances in (CFD) have put Ferri's theory back on the table as a promising research prospect. In 2004, Li & Zhang carried out a theoretical validation of a 2-dimensional asymmetric nozzle [55], with further studies in asymmetric shock behaviour subsequently carried out [56-59]. In 2015, Bricalli presented a high-fidelity numerical study into TC, using CFD to model a 3D inlet [2, 52]. In the Bricalli study, a scramjet with an 18° high-compression ramp on one side of the inlet, combined with an 8° low-compression ramp on the other, were simulated. The compression generated by the low-compression ramp was insufficient to initiate combustion, which allowed the propagation of combustion from the high-compression side to be analysed (Figure 2.10). The study showed an improvement in specific impulse, which was attributed to the TC mechanism.

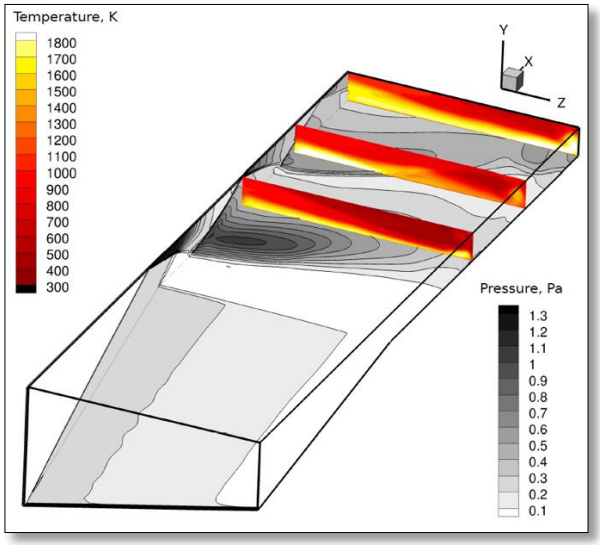

Figure 2.10 – Asymmetric 3D Thermal Compression inlet showing uneven pressure distribution and ignition propagation in the inlet. The inlet features an 18° high compression side and an 8° low compression side. Image sourced from Bricalli (2015) [52].

This result encourages further research to be carried out on a more realistic inlet design. The Bricalli inlet design was a basic rectangle-to-rectangle shape, bearing little resemblance to the REST inlets preferred for vehicle integration. In order to accurately validate the usefulness of TC in an asymmetric inlet, the most relevant next step for the Centre for Hypersonics is to design an asymmetric REST inlet building on the work of Smart (1999) [6] and Gollan (2013) [3], and integrating the uneven compression fields as explored by Bricalli (2015) [52]. Building an inlet of this design complexity is challenging, due to the limitations of CAD tools in creating surfaces for CFD analysis. The difficulties currently being faced in terms of geometry generation are further outlined in Chapter 2.5.

2.4 CFD for Aerospace Design

Successful flight engineering, since its infancy in Kitty Hawk, North Carolina, where the Wright Brothers launched the first ever flying vehicle, has been characterised by an adherence to rigorous design processes [60]. Shlien [61] argues that the Wright brothers' success over other contemporary aspirants was due in large part to the testing carried out during their design process. Their wind tunnel testing, although arguably so inefficient as to render the results irrelevant to full-scale designs, was one of the earliest documented cases of the rigorous testing of more than 200 aerofoil shapes, and is considered by some to have been a key turning point in aviation design processes [60, 62].

Wind tunnel testing and subsequent flight testing of aircraft remained the primary method of generating data regarding the efficiency of new vehicle designs throughout the twentieth century. Advances in digital technology from the 1940s to 1960s resulted in computer-based automated data-gathering using sensors to take key measurements, rather than relying on manual readings [63]. These technological advances improved the ability of designers to gather data, which subsequently allowed more and more ambitious projects to be undertaken. By 1969, wind tunnels capable of generating supersonic flow were in existence, but with increases in aircraft

capability also came increases in the cost of testing [64]. Advances in computer processing power, which occurred simultaneously with advances in aircraft design throughout the latter half of the twentieth century (Figure 2.11), enabled the fledgling field of numerical analysis to emerge.

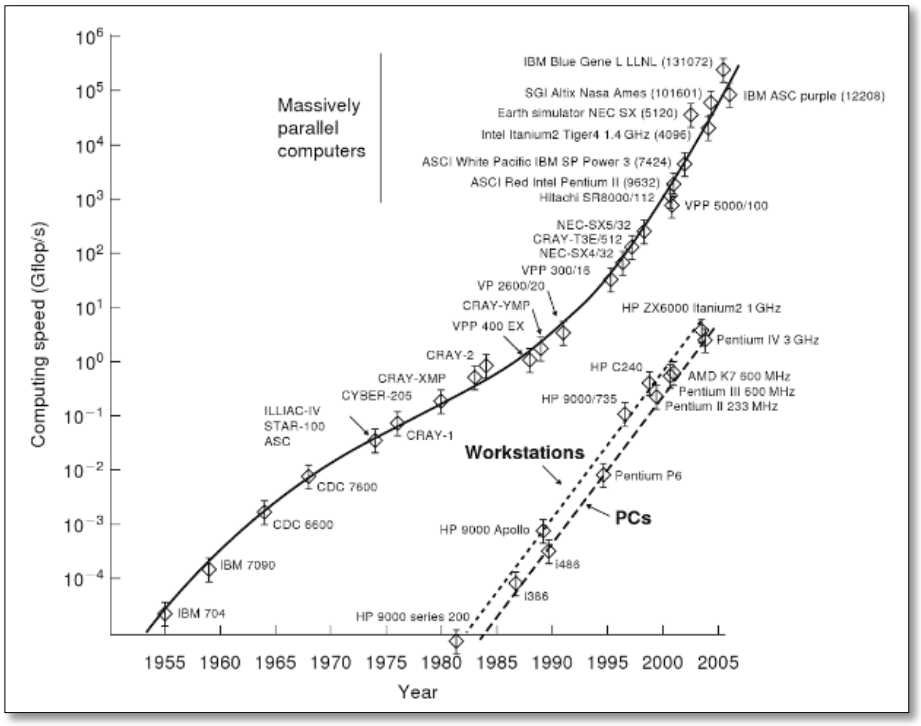

Figure 2.11 – Increase in computing power expressed on a logarithmic scale. Image sourced from Hirsch (2007) [64].

Computational Fluid Dynamics (CFD) with its iterative solutions to complex fluid flow problems, began to take shape. Hirsch [64], in his discussion of numerical computation, draws a link between the aforementioned improvements in computer power (leading to increased capability to solve the fluid flow equations) and a gradual shift away from ground testing in commercial aviation design. As shown in Figure 2.12, aircraft testing at the Boeing company over the past 35 years has heavily favoured CFD modelling. Indeed, between 1973 and 2002 the number of CFD simulations performed at the aircraft manufacturer's facility in Seattle increased by approximately 1000% [65]. Johnson [65] goes so far as to declare that the advances in CFD have led to a "paradigm shift in (…) vehicle design, analysis and support processes".

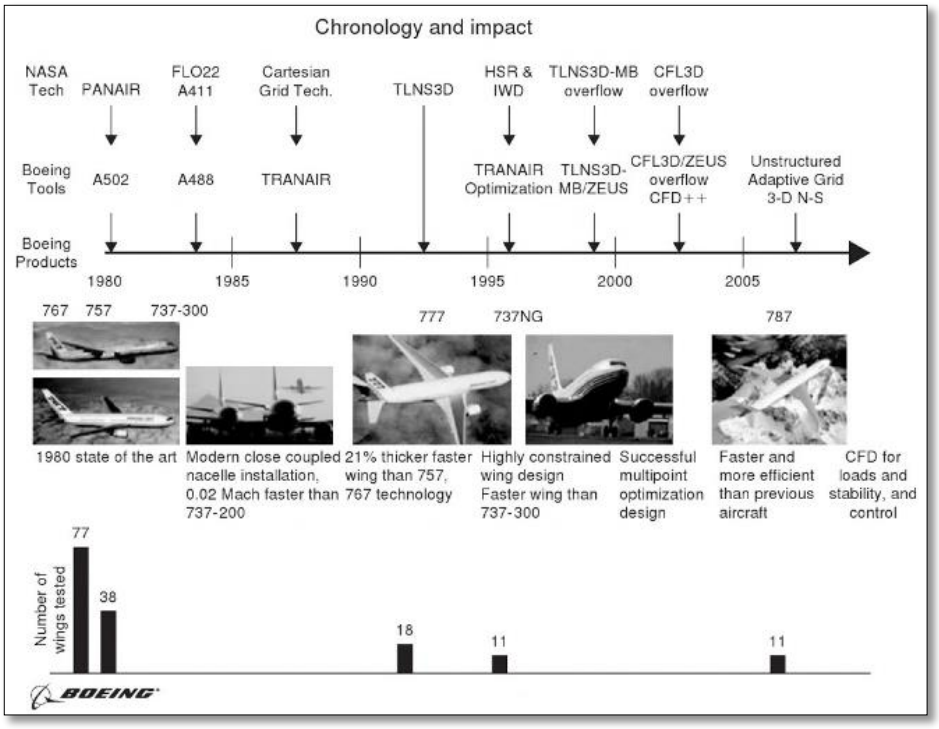

Figure 2.12 – Thirty years of CFD at Boeing, showing a reduction in dependence on wind tunnel testing. Image sourced from Hirsch (2007) [64].

With the development of numerical models capable of dealing with hypersonic flow conditions [66], CFD simulation of scramjet inlet designs is becoming increasingly reliable [67]. Faced with the limitations of ground-based testing, where models can only be subjected to high hypersonic flows in a shock tube for durations in the order of milliseconds [48], and flight testing, which is prohibitively expensive, CFD simulation has the potential to revolutionise hypersonic vehicle design as it has already revolutionised conventional aircraft design.

UQ's Centre for Hypersonics has developed software that enables a user to design a body-integrated scramjet inlet relevant to the desired operating conditions. The Stile program [4] generates a point cloud which can then be modelled into a surface appropriate for CFD analysis, but the transformation from a point cloud to a useful surface is currently subject to a bottle-neck in the process. Currently, a CAD user must visually analyse the automated surface output, correct issues with smoothing, and then apply real-world features to the model. For each new design concept, processing of

the point cloud may take in the order of weeks to complete. This places restrictions on the ability to compare design ideas or optimise solutions, as each new design iteration must be individually processed.

Where in the past, the limitations on CFD were largely based on limitations in computational power, in this application, it is the design process itself which is the limiting factor. In order to remove the bottle-neck, a new solution is required which can provide rapid, automated (or semi-automated) processing from the Stile point cloud to a surface suitable for CFD analysis.

2.5 3D Surface Modelling for CFD

2.5.1 Current Processing Method

The software currently being used to post-process the point clouds is Dassault Systems® CATIA™ [68]. Once processed, the output is exported to Pointwise® CFD mesh generation software [69]. Whilst CATIA™ is recognised as an industry standard in aerospace design, having been operational in the industry for almost 40 years [70], it has been found to be unsuited to the task of generating the type of surface required for a shape-transition scramjet inlet.

The Stile point cloud is imported into CATIA™ so that a surface can be generated from the points. The surface must be given real-world material properties (such as bluntness and thickness) to enable a high-fidelity CFD analysis to be carried out. However, importation of the point cloud results in a warped representation of the surface geometry, which must then be manually corrected. Depending on the complexity of the surface, and the corrections required, pre-processing may take in the order of weeks for each design iteration. As a result, the search has begun for a design tool capable of:

- Accepting point cloud geometry,
- Smoothing the surface without generating unwanted artefacts, and
- Applying real-world features.

Furthermore, these actions should be automated or semi-automated, and should result in output that is CFD-ready.

The challenges in the current processing method instigated the search for a new design tool, with designers taking the opportunity to explore a wider

field of tools than is traditionally used in engineering design applications. Rather than focussing exclusively on CAD tools, the question has been broadened to ask if there may be tools used in other industries that are well suited to producing CFD-suitable surfaces.

2.5.2 An Introduction to CAD and 3D Modelling

Computerised 3D design programs are often split into two main categories: CAD/CAM programs used in design and manufacturing industries, and artistic or animation programs used primarily in the film and gaming industries [71, 72]. Whilst the software packages used in each sector may share some common features, their development occurred independently of each other, and to some extent, they have remained independent over the years [71].

Computer Aided Design, or CAD, has its roots in the discovery that computers could generate vectors to represent data visually. This knowledge first made its appearance in the field of machine tooling, when, in 1949, John Parsons created the first numerically-driven milling machine, which was used to manufacture the complex swept-wing panels of the new Lockheed bomber [73]. Building on this foundation, in 1957, Patrick Hanratty developed 'Pronto', a numerical tooling program, which utilised a punch-card control system for production manufacturing equipment [74]. Ivan Sutherland, in his 1963 PhD thesis, built on the idea of using a computer to generate complex vectors, and developed the world's first CAD program, Sketchpad. Sketchpad responded to a light pen used to draw directly onto the computer monitor, generating lines the computer recognised as vectors, and was able to reproduce and plot complex figures based on these inputs [75]. In 1971, Hanratty returned to the spotlight on his production of the first commercially available CAD/CAM program, called 'Adam'. Many modern CAD programs have their roots in the code written by Hanratty for Adam, leading to his informal title as 'the father of CAD/CAM' [74].

Meanwhile, computerised 3D modelling first appeared in the 1960s, when the first computer-generated human figure was created by William Fetter. The so-called 'Boeing Man' (created for use in the aircraft

manufacturer's in-house design and training films) heralded the beginning of modern 3D modelling [76]. In their broad introduction to the field, Foster and Halbstein note that this technology was first adopted by the entertainment and computer game industries. As more specific industry applications appeared, 3D modelling techniques branched out to address these new needs. The three major areas which currently compose the field of '3D modelling' are Photogrammetry, Computer Vision, and Surface Topology and Retopologising [71].

2.5.3 Photogrammetry

Photogrammetry is a process in which data about shape or surface topography is gathered from images (or, more recently, remote sensing technology) with the aim of creating 3D representations of the visual surface. Whilst early photogrammetry was predominantly related to geology and topography [77], developments over the past 20 years have led to a broadening of applications to include areas as diverse as quality control, gaming, emergency management and cultural heritage conservation [78]. Once the data has been acquired, the subsequent processing is intended to build and render the object in as much realistic detail as possible. In other words, the key to successful photogrammetry is to have highly accurate computer vision and image recognition capabilities which can resolve intricate detail, and then to generate a surface or model which is explicitly faithful to the original real-world model [79].

Photogrammetry is not of immediate interest to this project, as the Stile point cloud has already been generated, leaving no requirement for this type of point acquisition. Similarly, the surface rendering is of no importance, as the relevant material properties will be applied to the model during the CFD analysis itself. However, there may be some value in assessing the methods used in photogrammetric post-processing.

A developing application in photogrammetric post-processing is so-called 'Reverse Engineering', which is the process of reconstructing, in loose terms, a 'useful' output by simply photographing and post-processing the object. What is defined as a 'useful' output appears to be dependent on the

individual application. In many cases, the output is used in an additive manufacturing process such as 3D printing. Examples of areas where this output may be considered useful include the preservation of artistic and cultural heritage [80-83], developing innovative medical breakthroughs [84, 85], and microscopic part development [86].

Of more interest to this project are the early stages of research being carried out in part development. Some reverse engineering tools such as Resurf [87] and 3DReshaper® [88] include automatic mesh-to-polynomial remodelling tools, which allow a part to be photographed, digitised, and converted into a CAD-quality part from which manufacture-standard working drawings may be created. (See Section 2.5.5 – Topology and Retopology for more on mesh and polynomial surface representations.) This mesh-to-polynomial conversion is a potentially useful tool in designing an asymmetric inlet.

2.5.4 Computer Vision

Computer vision relates to the ability of software to autonomously read and identify features of a digital image using information gathered from the pixels of the image [89, 90]. That is, it aims to program computers to be able to 'see' and respond autonomously to what they have seen. In 1963, Roberts introduced the concept of programming a computer to construct a 3D model from a 2D photograph [91]. Building on Roberts' work, in 1979, David Marr introduced a three-phase approach to computer vision which started by building a 2D sketch, followed by a 2.5D representation (a viewer-oriented image showing depth perception markers), and finally a 3D model, from a digital image [92]. In spite of initial estimates that having a computer see and interpret images would be simple, it is now widely acknowledged to be a surprisingly complex and difficult field to crack open [90]. In more recent years, computer vision technology has been more widely harnessed, appearing as embedded tools on platforms as diverse as mobile phones, cameras and satellite GPS systems [93].

Computer vision is not immediately relevant to this project. The surface geometry has been generated precisely by the Stile tool, according to

the identified flow field conditions. It is possible that future iterations of a new type of design tool may make use of computer vision to "look" at a design proposal with the intention of optimising it, but that is, at best, a distant proposal, and beyond the scope of this study.

2.5.5 Topology and Retopology

Topology is concerned with generating the 3D model surface by creating a mesh representing the model's geometry. Retopology is the improvement of an existing mesh by cleaning it up [71]. The model itself is defined by a series of points in space, and it is the mesh which defines how those points are joined to create the surface. At its base level, topology is dependent on mesh generation, a relatively recent field of research which began to emerge in the 1970s. Cheng's discussion of Delaunay mesh generation [72] features a brief introduction to the history of generation techniques dating back to the 1970s. Some early advances in automatic unstructured grid generation were made in the early 1970s by Frederick [94] and George [95], but for the most part, unstructured grids remained experimental whilst triangulation became the predominant method, following Frey's 1991 study in mesh relaxation techniques [96].

Developments in meshing techniques were primarily carried out with a view to creating grids for finite element analysis (FEA) or CFD simulations. It wasn't until the late 1990s and early 2000s that 3D animation began to filter into the entertainment and video game industries, adding an extra field of interest to the development of meshing capabilities.

Rather than being focussed on accurate solutions to the governing equations of an FEA or CFD simulation, meshing in the entertainment industry is predominantly concerned with surface smoothing to create the desired visual characteristics of the model [97]. Animation programs make use of meshing and smoothing algorithms to build surface topology. The smoothness of the surface to be constructed is dependent on the fineness of the mesh: a finer mesh with smaller and more numerous polygons will create a smoother finish, but at the cost of higher computational requirements.

One way of reducing the computational requirements of mesh generation is to use a polynomial surface generation technique. Two of the most common surface generation algorithms are Bezier splines and non-uniform rational B-spline (NURBS) surfaces [98, 99]. These polynomial-based surfaces are less computationally expensive, but can be difficult to control, particularly at the interface between surfaces [100].

The output from the Stile software is a point cloud, which natively represents a polygon mesh surface model. Any attempt to create a polynomial-type surface would therefore require a conversion from polygons to, say, NURBS. Some animation software, such as Resurf for Rhinoseros® [101], 3DReshaper® [88] and Autodesk Maya® [102] facilitate conversion of polygons to NURBS surfaces; others, including Blender™, do not [98]. Conversion of the point cloud from mesh to NURBS offers a potential solution to the design challenge of creating an asymmetric inlet surface for CFD.

2.5.6 Summary of Useful Surface Modelling Tool Characteristics

Of the three surface modelling streams considered here, topology is of primary relevance to this project. The Stile tool outputs a set of discrete points which may be joined via a mesh structure to create a surface. It may be valid to leave it as a mesh and apply real-world features as-is.

Alternatively, the meshed surface representation may benefit from being converted to a NURBS or Bezier spline surface. If this is found to be the case, the photogrammetric post-processing, or Reverse Engineering tools may be of interest. In either case, any surface representation must be readable by the Pointwise® meshing software used for setting up the CFD analysis.

Chapter 3

Project Aim

The goals of this project can be broken into two key categories:

1. Body-Integrated Thermal Compression Inlet Investigation, and
2. Surface Modelling.

3.1 Body-Integrated Thermal Compression Inlet Investigation

The primary aim of this project is to develop a body-integrated thermal compression hypersonic inlet for preliminary feasibility testing. The purpose of this inlet design investigation is to determine whether an asymmetric inlet design can provide the necessary conditions for TC combustion in the chamber. For this project, the 'body-integrated thermal compression' characteristics will be incorporated by developing an asymmetric inlet for integration onto a conical forebody, and which generates non-uniform compression fields at the inlet entrance.

This will require some conceptual decision-making processes to be carried out, regarding the most suitable method of creating an asymmetric inlet. Concept and design choices may include questions such as:

- How do we choose the conditions which will define the two different halves of the asymmetric inlet? (Do we pick two different flight speeds? Do we pick two different compression ratios? If so, what flight speeds or compression ratios do we choose, and why?)
- Once the two halves have been defined, how do we ensure that they will align properly at the throat, which must maintain the correct elliptical shape to join with the combustor entrance? (Do we scale one side to match the other side, but try to trim the cross section to maintain the original area ratios? Do we scale, instead, using mass flow ratios? Do we use some other method

of scaling? Or do we simply try to join the two halves and force the output into the required elliptical shape?)

- In areas where the two halves do not match up properly, how do we decide which half should dominate the design? (Do we trim the high compression side down to match the low compression side, or do we build the low compression side up to match the high compression side, or do we attempt to find a happy medium?)

Depending on the responses to these questions, a re-evaluation of the Stile tool may be necessary, with a view to incorporating some scaling method into the design process.

Once the respective roles of Stile's point generation tool, and subsequent modelling operations have been evaluated, an asymmetric 3D surface will be modelled, and a 3D CFD simulation carried out in order to determine whether this type of inlet is capable of producing the non-uniform pressure field required for TC combustion at the throat. A determination will be made as to whether this line of inquiry should subsequently be pursued in more detail.

3.2 Surface Modelling

The surface modelling component of this project aims to deliver a solution to the design bottle-neck in the current pre-processing method. The sub-goals of the surface modelling component fall into five main categories:

1. Tool selection
2. Surface joining and smoothing
3. Application of real-world features
4. Process automation
5. Demonstration of robustness

3.2.1 Tool Selection

The Stile tool outputs only one half of an inlet surface. A full inlet can be built by mirroring the half-surface and joining the two halves together. However, creating an asymmetric inlet requires that the two halves of the inlet

will not be identical. The joining line between the two halves may not line up precisely, and it will be necessary to develop a method of smoothly integrating the halves to create a CFD-suitable mesh. This will require an investigation of various CAD and 3D modelling/animation software to find a fit-for-purpose tool.

3.2.2 Joining and Smoothing of the Surface

Once a suitable tool has been identified, it will be used to generate a smooth surface. One challenge previously noted in generating a surface from a point cloud is that CAD programs represent the surface absolutely faithfully, which can result in ripples and deformations on the surface caused by the discrete nature of the cloud. Any method used to create a surface should incorporate surface smoothing techniques, with the outcomes that:

- The surface is smooth and a viable candidate for meshing and CFD analysis; and
- Any smoothing processes do not result in unacceptable loss of data.

3.2.3 Application of Real-World Features

Once a smooth surface has been generated from the point cloud, the inlet should be further developed to incorporate real-world features such as material thickness and edge bluntness. These features can have a significant effect on the flow field behaviour [103], so any high-fidelity analysis should represent the built surface as closely as possible.

3.2.4 Automation

The ideal outcome of this project component would be a fully- or highly-automated process to convert the point cloud into a viable surface for CFD analysis. Such automation should incorporate joining, smoothing, application of real-world features and mesh clean-up in preparation for CFD grid processing.

If full automation is not possible, semi-automation or even a user-friendly manual process may be considered as an alternative. The key goal is

to have a system that is both rapid and user-friendly, and which incorporates a “hands-off” smoothing and surface generation process.

3.2.5 Demonstration of Robustness

An asymmetric shape-transitioning hypersonic inlet will be used as a case study in attempting to achieve the above goals. Should a solution be found which is capable of automated surface generation and smoothing, the method should then be tested on other geometries. The preferred outcome would be that the solution is found to be a robust general solution that may be applied to a variety of geometries with equal success.

3.3 Project Plan

The project plan below outlines the steps necessary to complete the goals in their entirety, although it is important to note that these goals are quite ambitious. It is anticipated that it may not be possible to fully realise some of them within the required time-frame. Given this understanding, priority has been given to the primary goal of developing and testing a body-integrated thermal compression inlet.

Project Plan:

1. Consider the design decisions and propose a method for defining, scaling and building the two halves of the asymmetric inlet.
2. Use the Stile software to generate an asymmetric point cloud, as per these design decisions.
3. Research and choose a CAD or 3D modelling tool and use it to build a smooth surface representation of an asymmetric inlet for CFD.
4. Run a CFD analysis on the surface to determine whether the asymmetric inlet demonstrates the pressure distribution characteristics necessary for thermal compression.
5. If it is determined that the asymmetric inlet is a good candidate for further study, move on to optimising and automating the surface-building process.

6. Test the robustness of the surface generation tool by using it to build a series of asymmetric inlets for high-fidelity testing.
7. Perform an analysis on the new family of asymmetric TC inlets to develop understanding of their capabilities, and provide recommendations for future concept development.

The methodology to be undertaken in this project may be divided into three major categories:

1. Development of an Asymmetric Thermal Compression Inlet
2. Development of a Surface Modelling Method
3. 3D CFD Analysis of Asymmetric Hypersonic Inlet

These steps are discussed in the following three chapters.

Chapter 4 begins with a discussion of the greater conceptual fundamentals of the TC design challenge, sets up the related design decisions and scope, and presents the process used to develop an asymmetric TC inlet point cloud.

Chapter 5 is specific to the 3D modelling tools selected for use in the surface modelling stage of the project. It presents a detailed methodology related to building a CFD-appropriate surface in 3DReshaper®, Blender™ and Meshlab.

Chapter 6 outlines the process used to carry out a CFD analysis on the 3D surface generated in Chapter 5, based on the point cloud developed in Chapter 4.

Chapter 4

Development of a Body-Integrated TC Inlet

4.1 Design Choices: Scoping the Problem

Before work may begin on designing an asymmetric TC inlet, it is necessary to address the design choices discussed in Chapter 3.1. There are two key decisions that need to be made.

1. How do we choose the conditions which will define the two different halves of the asymmetric inlet?
2. How do we ensure the halves will align properly at the throat, which must maintain the correct elliptical shape to join with the combustor entrance?

4.1.1 Defining the Conditions of Asymmetry

Two main options presented themselves as possible defining conditions for inlet asymmetry.

Firstly, do we design each inlet half for the desired upper- and lower-end flight Mach numbers? One of the scramjet limitations identified in the literature was poor off-design performance. If a scramjet is intended to be used as a second-stage access-to-space vehicle, it should be able to operate efficiently from the first-stage drop-off point (say, ~Mach 5) to the third-stage pick-up point (say, ~Mach 12). In this scenario, one option for designing an asymmetric engine may be to design one inlet half for Mach 5, and the other for Mach 12 flight conditions. This method presupposes that the intended flight mission details are known, which is limiting in a broad-scale feasibility investigation.

The second option was to choose the high-compression side for a known flight condition (say, Mach 12), and choose the low-compression side according to a desired relative compression ratio (CR). That is, if one was interested in testing a 30% difference in compression ratios between the high-

compression and low-compression sides, one could choose a known top end, and then design the bottom-end according to the required reduced CR. For instance, if a Mach 12 inlet has a CR of 17, a 30% reduced CR is 11.9. Thus, the low-compression side can be designed to provide a CR of 11.9.

Of these two options, the second option – choosing a desired reduction in compression ratio – was deemed to be a more versatile method for early-stage testing. Using this method, it is possible to set up a series of tests experimenting with a variety of reduced pressure ratios, investigate flow field behaviour, and address optimisation questions such as: 'What ratio of high-to-low CRs provides the best inlet efficiency?'.

Once TC inlets have been validated as useful using this process, further testing for specific top- and bottom-end flight conditions may be carried out for particular mission profiles, as required.

4.1.2 Scaling the Inlet Halves

The scramjet inlet must be designed bearing in mind the outlet conditions. The rectangular inlet transitions down to an elliptical cross-section at the throat, which is maintained along the isolator length to the exit (Figure 4.1). This elliptical outlet shape is essential in joining the inlet to the combustor, thus any potential inlet design must conform to this shape requirement at the exit.

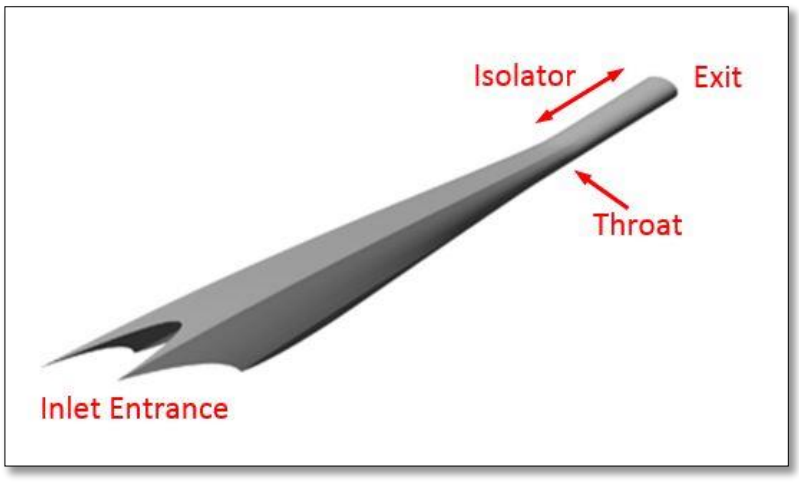

Figure 4.1 – The parts of a shape-transition hypersonic inlet.
Image sourced from Gollan & Smart (2013) [3], annotations added.

When designing the two halves of the asymmetric inlet, a restricting factor was that the aspect ratio of the elliptical throat was to be kept identical for each half. This presented a new design question for consideration: Given two dis-similar cross-sections featuring elliptical throats of different size but identical aspect ratio, how could a single ellipse of the correct aspect ratio be generated to join to the combustor without compromising the individual flow characteristics? Three options presented themselves for consideration:

1. Maintain the capture area ratio between the high- and low-compression sides,
2. Maintain the mass flow rate ratio between the high- and low-compression sides, or
3. Maintain the CR ratio between the high- and low-compression sides.

The point clouds generated by the Stile software feature elliptical throat shapes of the same aspect ratio, but the high-compression throat is larger than the low-compression throat (Figure 4.2(a)). In order to match the two halves, the low-compression side must be scaled up to match the high-compression side (Figure 4.2(b)). If one was interested in maintaining the capture area ratio between the two halves, it would then be necessary to alter the proportions of each half by moving the join away from the central axis (Figure 4.2(c)).

This requires first calculating the required area of each half, then determining how far across to move the joining axis, and then making a decision about whether this process is best done geometrically (in a CAD or 3D modelling program) or analytically (pre-surface generation, in the Stile software). Altering the two halves in this manner would be expected to potentially alter the compression ratios on each side of the join, and may make results difficult to quantify.

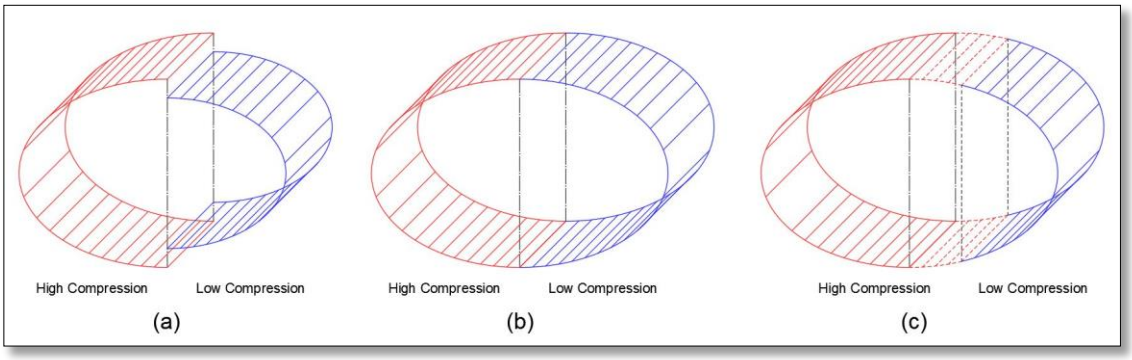

Figure 4.2 - Maintaining the capture area ratio requires scaling up the low-compression side (b), and extending the high-compression side past the point of symmetry (c) (not to scale).

Mass flow rate ($\dot{m}$) is one of the key parameters of interest in scramjet design. Assuming that the mass flow rate of air through the engine is much lower than that of fuel, the thrust generated by a scramjet is:

$$F = \dot{m}(v_{exit} - v_{\infty}) + (p_{exit} - p_{\infty})A_{exit}$$

Equation 4.1

It may be of interest to designers to maintain the $\dot{m}$ ratio between the two sides, in order to analyse the actual thrust generation capabilities of the individual halves of the engine. At this stage of the investigation, this was deemed unnecessary, and no plans for maintaining the $\dot{m}$ ratio were considered. However, this may be an area of interest in future studies if the concept of a TC inlet is found to be useful.

The compression ratio of each half of the inlet (from the inlet entrance to the throat) remains constant as the individual half is scaled up or down. Thus, in order to maintain the ratio of CRs between the two halves of the inlet, one half must simply be scaled to match the other at the throat. Matching the two halves presents an elliptical throat section of the correct aspect ratio, ready to be joined to the combustor entrance. This scaling may either be done geometrically (in a CAD or 3D modelling program) or analytically (pre-surface generation, in the Stile software.

Of these three potential scaling methods, the third option – maintaining the CR ratio between the two halves – was the simplest, and was considered the most relevant as a starting point. As in Chapter 4.1.1 (Defining

the Conditions of Asymmetry) a comparison of compression ratios was deemed to be a more versatile method for early-stage testing, as it is possible to set up a series of tests experimenting with a variety of reduced pressure ratios. It may become useful to revisit this decision in future investigations, if the TC inlet is found to be useful and further optimisation questions arise.

4.1.3 Simplifying the Problem: The Busemann Case

A shape-transition REST inlet for integration onto a conical vehicle features a complex set of geometries which make free-standing analysis of thermal compression more difficult. In particular, the corners in the rectangular segment can introduce unusual boundary layer effects, and the conical attachment point can make 3D surface generation more challenging. For this opening foray into TC inlets, a decision was made to simplify the initial analysis by carrying out the first tests on an asymmetrical Busemann inlet.

The REST inlet uses a truncated Busemann inlet to shape the flow [3], and applies Smart's REST methodology to create the rectangular-to-elliptical model [6]. For this project, the REST shape-transition process will be removed, and testing will be carried out on a truncated Busemann diffuser which transitions down to an elliptical throat shape (Figure 4.3). If an asymmetric Busemann inlet can be shown to demonstrate good thermal compression properties, it follows that the REST shape carved out of a Busemann stream field should demonstrate similar properties.

A further simplification made for this project was that the first CFD analysis was carried out on an infinitely thin surface, without any of the real-world features discussed in Chapter 3.2.3. The flow characteristics were applied to an inviscid flow, before boundary layer corrections had been applied. This was determined to be the most simple case study for analysing thermal compression in the inlet.

If this initial, simplified analysis shows successful generation of thermal compression in the asymmetric Busemann inlet, further work will be done to construct a body-integrated REST inlet, apply the appropriate boundary layer conditions, add the required real-world features.

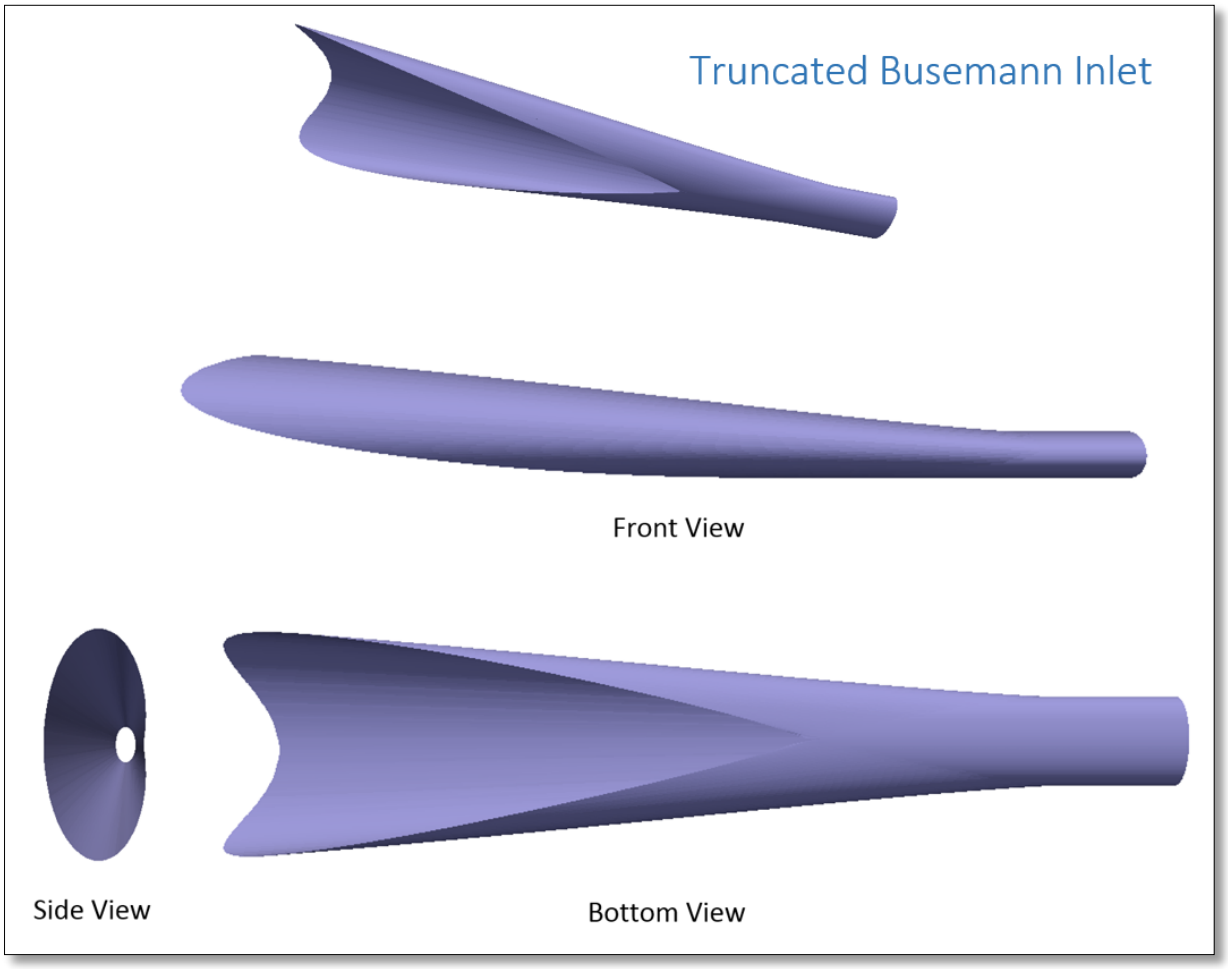

Figure 4.3 – Symmetrical truncated Busemann inlet. The asymmetric inlet design will be similar in concept to this symmetric version.

4.1.4 Final Design and Scoping Considerations

The concept of thermal compression in a scramjet inlet will be tested by designing an asymmetric inlet. An initial test case was chosen, wherein the high-compression side represents Mach 12 flight conditions. The low-compression side has been chosen to represent a 30% reduction in compression ratio from the high-compression side.

It should be noted that the hypersonic flight calculations to define the shock wave behaviour, inlet conditions and other associated flow conditions are beyond the scope of this project. The values used in this project have been pre-worked, and will be presented in their final form without derivation.

The flight conditions for this inlet are designed for Mach 12 flight of a vehicle with a 6° conical forebody, flying in air. The inlet entry conditions as processed by the forebody shock are:

p = 2247.2 Pa

T = 372.44 K

M = 9.1113

Gollan [3] notes that for a Mach 12 flight condition, the target pressure at the combustor entrance is ~50 kPa.

4.2 Developing an Asymmetric Thermal Compression Inlet

The methodology for creating an asymmetric thermal compression inlet was comprised of three main steps: building the high-compression side, building a low-compression side, and scaling the low-compression side to join up with the high-compression side. These steps are discussed in more detail below.

4.2.1 Building the High-Compression Inlet

The High-Compression (HC) side was treated as the primary reference for implementing the changes required to generate the 30% reduced compression (or Low Compression, or LC) field. Thus, it was constructed first.

1. **Calculate the diffuser characteristics**
   i. A new working directory was created for the High Compression inlet.
   ii. The diffuser set-up file, in this case named `diffuser_H.lua`, was copied into the HC working directory (see Appendix A).
   iii. The following was run from within the working directory:
   ```
   > stile build-Busemann-diffuser diffuser_H.lua
   ```
   This gave an output describing the characteristics of the high-compression Busemann diffuser (see Appendix B). It also generated the `sgl.dat` and `sgldisc.dat` files required for building the inviscid inlet surface.

2. Build the inviscid inlet surface

The following steps were also carried out in the HC working directory:

i. The inlet configuration file, in this case named `inlet.lua` (see Appendix C), was copied into the directory. The same inlet file was used for both the HC and LC sides.

ii. The `build-inviscid-surface.lua` script (available from the Stile repository) was run, as follows:

```
> ./build-inviscid-surface.lua
```

This command generated point data representing the inlet surface.

iii. The point data was converted into an .stl file capable of being interpreted by most CAD and 3D modelling programs, using the following:

```
> stile inlet2stl inlet.lua inviscid BusemannHC.stl
```

The output was an .stl file named `BusemannHC.stl`.

4.2.2 Building the Unscaled Low-Compression Inlet

1. Calculate the diffuser characteristics.

i. From Step 1 of Chapter 4.2.1, the compression ratio of the HC side was noted to be CR = 17. This CR was reduced by 30% to find the LC compression ratio (in this case CR = 11.9).

ii. A new working directory was created for the unscaled LC side.

iii. The diffuser set-up file was copied into the LC working directory and renamed `diffuser_L.lua`.

iv. In `diffuser_L.lua`, the characteristics which affect the CR are `M2` (the pre-shock Mach number), `M3` (the post-shock Mach number), `lip` (the truncation angle) and `r_cbody` (the radius of an imposed centrebody) [4]. Here, `lip` and `r_cbody` were left identical to the HC values, to preserve the elliptical shape of the inlet. Small modifications were made to `M2` and

M3, to apply slight changes to the CR. The Build Diffuser command was then run on this file:

```
> stile build-Busemann-diffuser diffuser_L.lua
```

This generated the diffuser characteristics for the LC side. The CR was noted, and more adjustments were made to M2 and M3 until the CR was reported back as 11.9 (see Appendix D). In this case, the values resulting in this CR were M2 = 5.87 and M3 = 5.39.

2. Build unscaled LC inlet

i. The inlet was built using:

```
> ./build-inviscid-surface.lua
```

This command generated point data representing the inlet surface.

4.2.3 Scaling the Low-Compression inlet

The processes laid out in Sections 4.2.1 and 4.2.2 can be used to generate two halves of an asymmetric inlet. However, as seen in Figure 4.4, the throat sections of the two halves do not meet up properly. A scaling process is required to join the throat sections together such that both the ellipse aspect ratio and HC-to-LC compression ratio is maintained.

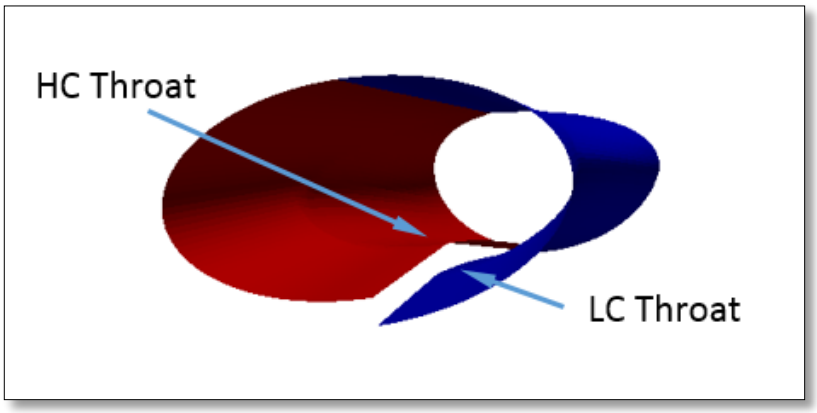

Figure 4.4 – A view from the combustor exit end of the joined HC and LC inlets, showing that the throats do not line up properly. A scaling process will be necessary to join the throats properly.

The scaling process was applied at the elliptical throat of the inlet. In order to scale the LC side to match the HC throat size and location, the throat

x-location (along the inlet's axis) and cross-sectional area were required. (The areas could be used to scale the size, as the aspect ratio had been kept constant in the `inlet.lua` file.)

Three scaling factors were required to size and locate the scaled inlet:

- sA: Throat area ratio = $\frac{HC\ Throat\ Area}{LC\ Throat\ Area}$,
- sL: Length scaling = $\sqrt{sA}$ (as the square root of the area is proportional to length), and
- DX: Throat position = $HC\ Throat\ Position - SL(LC\ Throat\ Position)$

These scaling factors, when applied together in the build file, have the cumulative effect of scaling the LC side up, and shifting its position so that the throat becomes a perfect ellipse located at the same x-position as the HC inlet throat.

1. **Gather inlet properties data to enable scaling of the throat**
   i. In the respective HC and LC working directories, the inlet properties were gathered using:
   ```
   > stile inlet-properties inlet.lua inviscid propertiesLC
   ```
   and
   ```
   > stile inlet-properties inlet.lua inviscid propertiesHC
   ```
   This generated an output file for each inlet summarising the inlet properties (see Appendix E). From these properties, information about the throat x-location and area were found for both inlets. This information is summarised in Table 4.1.

Table 4.1 – Summary of Inlet Scaling Factors

	Throat Area	Throat x-Loc	sA	sL	DX
HC Inlet	0.163588	6.393557	0.785925	0.886524	0.732064
LC Inlet	0.208147	6.386168			

2. **Modify the `build-inviscid-surface.lua` script to incorporate the scaling functions.**
   i. A new working directory for the scaled inlet was created. The `build-inviscid-surface.lua` script was copied into the

new working directory, and modified to include the scaling factors. (See Appendix F for the portion of script used to scale the inlet. This portion was inserted after Line 245 in the `Streamline Tracing` block. The scaling script was written by thesis supervisor Dr. R. Gollan.)

ii. The `diffuser_L.lua` and `inlet.lua` files were copied into the scaled working directory. The diffuser characteristics were generated:

```
> stile build-Busemann-diffuser diffuser_L.lua
```

and the scaled inlet surface built:

```
> ./build-inviscid-surface.lua
```

iii. Finally, the inlet data points were converted into an .stl file called `BusemannLC.stl`:

```
> stile inlet2stl inlet.lua inviscid BusemannLC.stl
```

Using the steps outlined in Chapter 4.2, a high-compression and low-compression inlet were developed which met at the throat, having a shared elliptical cross-section of the correct aspect ratio (Figure 4.5). However, the other surface edges did not meet (Figure 4.6). Chapter 5 will discuss the process of selecting and using a 3D modelling tool to join the two dissimilar halves as one smooth inlet surface.

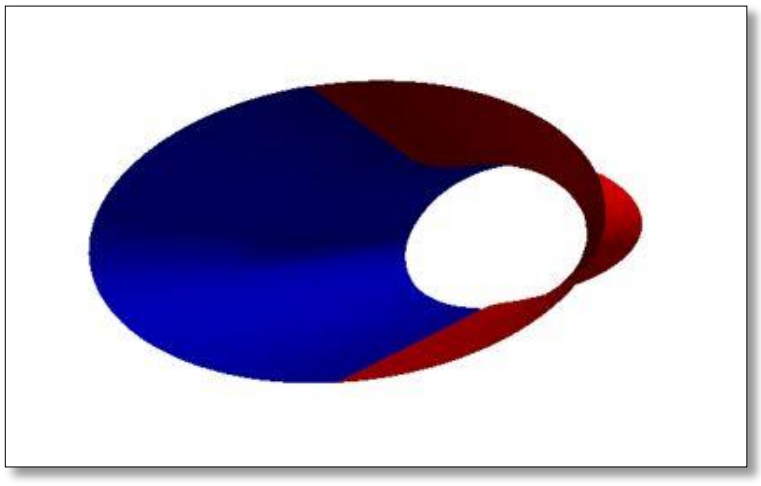

Figure 4.5 – A view from the combustor end showing the two scaled halves joined at the throat.

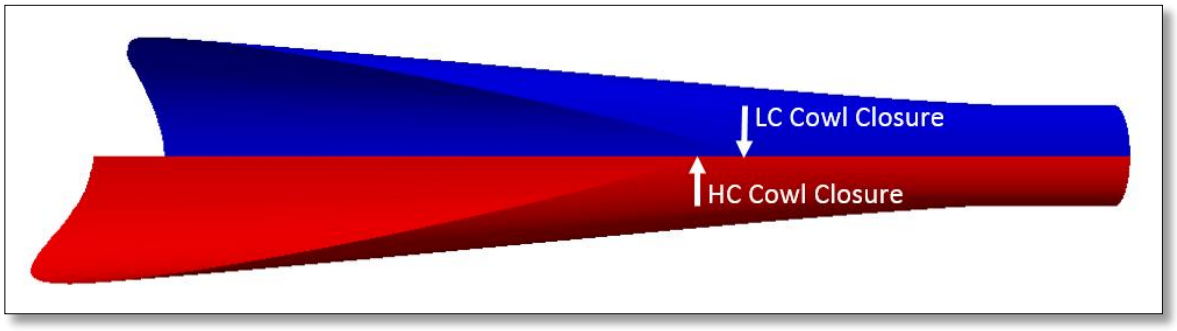

Figure 4.6 – Bottom view of the joined halves, showing significant discrepancies at the inlet entrance and cowl closure regions.

Chapter 5

Rapid, User-Friendly 3D Modelling Process

Chapter 4 introduced the design concepts and scoping decisions related to the development of a TC inlet, and presented the methodology for designing the base point cloud for an asymmetric inlet. In order to test this design concept, it becomes necessary to construct a 3D surface model for CFD analysis. This leads in to the secondary project aim: developing a rapid, user-friendly modelling approach with a view to removing the existing design bottle-neck.

This chapter turns to the selection of an appropriate design tool, and the specific processes used in those tools. The discussion specifically relates to the design tools 3DReshaper®, Blender™ and MeshLab, although some of the processes and concepts may prove relevant in the wider field of 3D modelling.

5.1 Developing a Surface Modelling Method

Development of a 3D modelling process consisted of first researching available products to determine which were suitable for this application. Then a decision was made about which product(s) to use. Finally, a surface blending together the HC and LC sides was created.

5.1.1 Choosing a Software Package

There is a vast array of 3D modelling software available on the market. Each bundle is designed to cater to a specific niche, and many of them overlap. The first step in selecting the most appropriate software was to identify the software requirements for this project. A wish-list of the software features was composed and divided into essential and preferred capabilities (Table 5.1). Each feature was given a weighting according to its importance, where 3 was most important and 1 least important.

Table 5.1 – Essential and Preferred Software Capabilities

	Weighting	Essential	Preferred
Thickness & bluntness modifiers	3	✓	
Smoothing & surface options	2	✓	
Pointwise® compatible output	3	✓	
Linux compatible	1		✓
Scriptable	2		✓
Open source or freely available	2		✓
Mesh-to-NURBS conversion	2		✓

With the desired functionality identified, a wide net was cast on internet forums and Google searches to identify firstly what software existed, and secondly, whether it was suited to purpose. It was not feasible to present an evaluation of every available piece of 3D modelling software, but Appendix G presents a filtered-down comparison of the "most likely" candidates, as decided based on a subjective reading of forums, reviews and user manuals.

A decision matrix was constructed using a numerical scale, where 2 (green) indicated that the software met the requirement well, 1 (orange) that it somewhat met the requirement, and 0 (red) that it did not meet the requirement at all. A selection of candidate software packages was collated, inspired by a series of blog posts comparing the best 3D modelling tools [104-110], followed by independent research of the suggested tools. Any software that failed to meet one or more of the essential requirements was disqualified; the remaining software was evaluated according to the weighting system. The results of the decision matrix are summarised in Table 5.2. Blender™ was chosen as the new design tool due to its high score.

Table 5.2 – Summary of Decision Matrix Results

Software Package	Score	Software Package	Score
Blender™	28	Onshape	21
Maya®	27	Moment of Inspiration	20
Meshmixer	27	ZBrush	19
Rhinoceros®	26	Sketchup	15
3ds Max®	26		

During the course of this project, no tool was found which was capable of adequately converting the inlet surfaces to NURBS, so the surface construction was carried out using mesh tools. The final asymmetric surface was constructed using a combination of 3DReshaper® and Blender™, with the final .stl export being sent out from Blender™. However, the exported mesh had some errors which were not visible to the eye, and the binary .stl format was not readable by Pointwise®. Therefore, the final surface was pre-processed for gridding in MeshLab to fix the errors and allow the export of a non-binary .stl file.

Blender™ is installed with a default user interface which is not ideal for the purposes of this project. Before undertaking any work in Blender™, the user interface was customised to provide more relevant working conditions. In addition, Blender's™ working interface is more complicated than many other CAD/modelling tools. Chapter 5.1.2 outlines the process of customising the Blender™ user interface, and provides an introduction to its basic operation. Chapter 5.1.4 outlines the attempted process of converting the mesh object to a NURBS surface in 3DReshaper®. The process of constructing the asymmetric inlet surface using meshing tools will be presented in subsequent sections.

5.1.2 An Introduction to the Blender™ User Interface

Customising of the Blender™ user interface was primarily related to the start-up conditions. The default setting is to open with three objects already in the work area: a light source, a camera and a cube. Upon opening,

these items were deleted from the workspace, and the settings saved to default (`Ctrl+U`) such that the program would then open by default to a blank workspace. This became particularly important in when automating the Blender™ actions in Python™ (see Chapter 5.3).

Blender™ has six operating modes, the most relevant of which to this project were `Object Mode`, `Edit Mode` and `Sculpt Mode` (Figure 5.1). `Object Mode` was used to make changes to the object on a macro scale, such as applying surface features. `Edit Mode` was used to make modifications to the underlying mesh. `Sculpt Mode` was used to smooth the mesh. In order to use Blender's™ features, it is important to be working in the appropriate mode. Many of the commands used in Blender™ are most accessible through shortcut keys. With these shortcuts, it is also important to be working within the appropriate mode.

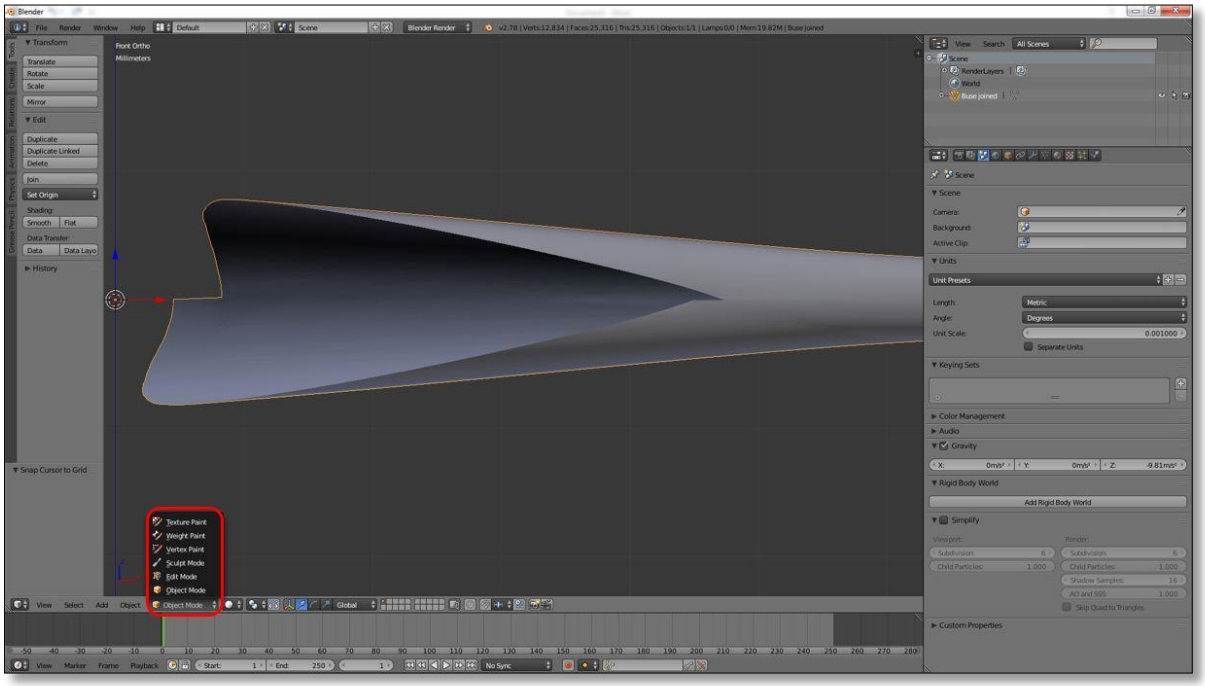

Figure 5.1 – Blender's™ User Interface. The operational modes most relevant to this project are Object Mode, Edit Mode and Sculpt Mode.

5.1.3 Joining the High- and Low-Compression Surfaces

The two surfaces were joined in 3DReshaper®. The joining process is outlined below.

1. The two surfaces were imported (`Main menu > Import Mesh(es)`) (Figure 5.2).
2. One of the meshes was mirrored about the z axis, so that the two meshes formed the approximate inlet shape (`Transform > Symmetry`, axis directions x = 0, y = 0, z = 1) (Figure 5.3).

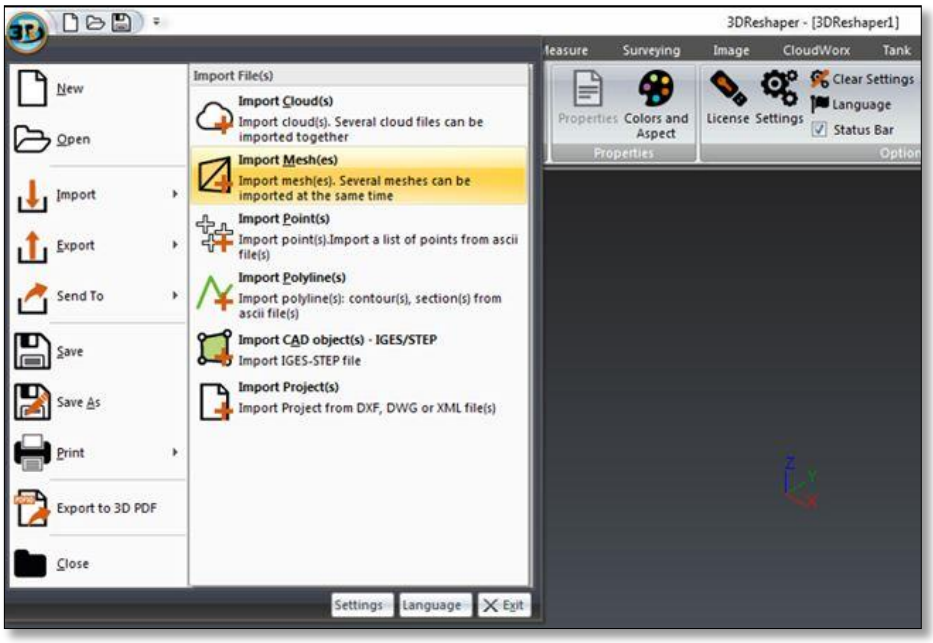

Figure 5.2 – 3DReshaper®: Import Meshes

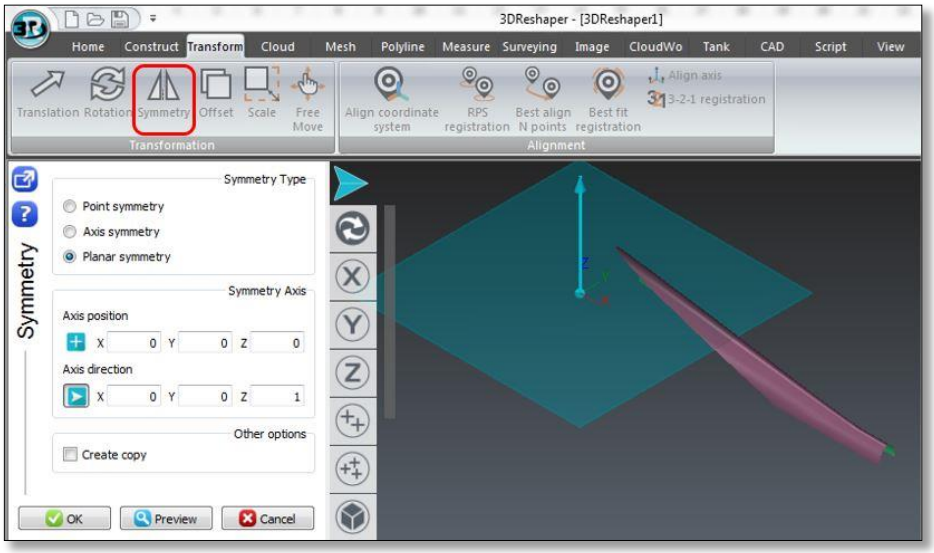

Figure 5.3 – 3DReshaper®: Mirror-image one half of the inlet

3. The top seam was joined using the `Join` tool (`Mesh > Join 2 Contours`) (Figure 5.4), as follows:

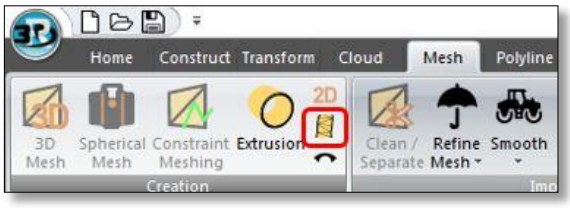

Figure 5.4 – 3DReshaper®: Join 2 Contours

i. The first half and second half were selected. In the `Irregular Contours` dialogue box, 'Make restriction' was chosen. This resulted in one of the halves was being outlined yellow, and the other in pink.

ii. On the pink half, the start- and finish-points of the first edge were selected. The red line representing the desired joining edge was then selected. The command was completed by pressing `Enter`.

iii. The same process was carried out on the second half to select the edge to be joined to (Figure 5.5).

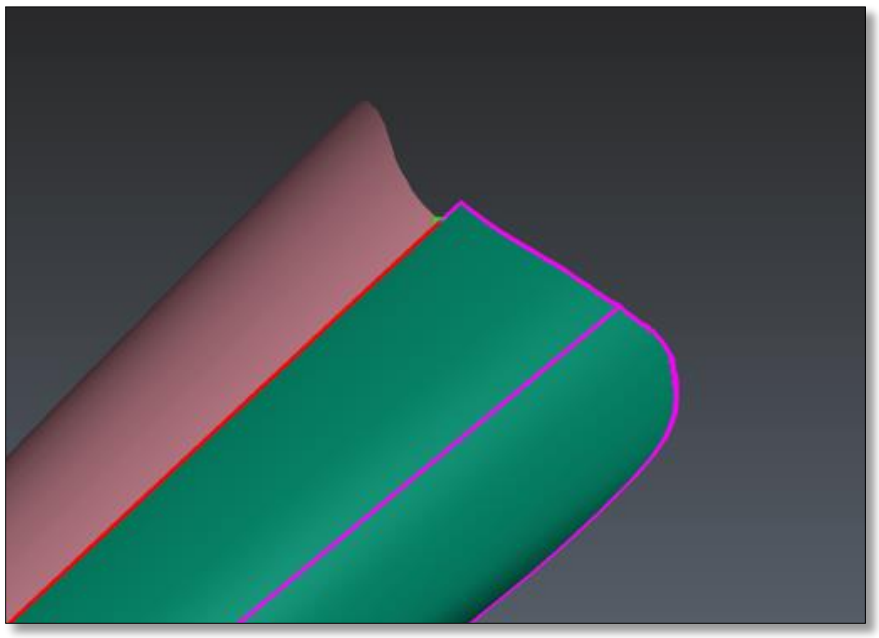

Figure 5.5 – 3DReshaper®: Select the two lines to be joined.
Join the long edge to the end-point of the short edge.

iv. The process was completed by selecting 'OK, Exit' on the `Join 2 Contours by Surface` control panel (Figure 5.6). A new surface was formed, joining the halves together (Figure 5.7).

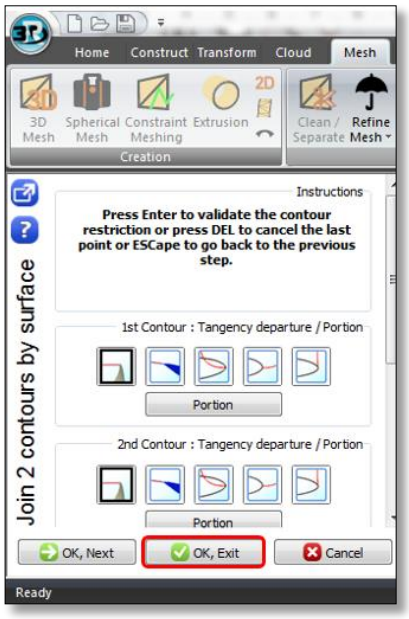

Figure 5.6 – 3DReshaper®: Finalise the joining process by selecting 'OK, Exit'.

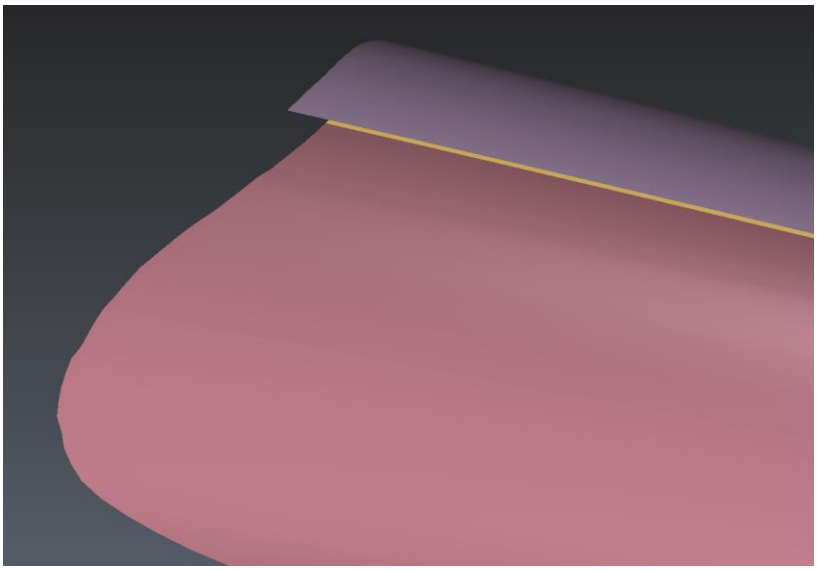

Figure 5.7 – 3DReshaper®: A new surface now joins the two halves.

v. The borders were merged to create a single mesh by selecting `Mesh > Merge Common Borders` (Figure 5.8).

Figure 5.8 – 3DReshaper®: Group the two sides into a single mesh.

5.1.4 Mesh-to-NURBS conversion in 3DReshaper®

3DReshaper® was chosen as a potential software primarily for its mesh-to-NURBS conversion capabilities. Once the two halves had been joined, an attempt was made to convert the surface into a NURBS surface for further modification (attempts were also made to convert the individual halves before joining). The process is outlined below:

1. A set of radial control polylines was created along the length of the inlet (`Polyline > Radial Sections`), spaced 10° apart around the central axis. The inputs for the `Radial Sections` command are shown in Figure 5.9.

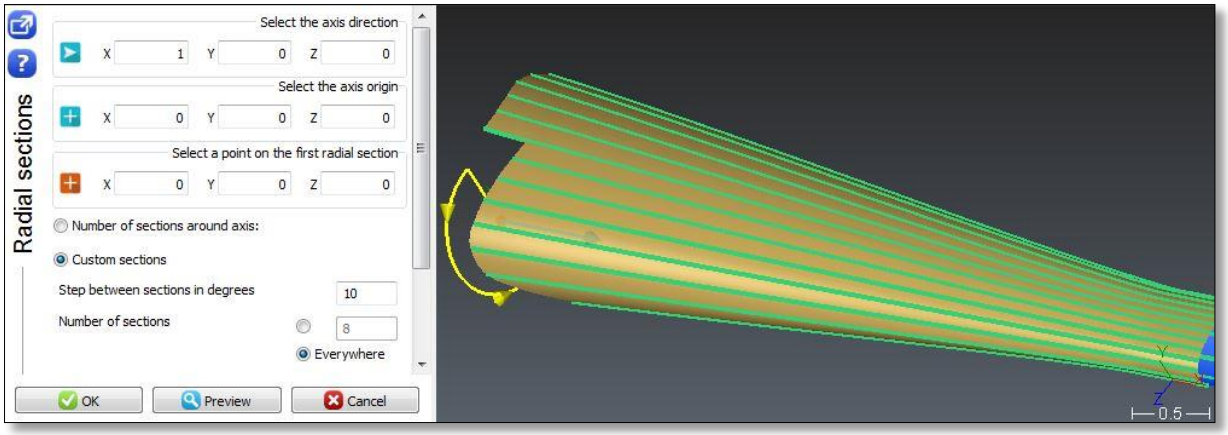

Figure 5.9 – 3DReshaper®: Radial Sections created along the length of the surface model.

2. A set of planar control polylines was created about cross-sectional slices of the inlet (`Polyline > Planar Sections`), spaced 0.1 units apart along the length of the inlet. The `Planar Sections` inputs are shown in Figure 5.10.
3. A feature line was projected along the surfaces at the entrance and exit of the inlet (`Polyline > Feature Line`). The Feature Line inputs are shown in Figure 5.11.

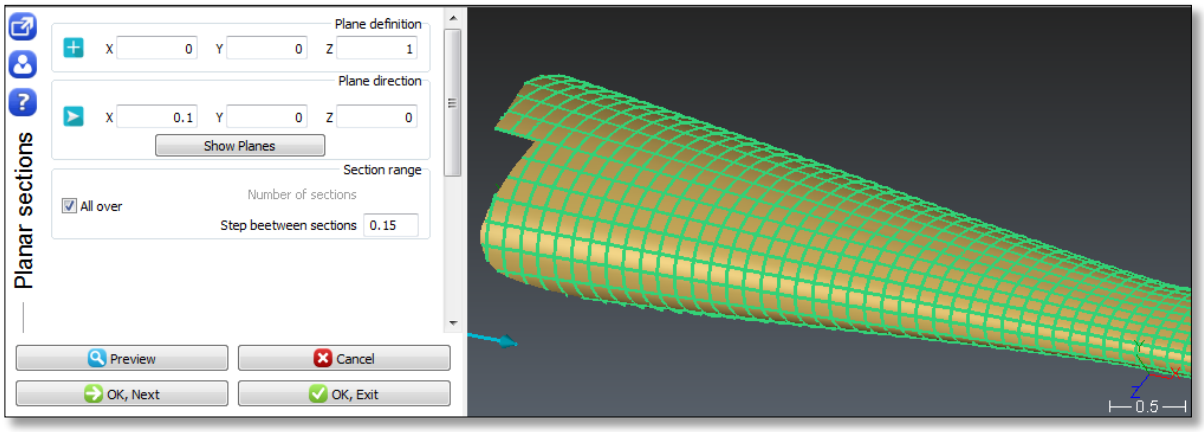

Figure 5.10 – 3DReshaper®: Planar sections created at cross-sectional slices of the model.

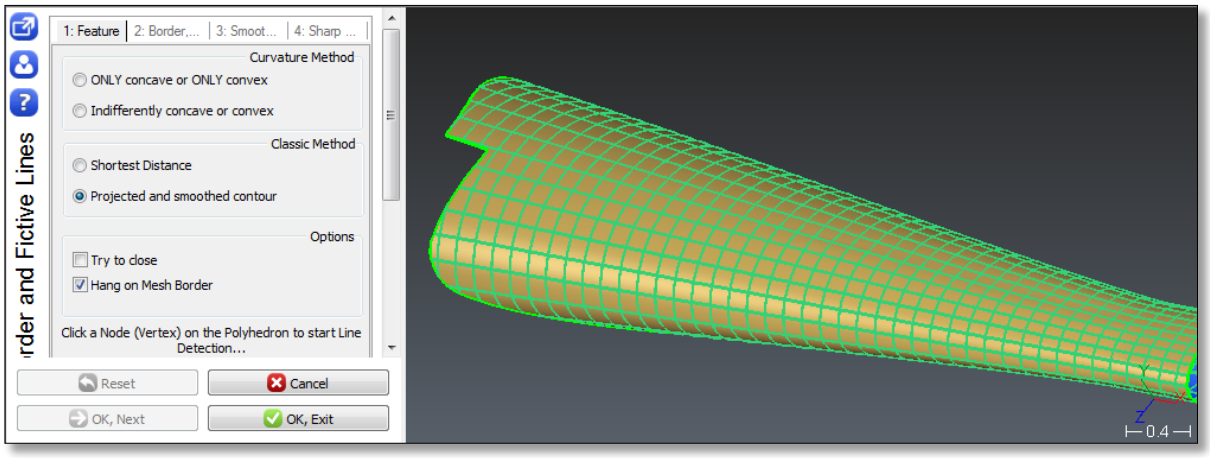

Figure 5.11 – 3DReshaper®: Feature lines incorporated at the entrance and exit of the inlet.

4. These bounding polylines were used as a basis upon which to construct a NURBS surface. The `Generate Patch` tool was used to construct the surface (`CAD > Generate Patch`).

The surface creation method was not successful in representing the more complex shapes at the inlet entrance and cowl closure (Figure 5.12). Further attempts to optimise the solution resulted in other gaps and holes in the surface. The mesh-to-NURBS conversion tool in 3DReshaper was not successful, so the decision was made to continue with surface creation using mesh modification tools. The following sections outline the mesh-based surface building method.

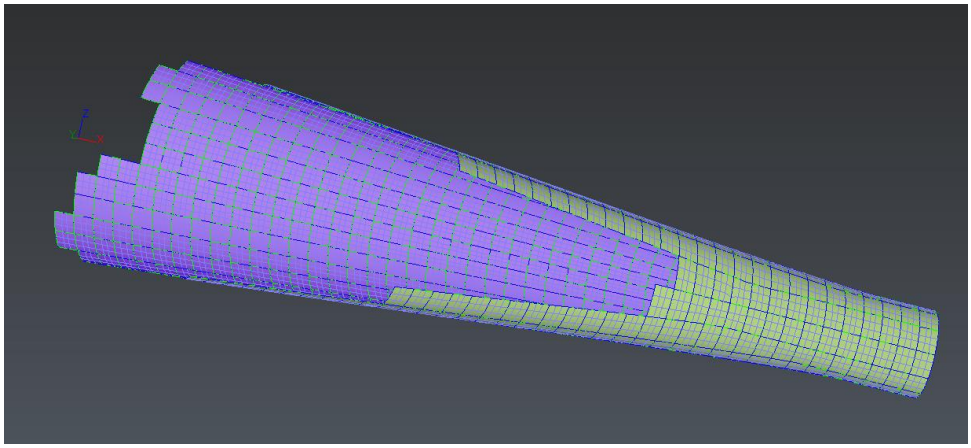

Figure 5.12 – 3DReshaper'r® mesh-to-NURBS conversion did not accurately represent the surface.

5.1.5 Smoothing the Upper Seam Join

Returning to mesh modification techniques, rather than NURBS surfacing techniques, the next step was to smooth the upper seam of the joined inlet. This was able to be done in either 3DReshaper® or Blender™. The decision was made to use 3DReshaper®, as the platform was already in use from the joining process.

1. After selecting the inlet surface, the `Regular Smoothing` feature was activated (`Mesh > Smooth`) (Figure 5.13).

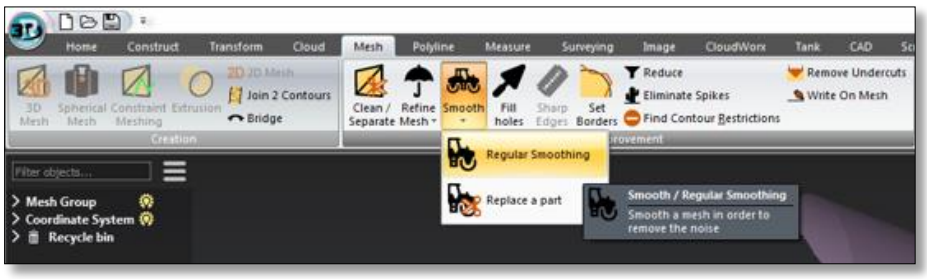

Figure 5.13 – 3DReshaper®: Select 'Regular Smoothing'.

2. In the `Smooth Mesh` control panel, the paintbrush icon, '`Select With A Pencil`', was chosen (Figure 5.14).

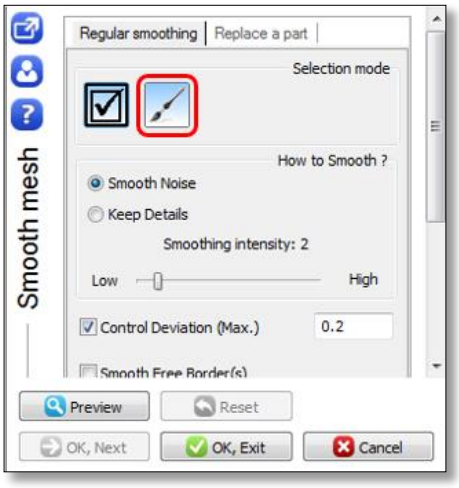

Figure 5.14 – 3DReshaper®: Select the paintbrush icon for 'Select With A Pencil'.

3. Using the pencil tool, the seam was drawn over to smooth the join (Figure 5.15).

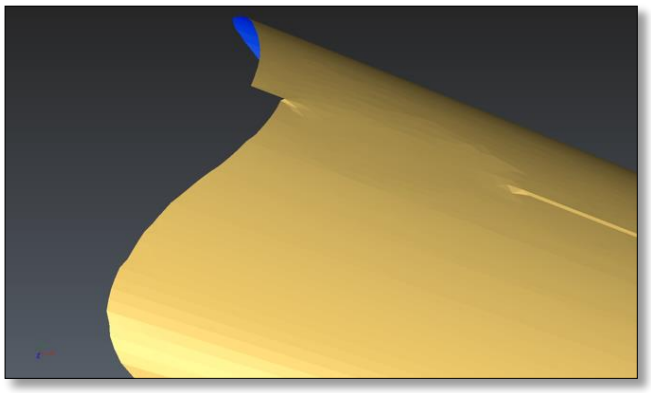

Figure 5.15 – 3DReshaper®: Use the pencil tool to smooth along the join.

After the surface was joined and smoothed, the mesh was exported from 3DReshaper® as an .stl file, and imported into Blender™. The cropping and shaping processes were carried out in Blender™.

5.1.6 Cropping the Cowl Closure Point

As seen previously, the cowl closure points of the two inlet surfaces did not match up properly (Figure 5.16). The HC side closed significantly earlier than the LC side. The decision about how to close this feature down to a single smooth point was determined by the overall effect on the inlet efficiency.

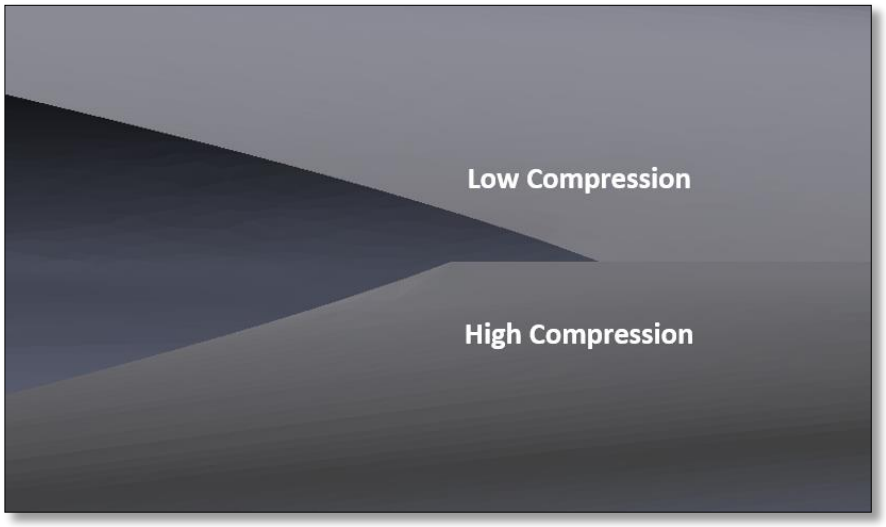

Figure 5.16 – Cowl closure point on the joined inlet. The HC closure point is significantly further forward than the LC point.

As discussed in Chapter 2.3, cutting away the HC closure to match the LC side allows more airflow to spill out of the inlet and improves self-starting and ignition, as well as low-speed performance. Building in the LC closure to match the HC side should have the opposite effect. It was anticipated that trimming the HC side and building up the LC side to meet in the middle would result in an approximate middle ground. As the aim of this project is to attempt to improve low-Mach number performance, the decision was made to allow the LC side to dominate the flow at the cowl closure by cutting away the HC side. The process to cut away the HC cowl closure in Blender™ is outlined below:

1. In `Edit Mode`, the vertices to be removed were manually selected and deleted (Figure 5.17).
2. The remaining edge vertices were then manually moved until they form the desired cowl closure shape.

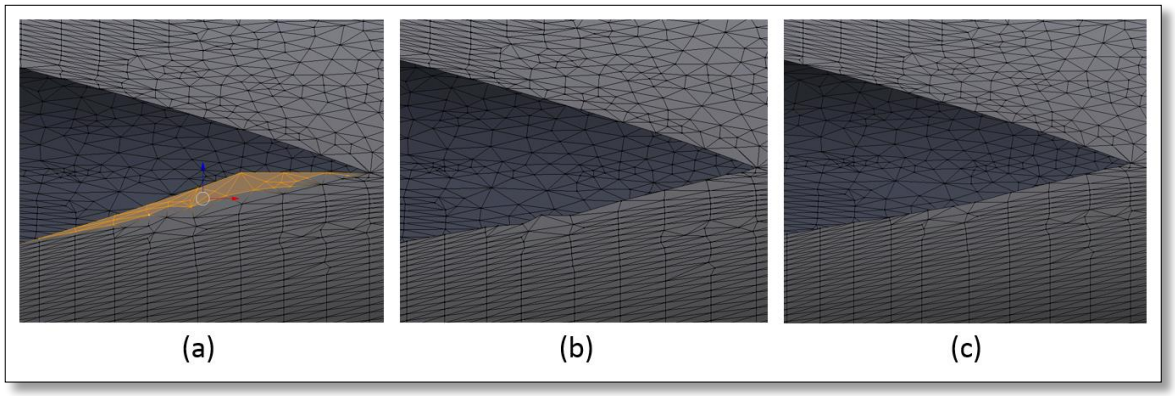

Figure 5.17 – Blender™: Cowl Closure procedure, (a) selecting, (b) deleting and (c) tidying the vertices.

5.1.7 Shaping the Inlet Opening

As with the cowl closure, the inlet entrance was also misaligned on the axis between the HC and LC halves (Figure 5.18(a)). Again, a decision was made regarding how to address this joining issue. The compression characteristics of the Busemann flow field are in part defined by the length of the inlet – a longer inlet allows more air to be gathered and compressed into a throat area of the same size. Trimming away the front section of the HC inlet would reduce the compression field of that inlet significantly, which would largely negate the asymmetric effect. Extending the LC entrance to meet the HC side would have a similar effect, by increasing its CR. In order to give the best possible opportunity to demonstrate the thermal compression effect, it was desirable to maintain the asymmetric effect of the inlet as much as possible. To achieve this, the decision was made to blend down from the join point to the LC side as smoothly as possible (Figure 5.18(b)).

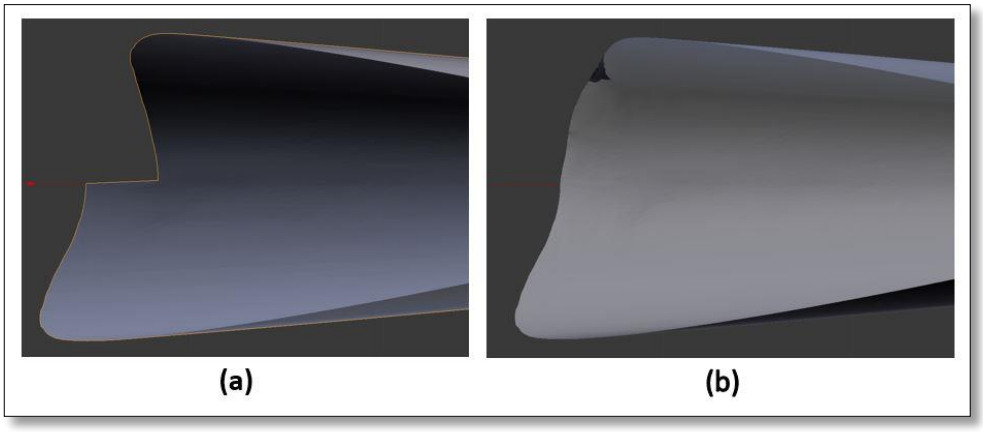

Figure 5.18 – Inlet entrance (a) mismatched between the HC and LC halves, and (b) blended together.

This was done in Blender™ by using mesh modification tools to manually build in a 3D surface to match the desired curve as closely as possible. From Figure 5.18(b), it can be seen that the manual joining process was imprecise and difficult to smooth out perfectly. Some deviations and ripples in the leading edge were generated, which were very difficult to remove due to the nature of the 3D mesh and free-form vertex mobility. The process for building in this section is described below:

1. The joined inlet .stl was imported from 3DReshaper®. A stand-alone HC inlet half was also imported and super-imposed over the LC side of the joined inlet (Figure 5.19). This provided a background mesh structure to trim down and fit into the gap.

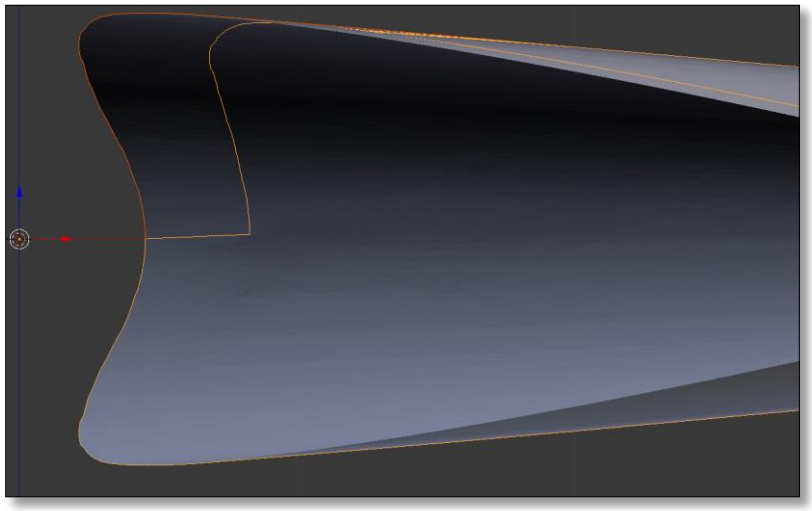

Figure 5.19 – Blender™: Joined inlet superimposed with stand-alone HC inlet.

2. The stand-alone HC inlet was cut down to remove the unnecessary length. First, the joined inlet was hidden using the visibility icon (Figure 5.20), then `Edit Mode` was activated. The knife tool was activated (press `K`) and constrained to the Z axis (press `Z`).

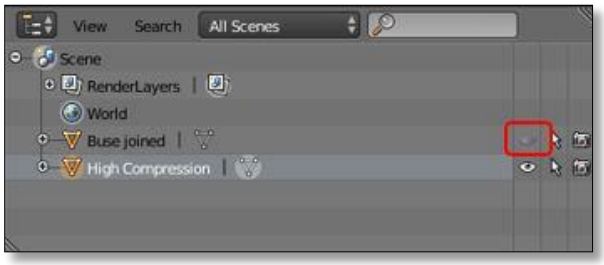

Figure 5.20 – Blender™: Visibility icon in the Scene panel.

3. The `Select Loop Inner Region` was chosen from the `Select` menu, which auto-selected the tail end of the inlet. The tail end was deleted (Figure 5.21).

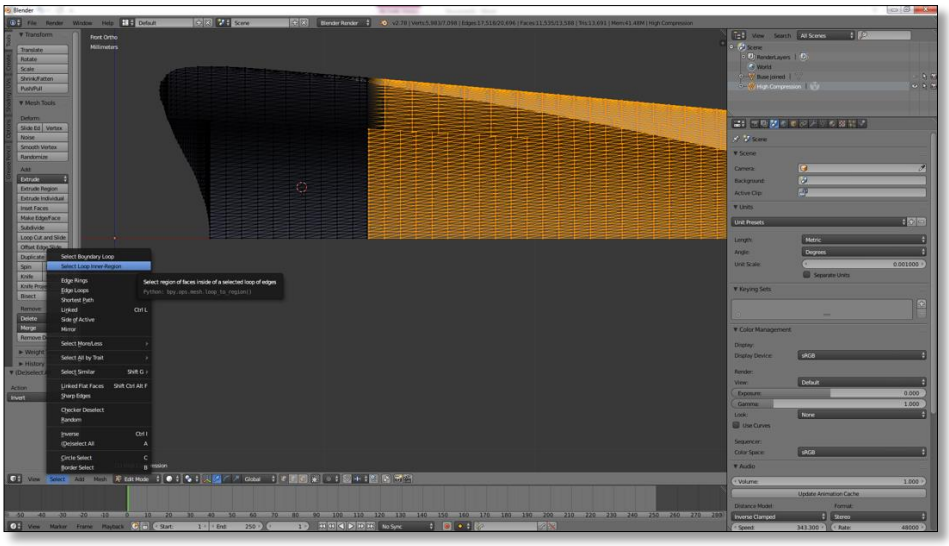

Figure 5.21 – Blender™: Cut the HC inlet, and delete the unnecessary inlet vertices.

4. The joined surface was returned to a visible state, and the stand-alone HC mesh was trimmed down into a shape approaching the desired curvature of the new panel. To do this, the `Circle` selection tool was used to choose the surfaces for deletion (press `C`) (Figure 5.22).

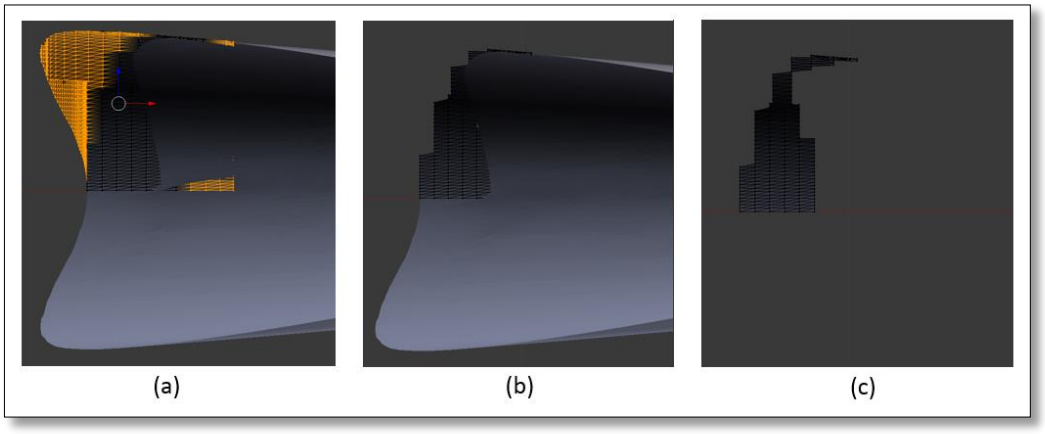

Figure 5.22 – Blender™: (a) Selecting the vertices to trim with the Circle tool, (b) deleting the vertices, and (c) the resultant surface fill mesh.

5. Blender™ was returned to `Object Mode` and both surface meshes were selected (press `A` to select all), then the join feature was used to join both surfaces into one object (`Ctrl-J`).
6. The mode was changed back to `Edit Mode`, and the vertices on the leading edge were manually moved and modified to create a smooth leading edge surface (Figure 5.23).

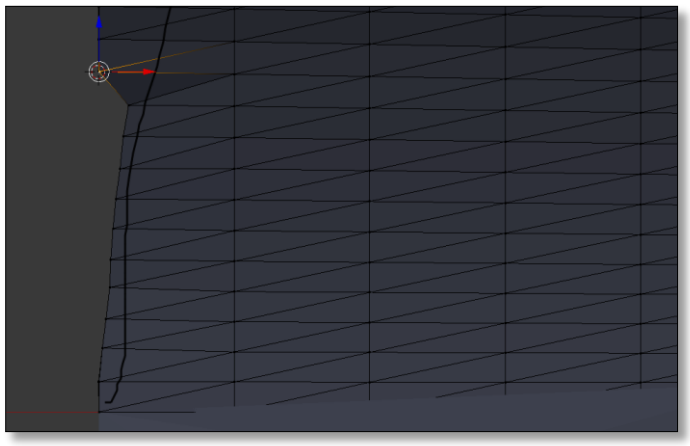

Figure 5.23 – Blender™: Manually building the leading edge by moving individual vertices.

7. It was necessary to relocate the vertices of the stand-alone panel along the centreline to precisely match the vertices on the LC half. To do this, the base vertex (on the LC half) was selected. Then the cursor was snapped to that vertex (`Shift-S > Cursor to Selected`).
8. The vertex to be relocated was then selected and snapped to the cursor positioned at the base vertex (`Shift-S > Selection to Cursor`). The process is illustrated in Figure 5.24.

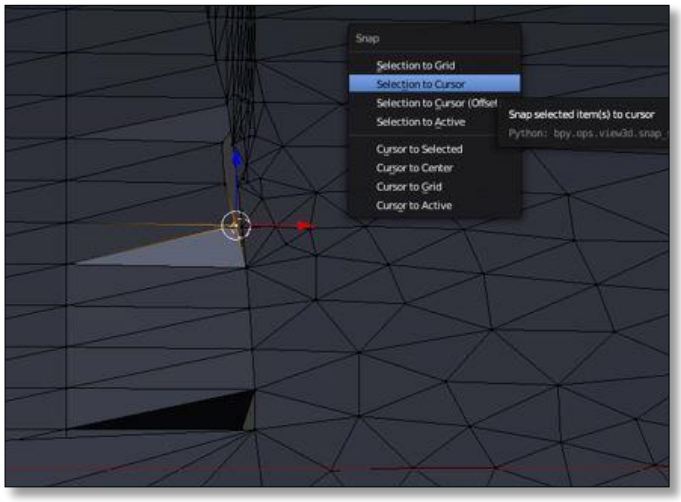

Figure 5.24 – Blender™: Snap vertices on stand-alone panel to vertices on base panel.

9. The result of the previous processes was to build a filler panel. A side-effect of the mesh joining was the introduction of some surface defects which needed to be smoothed. The mesh elements were too large to allow sensitive smoothing in these regions, so the mesh size was reduced using the `Subdivide` tool (`Mesh > Edges > Subdivide` (Figure 5.25)).

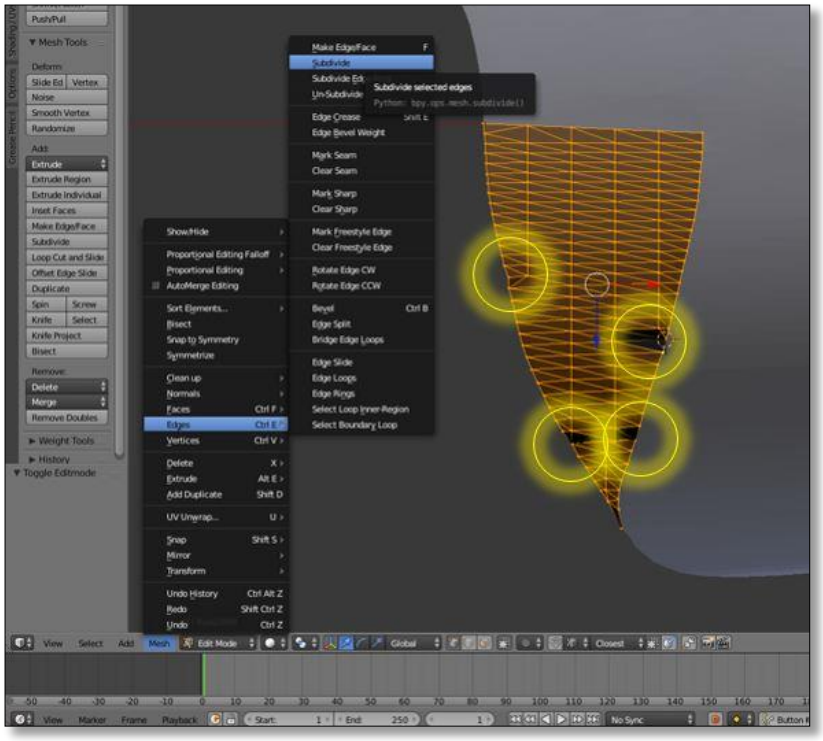

Figure 5.25 – Blender™: Filler surface panel with defects marked in yellow. Subdivide the mesh to make it fine enough for effective smoothing.

10. The joining seam on the back end of the filler panel was somewhat raised above the leading edge of the LC half. Once the vertices had been relocated, an uneven step became noticeable between the two surfaces. To smooth this step, as well as the defects described in Step 9, the operating mode was changed to `Sculpt Mode`. The `Smooth` tool was chosen, and used to smooth the interface between the two surfaces (`Brush > Sculpt Tool > Smooth` (Figure 5.26)).

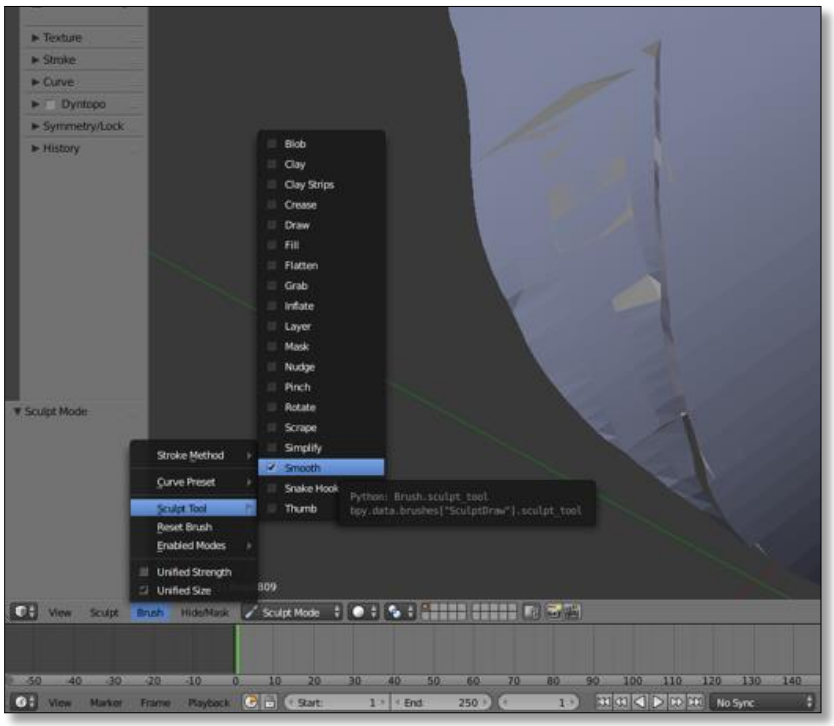

Figure 5.26 – Blender™: The step joining the LC inlet and the filler surface. The surface was smoothed using the Smooth brush in Sculpt Mode.

The process of creating this filler surface was found to be labour-intensive, time consuming, non-intuitive and difficult. The surface was not perfectly smooth, and had defects in the mesh. The smoothing process was challenging to implement, as any holes in the mesh caused the smoothing to be non-effective. The automated `Fill` tool demonstrated only limited success in locating and filling holes.

Once the surface had been successfully generated, it was exported as an .stl file for CFD grid generation. It was discovered that the Blender™ output had issues with inconsistent surface normals, unfilled holes and mesh

irregularities, and was also not capable of generating a non-binary .stl file, which was the preferred input for the Pointwise® grid-generation program. Therefore, it was determined that some pre-processing of the final mesh was required before a CFD grid could be built. The pre-processing was carried out in MeshLab, and is discussed in Chapter 5.1.8.

5.1.8 Pre-Processing the Surface For Grid Generation

Pre-processing the mesh and conducting a final clean-up in preparation for Pointwise® grid generation was completed in MeshLab. The pre-processing procedure is presented below:

1. The Blender™ .stl output was imported as a mesh and the full surface was selected (`Filters > Selection > Select All`).
2. From the Filters menu, the following clean-up operations were run from the Cleaning and Repairing sub-menu:
    - `Compact Faces`
    - `Compact Vertices`
    - `Merge Close Vertices`
3. The vertex normal were redistributed using the `Per Vertex Normal Function` operation (`Filters > Normals, Curvatures and Orientation > Per Vertex Normal Function`).
4. The file was exported (`File > Export Mesh As…`). In the `Export` dialogue box dropdown menu, .stl was chosen as the file type. In the .stl export dialogue box, `Binary Encoding` was de-selected to ensure a non-binary output.

After being exported, this file was then sent for CFD analysis. Further discussion of the analysis process can be found in Chapter 6. The surface was only designed for preliminary analysis, but before future high-fidelity studies may be carried out, some improvements to the model must be made. Viscous and boundary-layer effects must be accounted for, and real-world features must be applied to the model to account for the complicating effect they have on flow behaviour. The following section discusses preliminary attempts to build real-world features into the surface model.

5.2 Applying Real-World Features

The two real-world features which need to be applied to the model are the thickness of the surface material, and the bluntness of the material at the leading edge. Some progress was made in applying surface thickness to the model, but not in blunting the leading edges. The process of applying surface thickness was tested on a REST inlet, rather than the Busemann inlet used for the experimental CFD analysis.

5.2.1 Surface Thickness

The point cloud .stl import creates an infinitely thin mesh to which some thickness must be applied (Figure 5.27). To apply a surface thickness in Blender™, a surface modifier is created when operating in `Object Mode`.

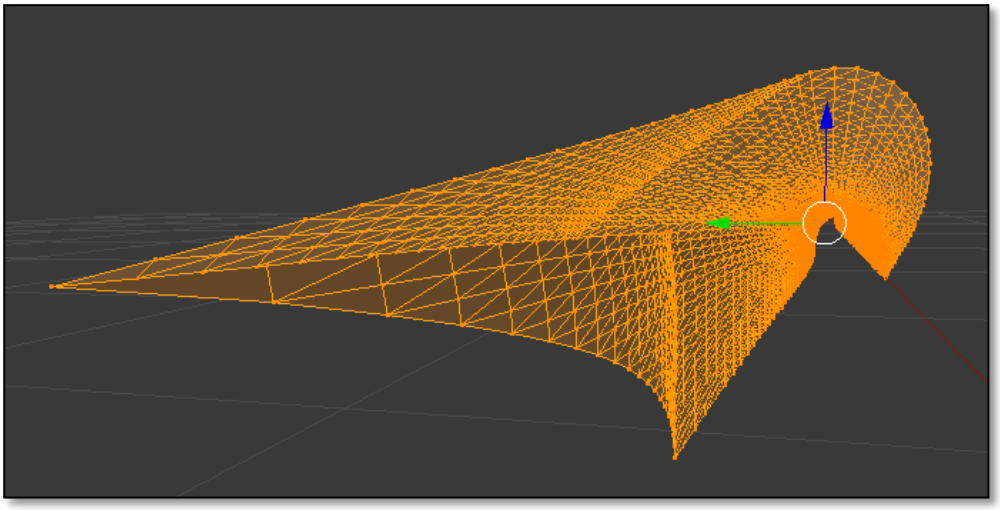

Figure 5.27 – Infinitely thin point cloud mesh.

The process for creating a surface thickness modifier is outlined below:

1. In `Object Mode`, a solidify surface modifier was applied from the `Properties` editor on the right-hand side of the workspace (Figure 5.28). (`Properties Editor > Modifiers > Add Modifier > Solidify`) (Figure 5.29).

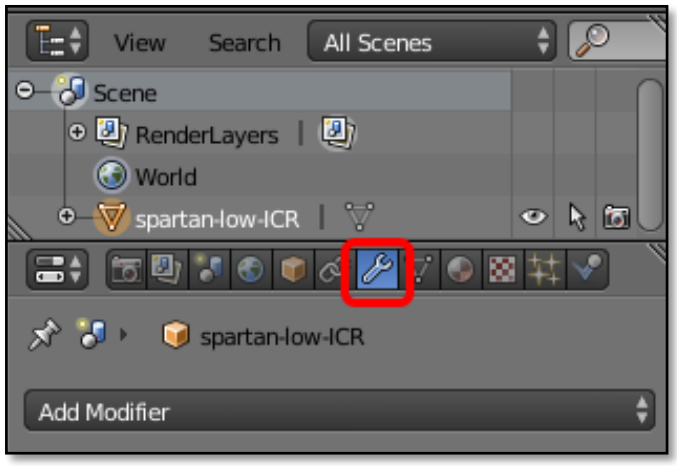

Figure 5.28 – Blender™: Select 'Modifiers' from the Properties Editor

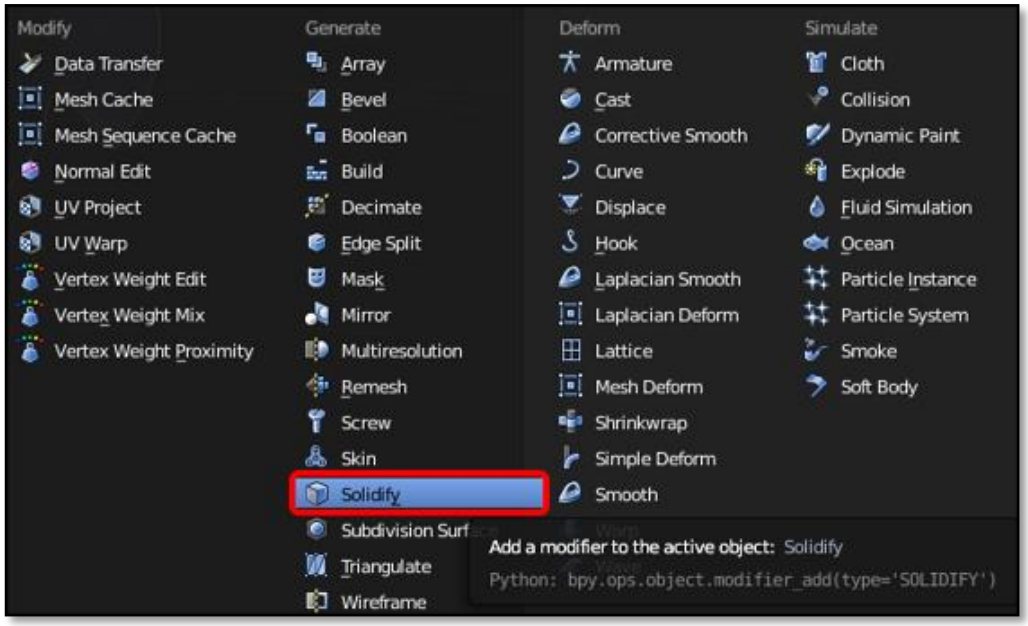

Figure 5.29 – Blender™: Select 'Solidify' Modifier

2. The desired surface thickness parameters were applied in the `Solidify` dialogue box. In testing, this thickness was set to an arbitrary thickness of 0.01 units (the units in Blender™ may be set to metric, imperial or 'unitless', as desired. In the interests of allowing the thickness to be parametrised at a later date during the automation process, the dimensions were left as unitless).
3. In the `Solidify` dialogue box, 'Offset' designates whether the thickness is applied inwardly (-1), outwardly (1), or equally on either

side of the surface (0). In this case, the REST inlet was calculated from the viscous flow properties, and had had boundary layer corrections applied. Thus, it was imperative that the capture area was maintained, so the offset was applied outwardly (1). The other values were set as described in Figure 5.30.

Figure 5.30 – Blender™: Select desired values and click 'Apply'

This process was successful in creating a wall of the desired thickness, except for a gap in the wall on the sharp corner in the front rectangular section (Figure 5.31).

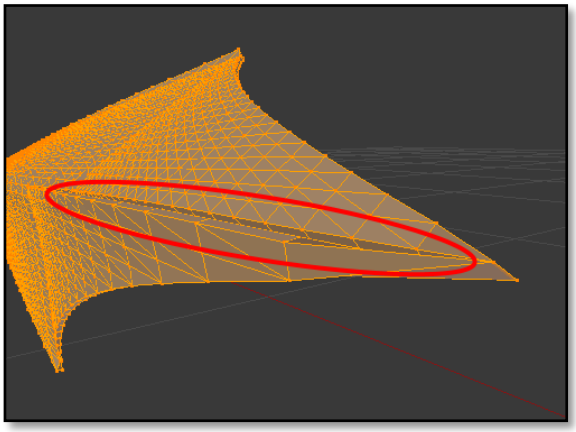

Figure 5.31– Gap in the surface caused by outwardly applying the offset

5.2.2 Constructing and Integrating a Conical Forebody

The vehicle forebody itself provides an initial bow shock as it moves through the flow field, which provides an opening compression wave. The inlet sits within the bow shock, and generates a second shock of its own [3]. A

thorough high-fidelity CFD analysis of the scramjet inlet will involve creating a model of the entire vehicle forebody with an inlet (or multiple inlets, for a modular engine analysis) integrated into the body.

The forebody design is a simple cone with a half-angle of 5°, and a rounded tip with a radius of 5 mm (Figure 5.32). The REST inlet has been designed to integrate into the forebody at a particular attachment point at x = 891.5 mm, y = 465.3 mm (see Appendix H for further information about forebody dimensions). The forebody was constructed in Blender™ by building and joining a truncated cone and a sphere. The process for building the nose section is presented below:

1. Blender's™ cone creation tool makes use of the tail (Radius 1) and nose (Radius 2) radii, rather than using the half-angle. First, the tail radius (Radius 2) was calculated. The cone must be longer than 465.3 mm to allow integration, so a length of 500mm was chosen. All measurements were made from the sphere's centre.

$$R_2 = 500\tan(5) = 43.74\text{ mm}$$

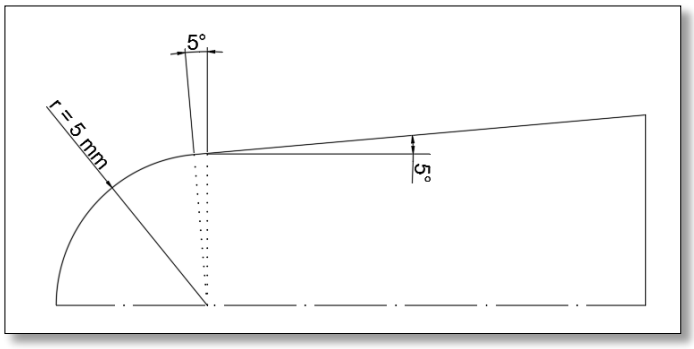

Figure 5.32 – Detail of the conical forebody nose section.

2. The 5° angle meant the cone's base point needed to be relocated to align with the tangent of the sphere (Figure 5.32). The offset distance was calculated:

$$Offset = 5\tan(5) = 0.47\text{ mm}$$

3. In Blender™ (operating in `Object Mode`), a cone was created (`Create > Cone` (Figure 5.33)). The following inputs were given:
   - Vertices = 1000, Radius 1 = 43.74, Radius 2 = 5.
   - Locations: x = -0.47, y = 0, z = 0.

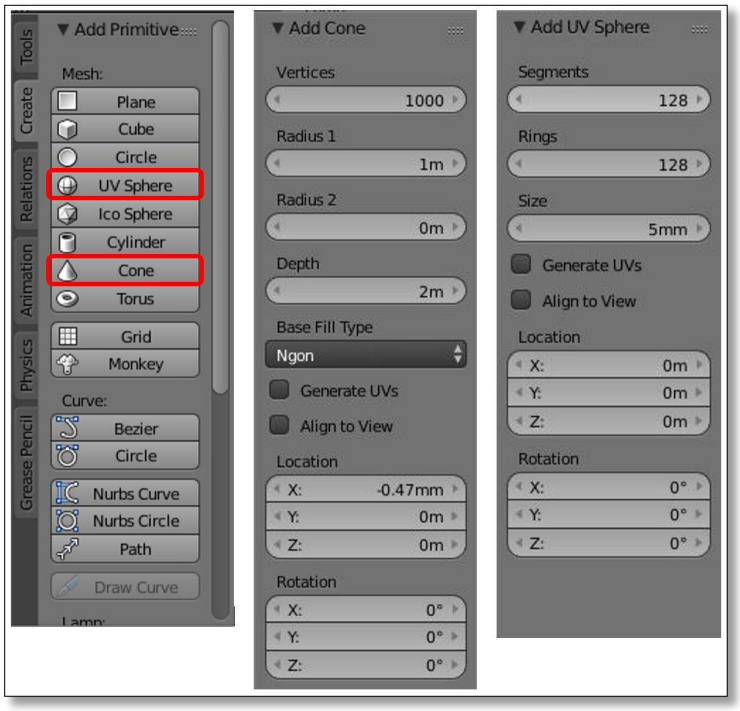

Figure 5.33 – Blender™: Create a truncated cone and spherical tip for the vehicle forebody.

4. A sphere was built to represent the blunt tip (`Create > UV Sphere` (Figure 5.33)). The following inputs were given:
    - Segments = 128, Rings = 128, Size = 5.
    - Location: x = 0, y = 0, z = 0.
5. The two objects were joined by selecting both parts (in `Object Mode` press `A` to select All), and then using the `Join` tool (`Ctrl-J`).

5.3 Automation of the Design Tool

5.3.1 Asymmetric Inlet Creation

No method was found which would enable automation of the asymmetric mesh building process. The only method which was successful in generating an appropriate mesh involved processing the Stile .stl data through three different tools: 3DReshaper®, Blender™ and Meshlab.

3DReshaper's® primary function was to join the two surfaces together. It is possible that a similar functionality exists in Blender™, which may enable the process to be streamlined down to the other two tools (3DReshaper's® smoothing functionality can be replaced by Blender's™ `Sculpt Mode`).

Although no automation process was discovered during this project, it is recommended that further attempts should be made in the future as new 3D modelling technology becomes available.

5.3.2 Building a High-Fidelity CFD Model with Real-World Features

In an ideal scenario, it would be desirable to be able to build a script into the Stile program to automate the full process described in Chapter 5.2 (the building of a vehicle forebody with an integrated inlet having real-world characteristics). In such a script, the parameters necessary for constructing the full vehicle, would be drawn from the source Stile script, and run directly from the command line, without having to open Blender™ at all. In this scenario, a single command line prompt would output an .stl file ready for CFD gridding.

This is currently not a feasible option, due to the limitations on inlet surface generation discussed in Chapter 5.1. However, an attempt was made to automate the vehicle forebody build-and-integration of a real-world inlet, under the assumption that such an inlet has been successfully generated. This attempt was made by writing a Python™ script to be executed within the Blender™ Python™ console.

A script was written which first imported the point cloud from a specific file path, then added a thickness modifier (as per Chapter 5.2.1). A sphere and cone representing the blunt-nosed conical forebody were then built (as per Chapter 5.2.2). The script then joined the three parts into one object and exported the combined mesh as an .stl file ready for pre-processing. The 3D model generated by implementing this script is shown in Figure 5.34. The script is presented in Appendix I.

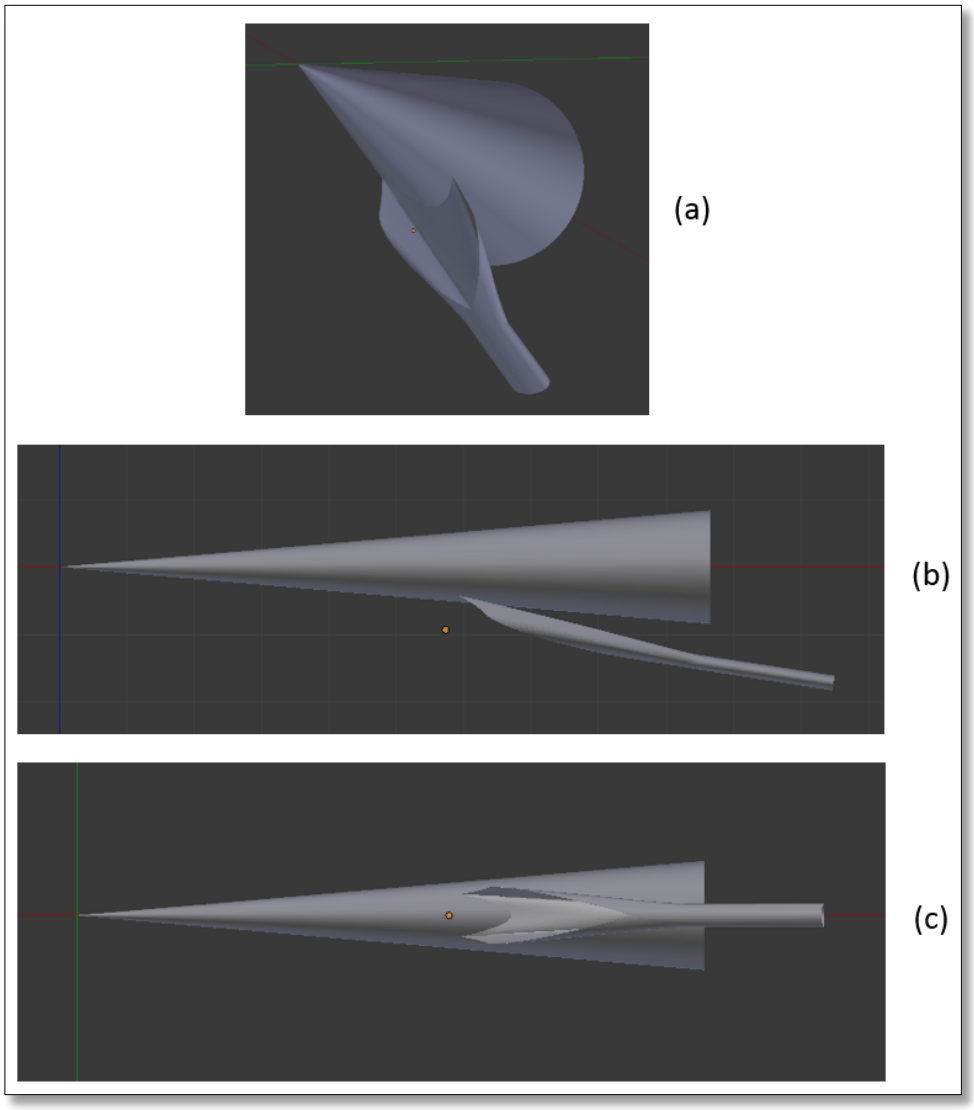

Figure 5.34 – A perspective view (a), side view (b) and bottom view (a) of the forebody and integrated inlet, as generated by the automated Python™ script.

5.4 Robustness of the Design Tool

The intention of robustness testing was to design and test a method for its usefulness on other surfaces. The first asymmetric surface, featuring an LC half with a 30% reduced compression ratio compared to the HC half, was constructed in 3DReshaper® and Blender™ manually, using mesh modification tools. Once this mesh had been completed and sent for analysis, an attempt was made to use the same process on an inlet with an LC compression ratio 50% reduced from the HC (Figure 5.35).

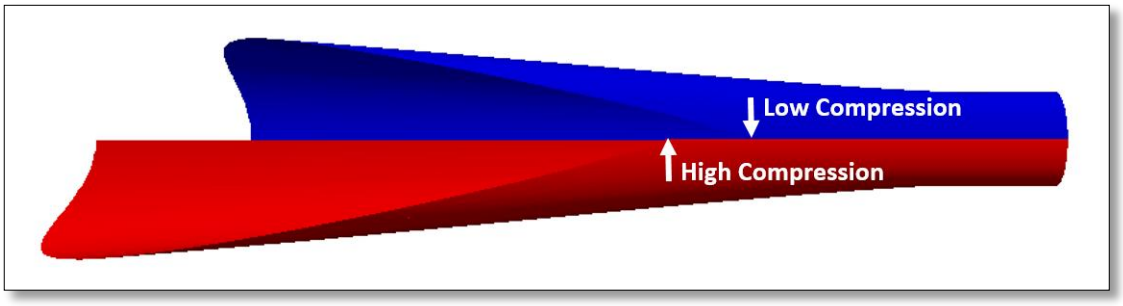

Figure 5.35 – Two inlet halves: an HC half, and an LC half, with a compression ratio reduced by 50%.

The extreme variation in shape between the two inlet halves of the 50% reduced inlet made mesh generation much more difficult, particularly at the entrance where a filler surface was required. The 50% reduced inlet was not able to be completed within the required time frame.

Chapter 6

CFD Analysis of Asymmetric TC Inlet

The CFD analysis was carried out by thesis supervisor Dr. Rowan Gollan and his colleagues in the Centre for Hypersonics. The simulation was performed on a 3D unstructured grid, which was prepared by UQ PhD candidate Jens Kunze. The grid consisted of 182263 individual cells, divided into four blocks with roughly equal cell counts (Figure 6.1) (larger prints of these images are also presented in Appendix J).

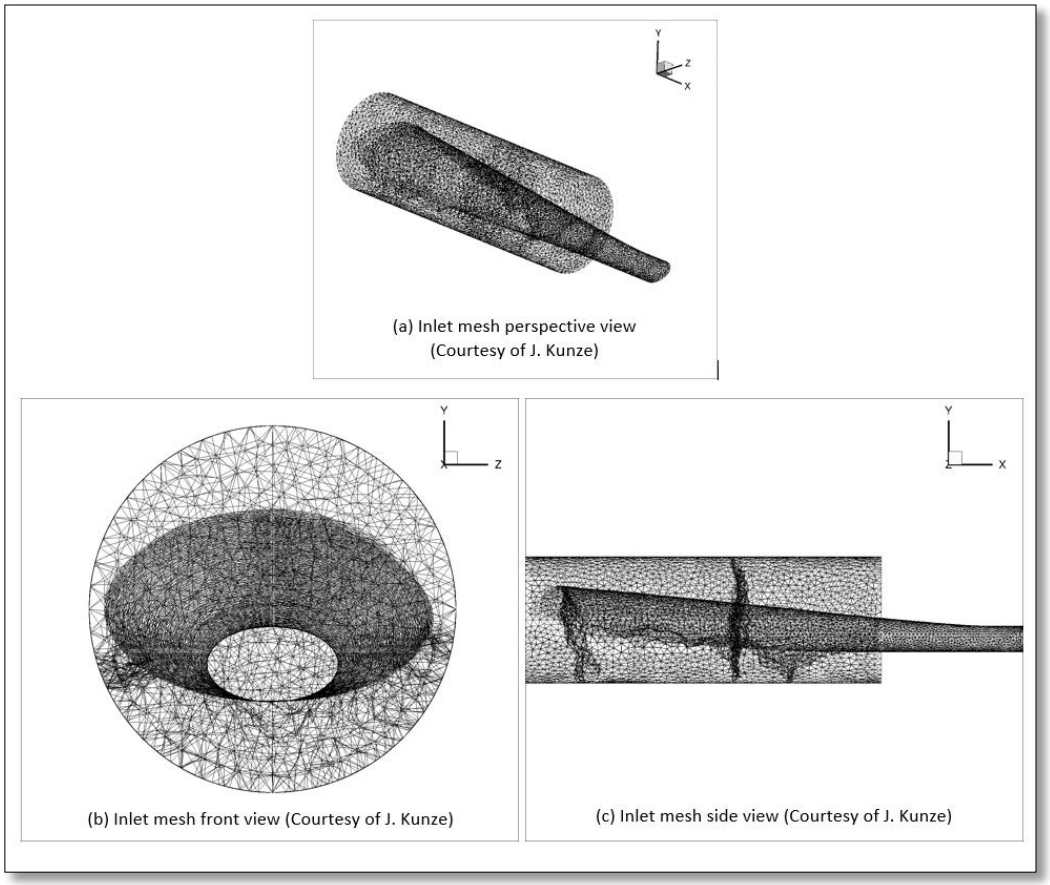

Figure 6.1 – 3D unstructured grid for CFD simulation (Courtesy of J. Kunze). Larger prints also presented in Appendix J.

The simulation was performed in the Eilmer 4 compressible flow solver [111]. The flow was treated as inviscid, with slip-wall boundaries at the inlet surface, to match the design conditions described in Chapter 4.1. A

supersonic flow was prescribed on the inflow boundary, and the outflow was set as an extrapolate out condition.

The gas was modelled as ideal air with constant specific heats, with the inflow conditions representative of flow conditions behind a 6° wedge forebody (representing the conical vehicle shape) travelling at Mach 12. The inflow conditions were:

p = 2247.2 Pa

T = 372.44 K

M = 9.1113

The simulation took approximately 40 minutes to reach a steady state condition, using 4 cores of an Intel i7vPRO CPU. The results are presented in Chapter 7.2.

Chapter 7

Results

The project aims as presented in Chapter 3 related firstly to generating a body-integrated thermal compression inlet, and secondly to the development of a design process which could expedite the current methods in place. The results will be assessed in reverse order: first, a look at the design process developed over the course of the project, and second, an assessment of the thermal compression inlet.

7.1 Efficient Surface Generation of an Asymmetric Inlet

Using the processes described in Chapter 4 and Chapter 5, an asymmetric Busemann inlet was created (Figure 7.1). The goals of the design aspect of the project were related to:

- Stile point cloud generation,
- Tool selection,
- Smoothing and joining of the surface,
- Application of real-world features,
- Automation, and
- Robustness

The results of the design exercise will be addressed these terms.

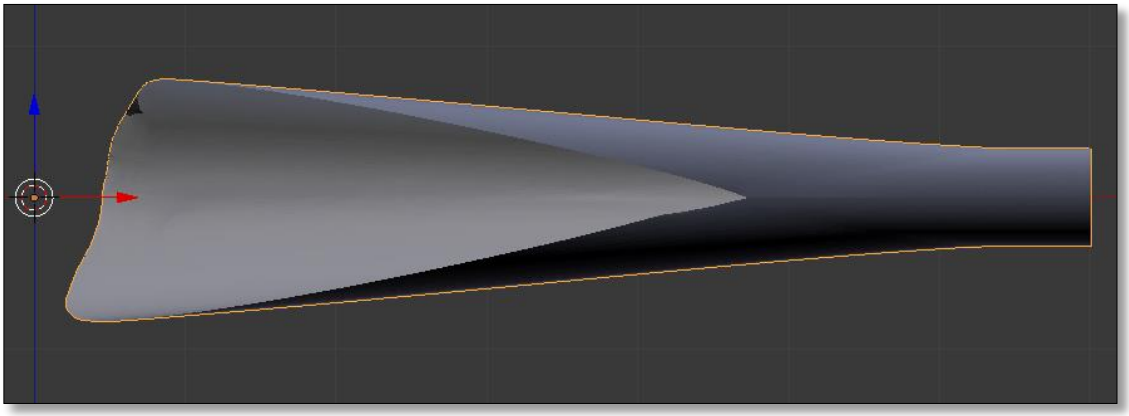

Figure 7.1 – An asymmetric Busemann inlet with a Low-Compression side (top) generating 30% less compression than the High-Compression side (bottom).

7.1.1 Stile Point Cloud Generation

Once the primary decisions had been made regarding comparative compression ratios, and the method of scaling the two inlet halves, applying these changes to the Stile tool was very successful.

By simplifying the problem down from a REST inlet to a Busemann inlet, and applying the scaling process to the `build-inviscid-surface.lua` file, the two compression fields were created to represent the basis of an asymmetric surface with differing compression fields (Figure 7.2). The scaling process produced a throat output of the required aspect ratio to join to the combustor inlet, and the point clouds were capable of being modified in most 3D modelling programs.

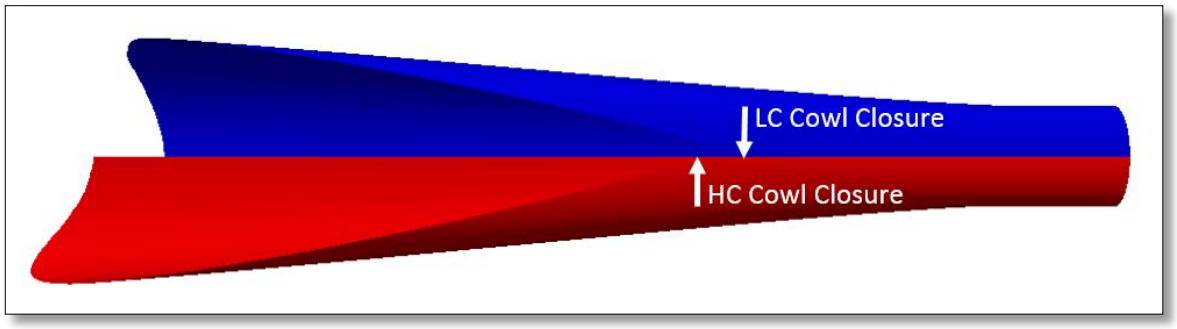

Figure 7.2 – The Stile output of the HC and scaled LC halves, joining appropriately at the throat.

7.1.2 Tool Selection

The tool selection process did narrow down the field of potential software candidates, but it became apparent that none of the software chosen for this project had all of the capabilities required for successful project completion. Blender™ was chosen as the best candidate package, but it was not capable of converting the inlet surfaces to NURBS. Its mesh modification tools, whilst flexible enough to brute-force the design project, were neither user friendly, nor entirely satisfactory in terms of the resulting surface smoothness and integrity. Some holes and irregularities were left in the mesh, and it was left to MeshLab to resolve them.

Whilst Blender™ is Python™ scriptable, the process used for developing the asymmetric inlet was not. The surface had to be modified manually, which was a painstaking process, and difficult to complete cleanly. The current process used by the Centre for Hypersonics to generate

symmetrical inlets in CATIA™ is also time-consuming and difficult, with inlet processing taking anywhere from days to weeks to complete[2]. Once the groundwork had been set, this asymmetric inlet took two to three days to complete, which did not represent any significant time saving compared to the comparative CATIA™ process.

It is possible that, with more time to grow accustomed to the software and develop a better idea of how to work with the tools, the modelling time may be reduced, and the output quality improved. This may enable further design experiments to be carried out whilst the search for a more suitable software package continues.

3DReshaper® was introduced as a candidate software because of its potential as a mesh-to-NURBS conversion tool. However, the complexity of the inlet shape meant that the conversion tool did not work properly. Attempts to convert to NURBS resulted in a poor surface representation (Figure 7.3).

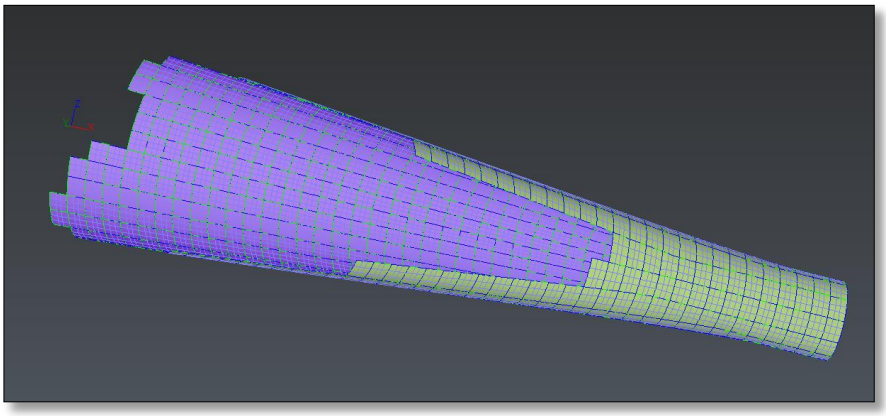

Figure 7.3 – The 3DReshaper mesh-to-NURBS function failed to provide a good surface representation.

Some of its other functions, such as joining and smoothing, were also found to be of use. The tool to create a join along the seam between the high- and low-compression surfaces proved to be the most quick and effective method of joining the two surfaces, although Blender™ also had a similar functionality available.

[2] The SPARTAN inlet being developed in early 2017 took approximately 5-6 weeks to process, due to a requirement to create a full set of manufacturing drawings. For iterative CFD testing, the full detail of a manufacturing drawing is not required, so surface generation in CATIA™ can be completed in the order of 4-5 days.

Although the mesh-to-NURBS functionality was found to be unfit for the purposes of this project, 'Reverse Engineering' technology is still in its infancy, and not as well established as the more longstanding mesh geometry tools. As Reverse Engineering is primarily of interest in the additive manufacturing industries, which are currently enjoying rapid and significant growth, it remains possible that Reverse Engineering software tools will become more accessible and more powerful in the foreseeable future. Therefore, whilst it is recommended that 3DReshaper should not be pursued further as a candidate program at this time, it is anticipated that future developments in mesh-to-NURBS capabilities may open the design space in the future.

It is also worth noting that Maya® and Rhinoceros® have the capability of converting to NURBS. The Rhino® tool requires a plug-in, RhinoResurf, which was not available for use during the majority of the project duration. Limited experiments with the software proved promising, and a second recommendation is that Rhinoceros® and RhinoResurf should be explored further to determine their suitability for purpose.

MeshLab was introduced as a way of filling in the deficits left by Blender™. It was found to be a very powerful mesh modification tool, with excellent facilities for correcting errors and irregularities in a mesh. Of the three tools used in this project this one was the most successful in fulfilling its purpose. For the present, it is recommended to keep MeshLab available for addressing meshing issues, however, the preferred solution in the long-term is to identify a software package capable of replacing the Blender™/MeshLab combination.

7.1.3 Creating a Surface Suitable for CFD Analysis

The combination of software packages chosen was successful in both joining and smoothing the surface, and presenting a surface suitable for CFD analysis. The surface had some problems with the smoothness and shape of the leading edge between the HC and LC halves, which were due to the manual nature of the surface building process.

One key result of the surface generation process was that Blender™ was not capable of generating a CFD-ready surface. The problems with the surface were:

- Some holes and irregularities were left in the mesh, which Blender™ had not been able to properly clean up.
- The surface normals were not all directed the same way. This was resolved in post-processing with MeshLab.
- The .stl output from Blender was binary, which was less suitable for grid generation in Pointwise®. In some cases, a binary .stl file may work adequately, but a non-binary version is preferred, as this allows more in-depth trouble-shooting and analysis of the output in the event that problems are detected.

7.1.4 Application of Real-World Features

Some progress was made in applying real-world features to a REST inlet, but the method was not followed through to a complete conclusion. Some surface thickness was applied to the REST inlet, but potential problems were noted in the meshing, specifically in relation to a gap in the mesh in the rectangular section (Figure 7.4). The current assumption is that this gap will not have a negative effect on the surface once it has been properly integrated onto a conical forebody for high-fidelity CFD analysis. Further investigation is required to establish whether this assumption is correct, and, if not, what effect this gap may have on the model's integrity. It may then be necessary to take further steps to address this issue.

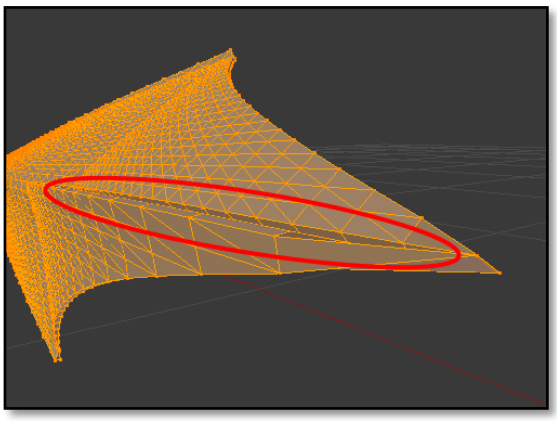

Figure 7.4 – A gap in the surface thickness mesh.

7.1.5 Automation

Similarly, some progress was made towards automating the design process, but not as it related to the asymmetric inlet shape. The parts of the process that were able to be automated were the integration of an already-constructed inlet onto a conical vehicle forebody (Figure 7.5).

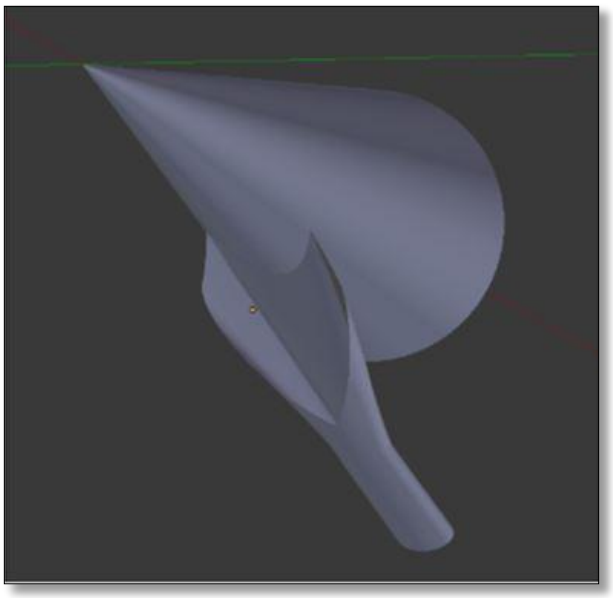

Figure 7.5 – Automated construction of vehicle forebody and integrated inlet.

As an initial test, this script was successful in automating the build. There is potential for this script to be implemented on current inlet designs, with the possibility of providing significant reductions in surface processing time. However, some bugs remain in the code, and further work is required in testing and implementing these processes before putting them to use. There is also potential for this script to prove useful in processing future asymmetric inlets, once the concept of an asymmetric thermal compression inlet has been further validated.

7.1.6 Robustness

An attempt was made to use the surface generation method on a different surface, featuring an LC compression ratio 50% reduced from the HC (Figure 7.6). On this inlet, the LC half had a vastly different shape from the HC half, and it was found that the method used on the 30% reduced inlet was

less effective and more difficult to implement. The 50% reduced inlet was not able to be completed within the required time frame.

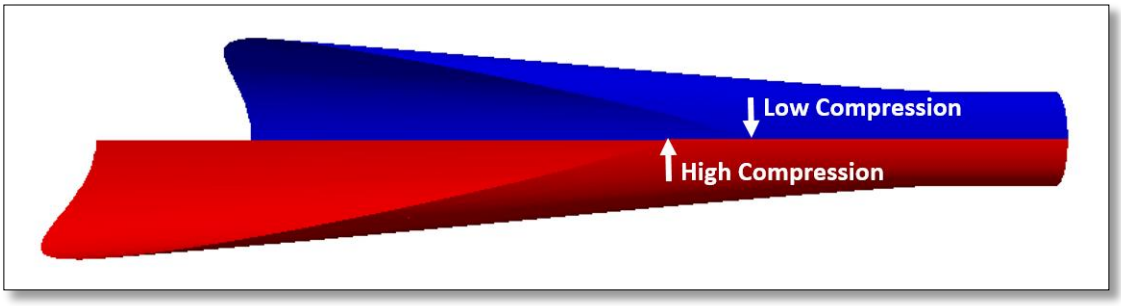

Figure 7.6 – Two inlet halves: an HC half, and an LC half, with a compression ratio reduced by 50%.

When attempting to construct the filler mesh in Blender™, the step between the joining patch and the LC side was quite extreme, and caused difficulties with surface holes and smoothing (Figure 7.7). This suggested that the meshing method used to create the surface mesh was not necessarily a good candidate for other surfaces, and could not be considered robust.

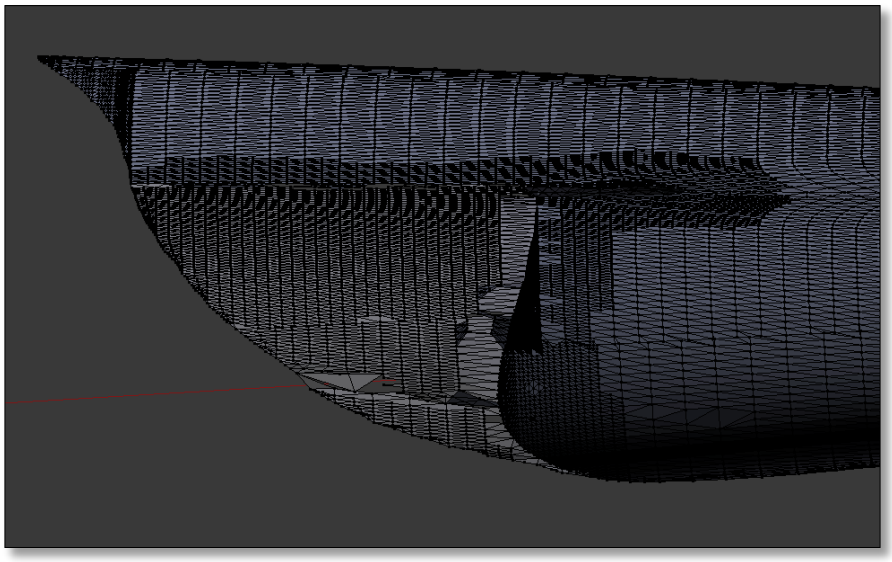

Figure 7.7 – An asymmetric inlet with a 50% reduced LC half. The difference in inlet halves is so great that building the filler patch proved very challenging.

7.2 Thermal Compression Effect in an Asymmetric Inlet

The primary goal of this thesis was to determine if an asymmetric inlet could be successful in generating a non-uniform pressure distribution at the throat, suitable to allow for thermal compression combustion. The simulation results were processed to give cross-sectional slices showing the pressure

fields across the inlet. Relative to the desired output pressure of ~50 kPa (as indicated in Chapter 4.1.4), pressure contours from 20 to 60 kPa were plotted.

The results showed weak evidence of a non-uniform flow field at the throat, with the HC side peaking at ~60 kPa, and the LC side troughing at ~25 kPa (Figure 7.8). The non-uniformity in the compression field was not as strong as anticipated, which was partially attributed to the natural tendency of the two streams to equalise.

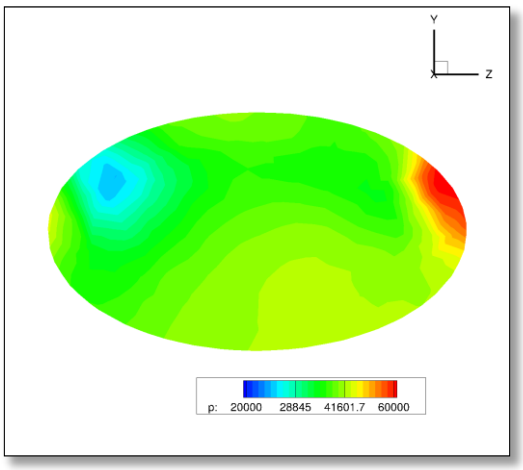

Figure 7.8 – Inlet slice at the throat, showing a non-uniform compression field. The high-pressure area (red) is on the HC side of the inlet; the low-pressure area (blue) is on the LC side.

However, of more concern was an unanticipated shock which was observed to reflect off the cowl closure point (Figure 7.9). This shock was most clearly observed in slices at x = 5 and x = 6, and had a measured peak of ~120 kPa (not shown in the images, due to the pressure range of the contour plots from 20 – 60 kPa).

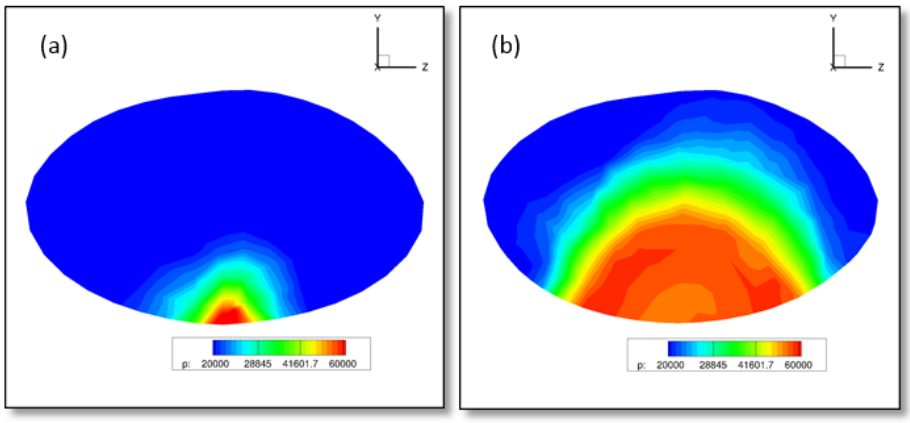

Figure 7.9 – Slices at (a) x = 5 and (b) x = 6, showing a shock wave reflecting off the cowl.

This very high pressure shock dominated the internal pressure field, resulting in significant disruption to the subtle non-uniformity intended. This unexpected result demonstrated an unforeseen gap in the design process, and leaves open the question of whether this design, and the pressure field it generates, will be successful in allowing TC combustion to occur. Further investigation into airflow behaviour at the cowl closure point will be required before this question can be answered.

Chapter 8

Conclusions and Recommendations

The primary aim of this project was to determine whether an asymmetric inlet could produce the pressure distribution necessary for thermal compression in the combustor. To determine this, an asymmetric 3D TC inlet was developed and analysed. The inlet shape was generated using the university's Stile software, and the surface was constructed using a combination of 3D modelling tools. An attempt was made to develop a rapid surface modelling process to enable more efficient testing of subsequent designs in the future.

This project has been inconclusive in determining whether an asymmetric inlet can create the conditions required for thermal compression to occur in a scramjet engine. The shock reflected from the cowl closure point caused undesirable effects on the flow field, thus the design decisions surrounding the cutback of the closure point will need to be revisited. As discussed in Chapter 5.1.6, the decision was made to allow the LC half to dominate the design at the closure point, but further work is required to determine whether there is a better method of choosing the closure point in order to minimise the reflected shock.

It may be necessary to work through several design iterations in order to solve this problem. Whilst this is possible with the surface generation methods investigated above, the design process remains time-consuming and non-user-friendly. However, the requirement for a set of iterative designs presents an opportunity for robustness-testing of the current design method, and/or investigating new methods.

Two key recommendations have arisen from the primary project outcomes:

1. Work should continue on the inlet design with a view to removing or minimising the cowl shock, and preserving the non-uniform distribution at the throat with the least possible interference.
2. Once the cowl closure issue has been resolved, a full system analysis should be performed on the engine to determine the effect of the asymmetric inlet on overall engine performance.

Surface modelling of the inlet proved to be challenging, and a rapid, user-friendly surface generation process was not developed. The primary reason for this was the limitations of the software used. None of the programs tested were able to successfully convert the mesh surface to NURBS in this application. 3DReshaper® was introduced specifically to address this problem, but was unable to adequately process the surface.

It remains unclear whether having NURBS surfaces would simplify surface generation, but one recommendation is that this theory should be more explicitly tested. A promising mesh-to-NURBS tool is Rhinoceros® with the RhinoResurf plugin applied. Maya® also offers mesh-to-NURBS functionality, which was not thoroughly tested throughout this project. The iterative process required to solve the cowl closure problem presents an excellent working opportunity to evaluate Rhinceros® and Maya® as potential tools. (Preliminary experiments with both tools suggest Rhinoceros® demonstrates the greatest potential in this area).

The 3DReshaper® software failed to fulfil its intended use as a mesh-to-NURBS convertor. It was successful in joining and smoothing the two halves, but these functions were also capable of being performed in Blender™. As such, in the interests of simplifying the process, it is also recommended that 3DReshaper® should not be considered a staple of the design process. Rather, the recommendation is that, until such time as a more versatile program presents itself, mesh generation should be carried out in Blender™ and post-processed in MeshLab.

This recommendation comes with a strong caveat: Blender™ was able to adequately model the surface using mesh modification tools, but the

process was neither rapid nor user-friendly. The surface had problems with smoothness at the inlet, and the mesh was prone to developing invisible holes. Blender™ is only recommended due to the current lack of any other preferred options. A stronger recommendation is that a better software package should be identified. The most promising package at this point is Rhinoceros®.

Regardless of whether work continues in Blender™, or whether another software option is found, any package in use should be subject to robustness testing. Two areas present themselves as ideal opportunities for testing, being:

1. An iterative process should be carried out in an attempt to resolve the issue with the cowl shock, and
2. A series of inlet designs should be developed and tested to determine the optimal thermal compression behaviour with respect to HC-to-LC compression ratio.

These investigations would enable the designer to develop a higher degree of familiarity with the design tool, and form sharper conclusions as to its usefulness.

If such robustness testing should suggest that this modelling method is suitable for upcoming designs, it is further recommended that the sub-tasks of application of real-world features and process automation should be revisited. (It may be worth revisiting these processes in any case, as a possible way of assisting the Centre for Hypersonics to remove the roadblock in their current design process.)

Whilst this project has been inconclusive in the outcomes for both the primary and secondary goals, it presents a very promising launching point for further investigations. The chosen design process was able to create a surface, but not to provide a rapid, iterable solution. It was not able to be automated, and challenges were encountered in creating a user-friendly surface generation method. A potential resolution has been identified, which involves experimenting with the mesh-to-NURBS functionality of Rhinoceros®.

The asymmetric geometry of the test inlet successfully generated a non-uniform pressure distribution in the throat section. This pressure

distribution was disturbed by unwanted effects from a reflected shock at the cowl closure point, but it is anticipated that this problem is not without a solution. From this starting point, where a non-uniform compression field has been successfully created, it seems likely that a solution enabling a full feasibility analysis is well within reach.

References

1. Ferri, A. and H. Fox, *Analysis of fluid dynamics of supersonic combustion process controlled by mixing.* Symposium (International) on Combustion, 1969. **12**(1): p. 1105-1113.
2. Bricalli, M.G., L.M. Brown, and R.R. Boyce, *Numerical Investigation into the Combustion Behavior of an Inlet-Fueled Thermal-Compression-Like Scramjet.* American Institute of Aeronautics and Astronautics. AIAA Journal, 2015. **53**(7): p. 1740-1760.
3. Gollan, R.J. and M.K. Smart, *Design of Modular Shape-Transition Inlets for a Conical Hypersonic Vehicle.* Journal of Propulsion and Power, 2013. **29**(4): p. 832-838.
4. Gollan, R., *Stile User's Guide: Computer Tools for developing Shape-Transitioning Inlets for hypersonic airbreathing engines*. 2016.
5. Pinckney, S.Z., *Rectangular capture area to circular combustor scramjet engine - NASA-TM-78657*. 1978, Sponsoring Organization: NASA Langley Research Center.
6. Smart, M.K., *Design of Three-Dimensional Hypersonic Inlets with Rectangular-to-Elliptical Shape Transition.* Journal of Propulsion and Power, 1999. **15**(3): p. 408-416.
7. Curran, E.T., *Scramjet Engines: The First Forty Years.* Journal of Propulsion and Power, 2001. **17**(6): p. 1138-1148.
8. Ferri, A. *Discussion on M. Roy's Paper 'Propulsion Supersonique par Turboreacteurs et par Statoreacteurs'*. Advances in Aeronautical Sciences 1960 [cited 1; 19 - 112].
9. Mackay, J.S. and R.J. Weber, *An Analysis of Ramjet Engines Using Supersonic Combustion*. 1958.
10. Nicholls, J.A., Dabora, E. K., and Gealev, R. L. *Studies in Connection with Stabilized Detonation Waves*. in *Proceedings of the Seventh Symposium on Combustion*. 1959. Butterworths.
11. Gross, R.A.a.C., W., *A Study of Supersonic Combustion.* Journal of the Aerospace Sciences, 1960. **27**(7): p. 517 - 524, 534.
12. Curran, E.T. and J. Swithenbank, *Really High Speed Propulsion by Scramjets A description of the scramjet and an analysis of its performance in the high hypersonic speed range.* Aircraft Engineering, 1966. **38**(1): p. 36-41.
13. Dugger, G.L., *Comparison of Hypersonic Ramjet Engines with Subsonic and Supersonic Combustion*. High Mach Number Airbreathing Engines. 1961, Oxford: Pergamon.
14. Ferri, A., Libby, P. A., and Zakkay, V. *Theoretical and Experimental Investigations of Supersonic Combustion*. in *International Council of the Aeronautical Sciences, Third Congress*. 1962. Stockholm: Spartan.
15. Smart, M.K., *How Much Compression Should a Scramjet Inlet Do?* AIAA Journal, 2012. **50**(3): p. 610-619.
16. Sutton, G.P. and O. Biblarz, *Rocket Propulsion Elements*. 2011, Hoboken, UNITED STATES: John Wiley & Sons, Incorporated.
17. Kimura, T. and K. Sawada, *Three-stage launch system with scramjets*, T. Kimura, Editor. 1999. p. 675-680.
18. Creagh, M., *Attitude Guidance and Control for a Spinning, Asymmetrical Vehicle*. 2010, The University of Queensland, School of Mechanical and Mining Engineering.

19. Allen, A.D.a.J., *Conceptual Study of Rocket-Scramjet Hybrid Engines in a Lifting Reusable Second Stage*. 1969, National Aeronautics and Space Administration: Cleveland, Ohio.
20. Paull, A., *Scramjet testing in the T3 and T4 hypersonic impulse facilities.* Scramjet propulsion /, 2000. **189**: p. 1-46.
21. Stalker, R.J., et al., *Scramjets and shock tunnels—The Queensland experience.* Progress in Aerospace Sciences, 2005. **41**(6): p. 471-513.
22. Juliano, T.J., D. Adamczak, and R.L. Kimmel, *HIFiRE-5 Flight Test Results.* Journal of Spacecraft and Rockets, 2015. **52**(3): p. 650-663.
23. Peebles, C. and N. Allen, *Eleven seconds into the unknown : a history of the hyper-X program / Curtis Peebles / Ned Allen, eitor-in-chief*, ed. ProQuest. 2011, Reston, VA: Reston, VA : American Institute of Aeronautics and Astronautics.
24. Dornheim, M., *A Breath of Fast Air. Flight test of scramjet airframe/engine combination shows thrust is greater than drag.* Aviation Week & Space Technology, 2004. **160**(14): p. 28-29.
25. Bouchez, M., et al., *French-Russian Partnership on Hypersonic Wide-Range Ramjets.* Journal of Propulsion and Power, 2001. **17**(6): p. 1177-1183.
26. Hallion, R.P., et al., *The Hypersonic Revolution. Volume 2. From Scramjet to the National Aero-Space Plane*, O.H. Aeronautical Systems Center Wright-Patterson Afb, Editor. 1995.
27. Heiser, W.H. and D.T. Pratt, *Hypersonic airbreathing propulsion / William H. Heiser, David T. Pratt with Daniel H. Daley and Unmeel B. Mehta*. 1994, Washington, D.C.: Washington, D.C. : American Institute of Aeronautics and Astronautics.
28. Razzaqi, S., *Oxygen Enrichment in a Hydrogen Fuelled Scramjet*. 2011, The University of Queensland, School of Mechanical and Mining Engineering.
29. *HRE - Hypersonic Research Engine*. 2017; Available from: https://hapb-www.larc.nasa.gov/Public/Engines/Hre/Hre.html.
30. Goebel, T.P., V.V. Vancamp, and W.R. Hartill, *Study of hypersonic propulsion/airframe integration technology - NASA-CR-145321*. 1978.
31. Henry, J.R. and G.Y. Anderson, *Design considerations for the airframe-integrated scramjet - NASA-TM-X-2895*. 1973, Sponsoring Organization: NASA Langley Research Center.
32. Hartill, W.B., *Analytical and Experimental Investigation of a Scramjet Inlet of Quadriform Shape*, U.S.A. Force, Editor. 1965, Marquardt Corp.
33. Kiersey, J.L., Snow, M. L., *Modular Inlet Investigation*, in *Aeronautics Div., Research and Development, Applied Physics Lab.,*. 1966, Johns Hopkins Univ.: Baltimore, MD.
34. Kutshenreuter, P.H., *Hypersonic Inlet Tests in Helium and Air*, in *AIAA Propulsion Joint Specialist Conf.* 1965: U. S. Air Force Academy, CO.
35. Simmons, J.M., Weidner, E. H., *Design of Scramjet Inlets with Rectangular to Circular Shape Transition*. 1986, NASA.
36. *Hyper-X ED97-43968-2: Hyper-X Research Vehicle - Artist Concept in Flight*. 2017; Available from: https://www.dfrc.nasa.gov/Gallery/Photo/X-43A/HTML/ED97-43968-2.html.
37. *Making their Mach*. 2017; Available from: https://www.eait.uq.edu.au/making-their-mach.
38. Ding, F., et al., *Influence of surface pressure distribution of basic flow field on shape and performance of waverider.* Acta Astronautica, 2015. **108**: p. 62.

39. Maikapar, G., *Comments on the choice of waverider shape.* Fluid Dynamics, 1996. **31**(3): p. 443-447.
40. Heinze, W. and A. Bardenhagen, *Waverider Aerodynamics and Preliminary Design for Two-Stage-to-Orbit Missions, Part 2.* Journal of Spacecraft and Rockets, 1998. **35**(4): p. 459-466.
41. Maikapar, G., *Waveriders of complicated shape.* Fluid Dynamics, 1998. **33**(4): p. 598-603.
42. Paull, A., R.J. Stalker, and D.J. Mee, *Experiments on supersonic combustion ramjet propulsion in a shock tunnel.* J. Fluid. Mech., 1995. **296**(-1): p. 159-183.
43. Trexler, C.A. and S.W. Souders, *Design and performance at a local Mach number of 6 of an inlet for an integrated Scramjet concept - NASA-TN-D-7944*. 1975, Sponsoring Organization: NASA Langley Research Center.
44. Kumar, A., *Three-Dimensional Inviscid Analysis of the Scramjet Inlet Flowfield.* Journal of Aircraft, 1982. **19**(10): p. 892-893.
45. Sun, B., et al., *Investigation on a streamtraced hypersonic Busemann inlet.* Proceedings of the Institution of Mechanical Engineers, Part G: Journal of Aerospace Engineering, 2010. **224**(1): p. 57-63.
46. Sun, B. and K.Y. Zhang, *Preliminary investigation on Busemann inlet starting characteristics*. Vol. 27. 2006. 128-131.
47. Ferri, A., *Review of problems in application of supersonic combustion.* International Organization, 1977.
48. Denman, Z.J., et al., *Ignition experiments of hydrocarbons in a Mach 8 shape-transitioning scramjet engine.* Journal of Propulsion and Power, 2016. **32**(6): p. 1462-1471.
49. El-Sayed, A.F., *Fundamentals of Aircraft and Rocket Propulsion by Ahmed F. El-Sayed*, ed. SpringerLink. 2016: London : Springer London : Imprint: Springer.
50. Nelson, E.S., G.J. Harloff, and H.T. Lai, *Two-dimensional viscous flow computations of hypersonic scramjet nozzle flowfields at design and off-design conditions - NASA-CR-182150*. 1988.
51. Ferri, A., *Mixing-Controlled Supersonic Combustion.* Annu. Rev. Fluid. Mech., 1973. **5**(1): p. 301-338.
52. Bricalli, M.G., *Numerical study into thermal-compression scramjets*. 2015, The University of Queensland, School of Mechanical and Mining Engineering.
53. Billig, F.S., M. Lasky, and R.C. Orth, *Effects of thermal compression on the performance estimates of hypersonic ramjets.* Journal of Spacecraft and Rockets, 1968. **5**(9): p. 1076-1081.
54. *National Aero-Space Plane: A Need for Program Direction and Funding Decisions*. 1993.
55. Li, N., K.Y. Zhang, and J.L. Xu, *Simulation and experiment validation of a two-dimensional asymmetric ramp nozzle.* Hangkong Dongli Xuebao/Journal of Aerospace Power, 2004. **19**(6): p. 802-805.
56. Wang, C., K. Zhang, and K. Cheng, *Effects of incoming flow asymmetry on shock train structures in constant-area isolators.* Transactions of Nanjing University of Aeronautics and Astronautics, 2006. **23**(1): p. 1-7.
57. Wang, C.P., K.Y. Zhang, and K.M. Cheng. *Pressure distribution measurements in scramjet isolators under asymmetric supersonic flow*. in *Collection of Technical Papers - 44th AIAA Aerospace Sciences Meeting*. 2006.

58. Yang, W., et al. *Effects of forebody models and internal flow supplying methods on an experimental study of a scramjet asymmetric nozzle*. in *Proceedings of 2010 Asia-Pacific International Symposium on Aerospace Technology, APISAT 2010*. 2010.
59. Fu, L., S. Zhang, and Y. Zheng, *Performances analysis of asymmetric minimum length nozzles.* International Journal of Modeling, Simulation, and Scientific Computing, 2016. **7**(2).
60. Lee, J., *Into the wind: A history of the American wind tunnel, 1896–1941*, J.R. Hansen, Editor. 2001, ProQuest Dissertations Publishing.
61. Shlien, D.J., *The Wright Brothers as design engineers*. 2000. p. 6297-6303.
62. Dodson, M.G. and D.S. Miklosovic, *An Historical and Applied Aerodynamic Study of the Wright Brothers' Wind Tunnel Test Program and Application to Successful Manned Flight.* 2005(41987): p. 269-278.
63. Galison, P. and A. Roland, *Atmospheric Flight in the Twentieth Century*, ed. P. SpringerLink Content. 2000: Dordrecht : Springer Netherlands : Imprint: Springer.
64. Hirsch, C., *Numerical computation of internal and external flows : fundamentals of computational fluid dynamics / Charles Hirsch*. 2nd ed.. ed. Numerical computation of internal & external flows. 2007, Burlington, MA: Burlington, MA : Elsevier/Butterworth-Heinemann.
65. Johnson, F.T., E.N. Tinoco, and N.J. Yu, *Thirty years of development and application of CFD at Boeing Commercial Airplanes, Seattle.* Computers and Fluids, 2005. **34**(10): p. 1115-1151.
66. Knight, D., et al., *Assessment of CFD capability for prediction of hypersonic shock interactions.* Progress in Aerospace Sciences, 2012. **48-49**: p. 8-26.
67. Morrison, D.C., *Testing the limits at Mach 25. (hypersonic aerospace plane).* Science, 1988. **240**(4855): p. 973.
68. *CATIA*. 2017; Available from: https://www.3ds.com/products-services/catia/.
69. *Mesh Generation Software for CFD - Pointwise*. 2017; Available from: http://www.pointwise.com/.
70. *Why is CATIA an industry leader?* 2017; Available from: http://www.intrinsys.com/software/catia/industry-leader.
71. Foster, S. and D. Halbstein, *Integrating 3D Modeling, Photogrammetry and Design*. SpringerBriefs in Computer Science. 2014, London: London : Springer.
72. Cheng, S.-W., *Delaunay mesh generation*, ed. T.K. Dey and J. Shewchuk. 2013, Boca Raton: Boca Raton : CRC Press.
73. Anonymous, *The CAD/CAM Hall of Fame.* American Machinist, 1998. **142**(11): p. 110.
74. Waurzyniak, P., *Masters OF MANUFACTURING Patrick J. Hanratty.* Manufacturing Engineering, 2010. **145**(1): p. 39-45.
75. Sutherland, I.E., *Sketchpad: A Man-Machine Graphical Communication System*, L.A.B. Massachusetts Inst Of Tech Lexington Lincoln, Editor. 1963.
76. Fetter, *A Progression of Human Figures Simulated by Computer Graphics.* Computer Graphics and Applications, IEEE, 1982. **2**(9): p. 9-13.
77. *Photogrammetry*. 2014.
78. Gruen, A., *Scientific-technological developments in photogrammetry and remote sensing between 2004 and 2008*, in *Advances in Photogrammetry, Remote Sensing and Spatial Information Sciences*. 2008, CRC Press. p. 21-25.
79. El-Hakim, S., *3-D Data modelling and visualization*, in *Advances in Photogrammetry, Remote Sensing and Spatial Information Sciences*. 2008, CRC Press. p. 311-322.

80. Kaufman, J., M. Clement, and A.E.W. Rennie, *Reverse Engineering Using Close Range Photogrammetry for Additive Manufactured Reproduction of Egyptian Artifacts and Other Objets d'art2.* Journal of Computing and Information Science in Engineering, 2015. **15**(1): p. 011006-011006-7.
81. Canevese, E. and T. De Gottardo, *Beyond Point Clouds and Virtual Reality: Innovative Methods and Technologies for the Protection and Promotion of Cultural Heritage* 2017, Copernicus GmbH: Gottingen. p. 685-691.
82. Blaya, F., et al., *Aplicación de la digitalización para el estudio, conservación y explotación turística del patrimonio: un caso práctico de un conjunto de bodegas subterráneas - declaradas Bien de Interés Cultural (BIC) 1/Scanning application for the study, preservation and exploitation of heritage tourism: a case study of a set of underground cellars - declared Spanish good of cultural interest (BIC).* Arte, Individuo y Sociedad, 2017. **29**(1): p. 163-176.
83. Baiocchi, V., et al., *Augusto's sundial: Image-based modeling for reverse engeneering purposes*. 2017. p. 63-69.
84. Martorelli, M., P. Ausiello, and R. Morrone, *A new method to assess the accuracy of a Cone Beam Computed Tomography scanner by using a non-contact reverse engineering technique.* Journal of Dentistry, 2014. **42**(4): p. 460-465.
85. Giordano, M., P. Ausiello, and M. Martorelli, *Accuracy evaluation of surgical guides in implant dentistry by non-contact reverse engineering techniques.* Dental Materials, 2012. **28**(9): p. e178-e185.
86. Galantucci, L.M., M. Pesce, and F. Lavecchia, *A stereo photogrammetry scanning methodology, for precise and accurate 3D digitization of small parts with sub-millimeter sized features.* CIRP Annals - Manufacturing Technology, 2015. **64**(1): p. 507-510.
87. *Reverse engineering software (RESURF)- mesh or point cloud to NURBS surface*. 2017; Available from: http://www.resurf3d.com/index.htm.
88. *3DReshaper (Home)*. 2017; Available from: https://www.3dreshaper.com/en/software-en/.
89. Klette, R., *Concise Computer Vision: An Introduction into Theory and Algorithms*. An Introduction into Theory and Algorithms. 2014, London: Springer London, London.
90. Marr, D., S. Ullman, and T. Poggio, *Vision: A Computational Investigation into the Human Representation and Processing of Visual Information*. 2010: MIT Press.
91. Roberts, L., *Machine Perception of Three-Dimensional Solids*, in *Electrical Engineering*. 1963, Massachusetts Institute of Technology.
92. Marr, D., *REPRESENTING AND COMPUTING VISUAL INFORMATION.* Energy Technology Review, 1979. **2**: p. 15-80.
93. Saha, S., *Design methodology for embedded computer vision systems*, S.S. Bhattacharyya, Editor. 2007, ProQuest Dissertations Publishing.
94. Frederick, C.O., Y.C. Wong, and F.W. Edge, *Two-dimensional automatic mesh generation for structural analysis.* International Journal for Numerical Methods in Engineering, 1970. **2**(1): p. 133-144.
95. George, A., *Nested Dissection of a Regular Finite Element Mesh.* SIAM Journal on Numerical Analysis, 1973. **10**(2): p. 345-363.
96. Frey, W.H. and D.A. Field, *Mesh relaxation: A new technique for improving triangulations.* International Journal for Numerical Methods in Engineering, 1991. **31**(6): p. 1121-1133.

97. DeRose, T., M. Kass, and T. Truong, *Subdivision surfaces in character animation*, in *Proceedings of the 25th annual conference on Computer graphics and interactive techniques*. 1998, ACM. p. 85-94.
98. *Modelling techniques – limitations of different surface types*. 2012 2012-12-03; Available from: https://carolamadio.wordpress.com/2012/12/03/modelling-techniques-limitations-of-different-surface-types/.
99. Piegl, L.A. and W. Tiller, *The NURBS book*. Second Edition.. ed. NURBS book, ed. SpringerLink. 1997: Berlin, Heidelberg : Springer Berlin Heidelberg : Imprint: Springer.
100. *Blender Manual: Introduction*. 2017; Available from: https://docs.blender.org/manual/en/dev/modeling/introduction.html.
101. *Rhinoceros*. 2017; Available from: https://www.rhino3d.com/.
102. autodesk, *Maya | Computer Animation & Modelling Software | Autodesk.* 2017.
103. Zhang, H. and Q. Shen, *Analysis of boundary layer parameters about hypersonic 2D blunt wedge*. Vol. 33. 2015. 259-265.
104. anatollocker, *22 Best 3D Modeling Software Tools (3D Design/3D CAD Software) | All3DP.* 2017.
105. *Finding the Right 3D Modeling Software For You | MatterHackers*. 2017; Available from: https://www.matterhackers.com/articles/finding-the-right-3d-modeling-software-for-you.
106. G2Crowd, *Best 3D Modeling Software in 2017 | G2 Crowd.* 2017.
107. *Top 20: Most Popular 3D Modeling & Design Software for 3D Printing (2017 Update)*. 2017 2017-05-09; Available from: https://i.materialise.com/blog/top-25-most-popular-3d-modeling-design-software-for-3d-printing/.
108. *Slant - 16 best 3D modeling software as of 2017*. 2017; Available from: https://www.slant.co/topics/1559/~3d-modeling-software.
109. *15 Best Tools for 3D Modeling Software – Joanna Ngai – Medium*. 2016 2016-12-19; Available from: https://medium.com/@ngai.yt/15-best-tools-for-3d-modeling-software-a7939fded451.
110. *10 best free 3D design software*. 2016 2016-11-09; Available from: http://windowsreport.com/free-3d-design-software/.
111. Gollan, P.A.J.R.J., *The User's Guide to the Eilmer4 Flow Simulation Program*. 2016, The University of Queenaldn: School of Mechanical and Mining Engineering.

Appendix A: diffuser_H.lua

```
-- Author: Rowan J. Gollan

-- Date: 18-Jun-2015
-- Place: Poquoson, Virginia, USA

gas = {
   R = 287.1,
   gamma = 1.4
}

inflow = {
   M = 7.74,
   p = 2374, -- Pa
   T = 376.1 -- K
}

diffuser = {
   M2 = 5.909999999,
   M3 = 5.37,
   lip = 4.7,
   r_cbody = 0.0
}
```

Appendix B: Diffuser Characteristics

```
Reading input from file:    diffuser_H.lua
Computing diffuser.
---------------------------------
Properties of the ideal diffuser:
M2 =    5.909999999
M3 =    5.3700320079843
beta =  12.535974975569
theta_s =   8.5119376625032
M1 =    9.2167856921557
pr =    39.332741657197
---------------------------------
Truncating diffuser wall.
Now computing flow through truncated Busemann diffuser
using Seagull.
  number of planes plotted              = 493
  number of times discontinuity plotted = 486
------------------------------
-- Diffuser characteristics --
------------------------------

pressure ratio =    17.009409
temperature ratio = 2.353651
average Mach number at throat = 4.751610
average Mach number at cowl closure =   5.711696
total pressure ratio =  0.850381
kinetic energy efficiency =     0.996044
x_cc =          4.473040
x_th =          6.327290
CRT =           6.764032
CRI =           2.084991
```

Appendix C: `inlet.lua`

```
-- A dummy input file so that we can use the Stile tools.
-- We just list the minimum information here so that the
-- viscous correction can be applied.

gas = {
  R = 287.1,
  gamma = 1.4
}

inflow = {
  M = 9.1113,
  p = 2247.4,
  T = 372.44
}

inlet = {
   nt = 30,
   ns = 30,
   nb = 30,
   -- We just include the throat to keep the tools happy
   throat = {
      aspect_ratio = 1.75
   },
   exit = 7.0

}

viscous_correction = {
   R0 = 1.0,
}

smoothing = {
   method = 'filter',
   steps = 20,
   l_dirn = true,
   c_dirn = true,
   nfixed_l = 1,
   nfixed_c = 1,
   nmin_c = 5
}
```

Appendix D: diffuser_L.lua

```
-- Author: Rowan J. Gollan
-- Date: 18-Jun-2015
-- Place: Poquoson, Virginia, USA

gas = {
   R = 287.1,
   gamma = 1.4
}

inflow = {
   M = 7.74,
   p = 2374, -- Pa
   T = 376.1 -- K
}

diffuser = {
   M2 = 5.87,
   M3 = 5.39,
   lip = 4.7,
   r_cbody = 0.0
}
```

Output:

```
Reading input from file:    diffuser_L.lua
Computing diffuser.
---------------------------------
Properties of the ideal diffuser:
M2 =    5.87
M3 =    5.3900247970444
beta =  12.284592981991
theta_s =   8.6777199159505
M1 =    8.8109944259263
pr =    28.380970126753
---------------------------------

Truncating diffuser wall.
Now computing flow through truncated Busemann diffuser
using Seagull.
  number of planes plotted              = 469
  number of times discontinuity plotted = 462
------------------------------
-- Diffuser characteristics --
------------------------------
pressure ratio =    11.903563
temperature ratio = 2.125842
average Mach number at throat = 5.048491
average Mach number at cowl closure =   5.808419
total pressure ratio =  0.845390
kinetic energy efficiency =     0.995897
x_cc =          4.520701
x_th =          6.578413
CRT =           5.289116
CRI =           1.742001
```

Appendix E: propertiesLC.txt

```
-------------------------------------------------------------
Properties of inlet (all values non-dimensional) [*]
-------------------------------------------------------------
Positions:
Inlet start:                0.214590
Cowl closure:               4.528362
Throat:                   6.386168
Inlet exit:               7.000000

Lengths:
Inlet length:               6.785410
Isolator length:            0.613832

Widths:
Capture width (full):           0.000000

Areas:
Capture area (full):            1.208793
Cowl closure area (full):       0.392738
Throat area (full):         0.208147
Internal wetted area (full):       14.187341

Contraction ratios
Total contraction ratio:        5.807409
Internal contraction ratio:     1.886831

-------------------------------------------------------------
[*] Positions, lengths and widths are normalised by R0.
    Areas are normalised by R0^2.
```

Appendix F: Scaling Script

* Script written by R. Gollan (2017)

```
   -- Transform the collection of lines
   sA = 0.183360/0.208362
   sL = sqrt(sA)
   DX = 6.477429 - sL*6.390993
   print("sL= ", sL, " DX= ", DX)
   transformedLines = {}
   local c_pts = {} -- start an empty table to collect starting points
in
   for i,line in ipairs(streamlines) do
      local function udf(x)
     local Xorig = (x-DX)/sL
     local fd = copy(line:get_flow_data(Xorig))
     fd.pos.x = sL*fd.pos.x + DX
     fd.pos.y = sL*fd.pos.y
     fd.pos.z = sL*fd.pos.z
     return fd
      end
      transformedLines[#transformedLines+1] = User_defined_line(udf,
sL*line:vstart().x + DX, sL*line:vfinish().x + DX)
      c_pts[#c_pts+1] = transformedLines[#transformedLines]:vstart()
      print("s-pt= ", c_pts[#c_pts].x)
   end

   -- Location of cowl closure is the start of the last streamline
   local x_cc = transformedLines[#transformedLines]:vstart().x
```

Appendix G: Software Decision Matrix

	Features (3)	Smoothing (2)	Pointwise® (3)	Linux (1)	Scriptable (2)	NURBS (2)	Cost (2)	Total
Blender™	2	1	0	2	2		2	28
Maya®	2	2		0	2		1	27
Meshmixer	1	2		2	1		2	27
3ds Max®	2	2		0	1		1	26
Rhinoceros®	2	2		0	2		0	26
Onshape	1	1		2	1		0	21
Moment of Inspiration	2			0	0		1	20
ZBrush	1	1		0	1		0	19
SketchUp	1	1		0	1		1	15
MeshLab		2	2	2			2	8
AutoCAD®	2	0		0			1	3
CATIA™	2	0	2	0			1	5
FreeCAD				2	2		2	6
Fusion™	1	1	0	0			1	3
Inventor®	2	0		0			1	3
Mudbox®	1	1	0	0			1	6
OpenSCAD	0	0	2	2	2		2	8
Sculptris			0	0			2	2
Solidworks®	2	0		0			1	3
3DReshaper®	0	2	0			2	1	5

2 – Meets requirement well	1 – Somewhat meets requirement	0 – Does not meet requirement	Unknown

** The number in parentheses represents the weighting factor relevant to the feature.

Appendix H: Conical Forebody Dimensions

```
==============
Notes on files
==============
:Author: Rowan J. Gollan
:Date: 2017-03-13

This directory contains files that can be used to build
a crest inlet surface in Catia.

Details of cone geometry
------------------------

half-angle : 5 degrees
nose radius: 5 mm

virtual apex of cone (w.r.t inlet coordinates)
-15.32737343, 0.74, 0
x = -9638.3 mm
y = 465.3 mm

inlet centerline attachment point
x = 891.5 mm
y = 465.3 mm

NOTE: In the frame of the inlet coordinates, the cone has one edge that
      lies in the x-axis direction. The axis of the cone is at 5 degrees
      to the horizontal.

Inlet arrangement
-----------------
This design accommodates four inlets arranged on the underside of the
vehicle.

Inlet cutback
-------------
Cowl to be cut back to give an internal contraction ratio of 1.7.

Surface for CFD
---------------
One full inlet with one sidewall arranged vertically -- will need to
rotate inlet geometry by 22.5 degrees.
```

Appendix I: Blender™ Automation Script

```
#construct_vehicle.py
# -*- coding: utf-8 -*-
"""
Created on Tue Jun  6 10:17:06 2017
By Reid Jones
"""

#import bpy
from math import sin, cos, tan, radians, degrees, pi
#import mathutils

################################################################################
##########                              INPUTS                          ##########
################################################################################
scale = 1000

x_virt_apex = 15.32737343/scale # dist of truncated end from virtual
apex (mm)
y_virt_apex = 0.74/scale    # dist of truncated end from virtual apex
(mm)

r2 = 5.0/scale              # Radius of cone front truncated tip (mm)
theta = 5                       # Half angle (deg)
r0 = r2/cos(radians(theta))     # Radius of blunt tip slice point (mm)
L0 = r2*tan(radians(theta))     # Length of slice point from truncated
end (mm)
L = 9638.3/scale                # Length of cone
r1 = (L)*tan(radians(5))  # Radius of cone rear (mm)

# Inlet centerline attachment point
x = 891.5/scale         # x dist of cowl closure from virtual apex (mm)
y = 0                   # y dist of cowl closure from virtual apex (mm)
z = 465.3/scale         # z dist of cowl closure from virtual apex (mm)

################################################################################
##########                   GEOMETRY CREATION                  ##########
################################################################################
#-----------------------    Build forebody geometry    ------------------
# Cone
bpy.ops.mesh.primitive_cone_add(vertices=1000, radius1=r1, radius2=r2,
depth=L,\
location=(0,0,0))
bpy.ops.transform.rotate(value=(-pi/2), axis=(0,1,0))
bpy.data.objects["Cone"].location = ((x_virt_apex + L/2 + r2), 0, 0)

# Blunt tip
bpy.ops.mesh.primitive_uv_sphere_add(segments=128, ring_count=128,
size=r0, \
location=((x_virt_apex + r0 + L0),0,0))

bpy.ops.object.select_all(action='DESELECT')

#-----------------------    Import inlet .stl file    ------------------
```

```
bpy.ops.import_mesh.stl(filepath="R://Reid//Documents//Uni//MECH4500//\
Point_Clouds//Spartan_STL//spartan-low-ICR.stl")

sphere = ["SurfSphere"]
cone = ["Cone"]
inlet = ["spartan-low-ICR"]

#----------------------------    Rotate inlet    ----------------------
bpy.ops.transform.rotate(value=(pi/2), axis=(1,0,0))
bpy.ops.transform.rotate(value=(radians(8.8)), axis=(0,1,0))

#----------------------------    Translate inlet    --------------------
# To find the index number of the vertex at the centreline attachment
point,
# un-comment the following:
#current_object = bpy.context.active_object
#[i.index for i in current_object.data.vertices if i.select]
#-------------------------------------------------------------------------

bpy.data.objects["spartan-low-ICR"].location = (x_virt_apex + x + L/2,
0, -2*z)

#########################################################################
##########                    MODIFICATIONS                    ##########
#########################################################################
#--------------------    Add inlet surface thickness    ----------------
bpy.ops.object.modifier_add(type='SOLIDIFY')
bpy.context.object.modifiers["Solidify"].offset = 1.0
bpy.context.object.modifiers["Solidify"].thickness_clamp = 2.0
bpy.context.object.modifiers["Solidify"].thickness = 0.002
bpy.context.object.modifiers["Solidify"].use_quality_normals = True
bpy.context.object.modifiers["Solidify"].use_rim = True
bpy.ops.object.modifier_apply(apply_as='DATA', modifier="Solidify")

#------------------------    Mirror inlet geometry    -----------------
bpy.ops.object.modifier_add(type='MIRROR')
bpy.context.object.modifiers["Mirror"].use_x = False
bpy.context.object.modifiers["Mirror"].use_y = False
bpy.context.object.modifiers["Mirror"].use_z = True
bpy.context.object.modifiers["Mirror"].use_mirror_vertex_groups = False
bpy.context.object.modifiers["Mirror"].use_mirror_merge = 0
bpy.ops.object.modifier_apply(apply_as='DATA', modifier="Mirror")

bpy.ops.object.join()

bpy.ops.export_mesh.stl(filepath="R://Reid//Documents//Uni//MECH4500//\
Point_Clouds//Spartan_STL//Blender_Exports//vehicle_body.stl")
```

Appendix J: 3D Unstructured Grid for CFD

* Grid generation and images courtesy of J. Kunze.

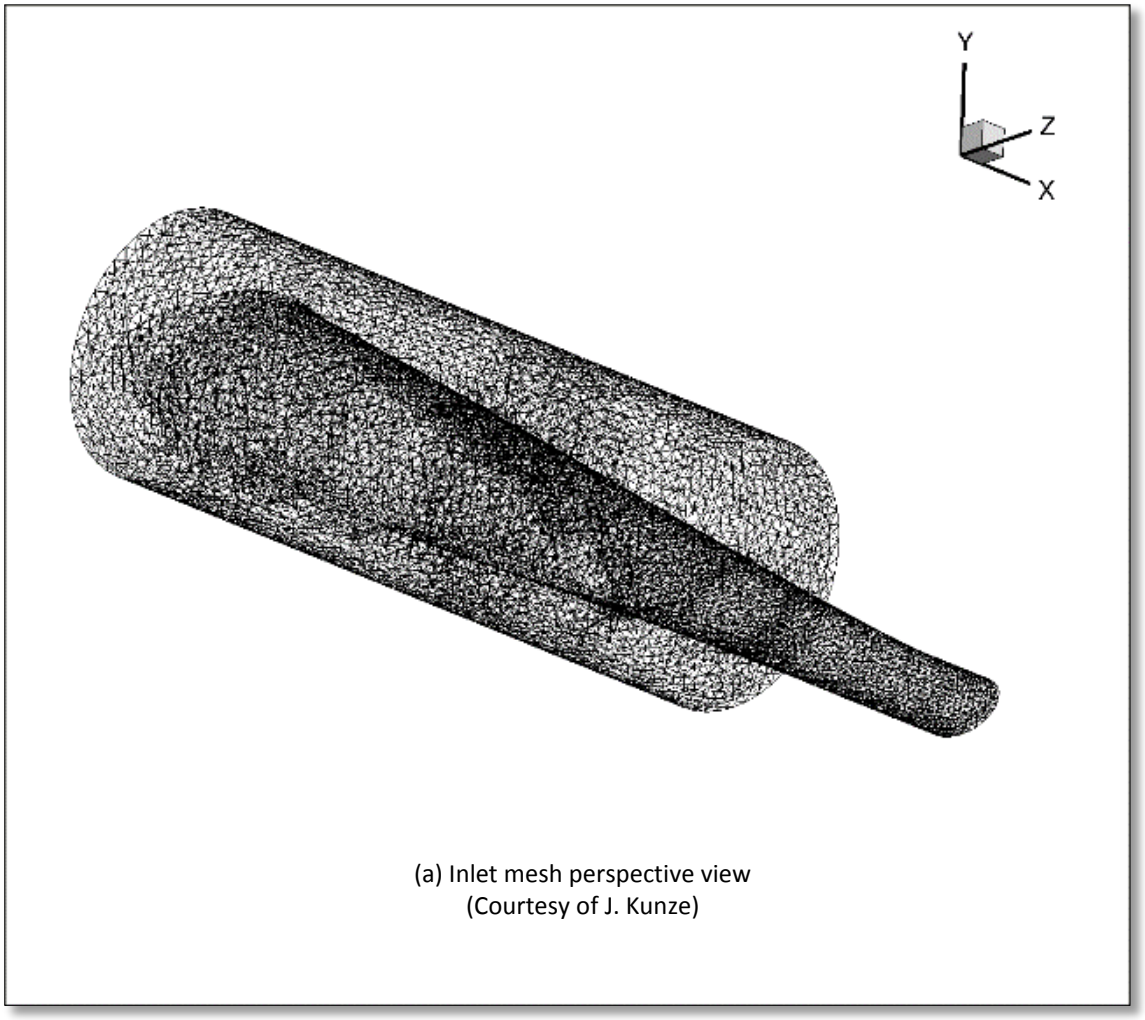

(a) Inlet mesh perspective view
(Courtesy of J. Kunze)

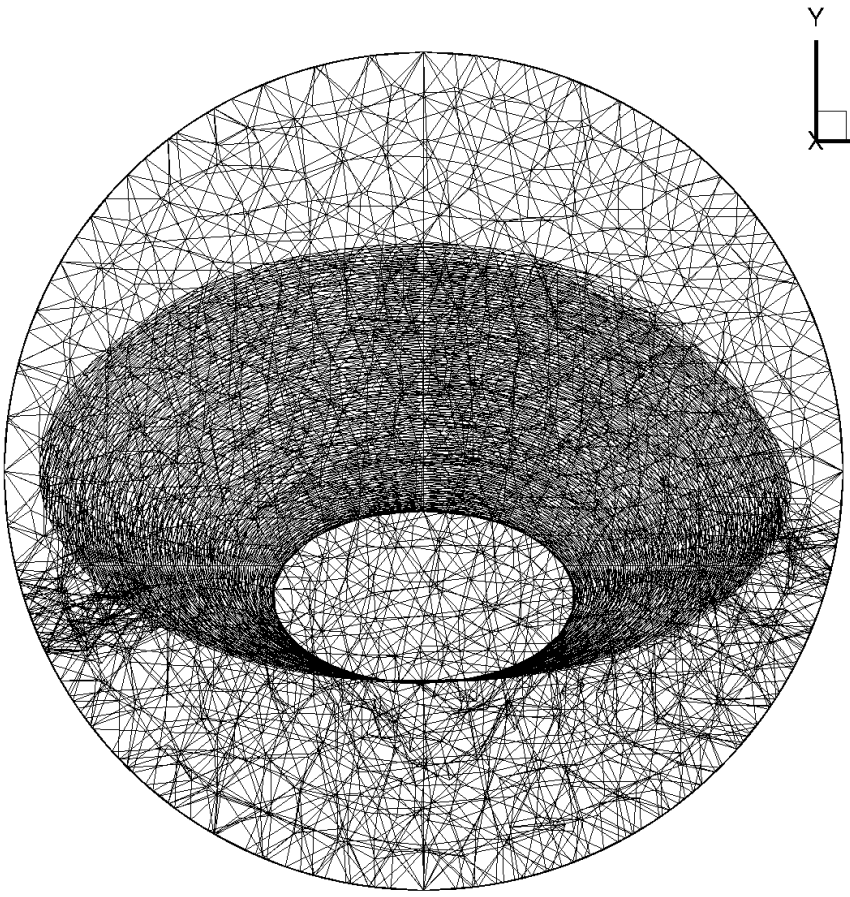

(b) Inlet mesh front view (Courtesy of J. Kunze)

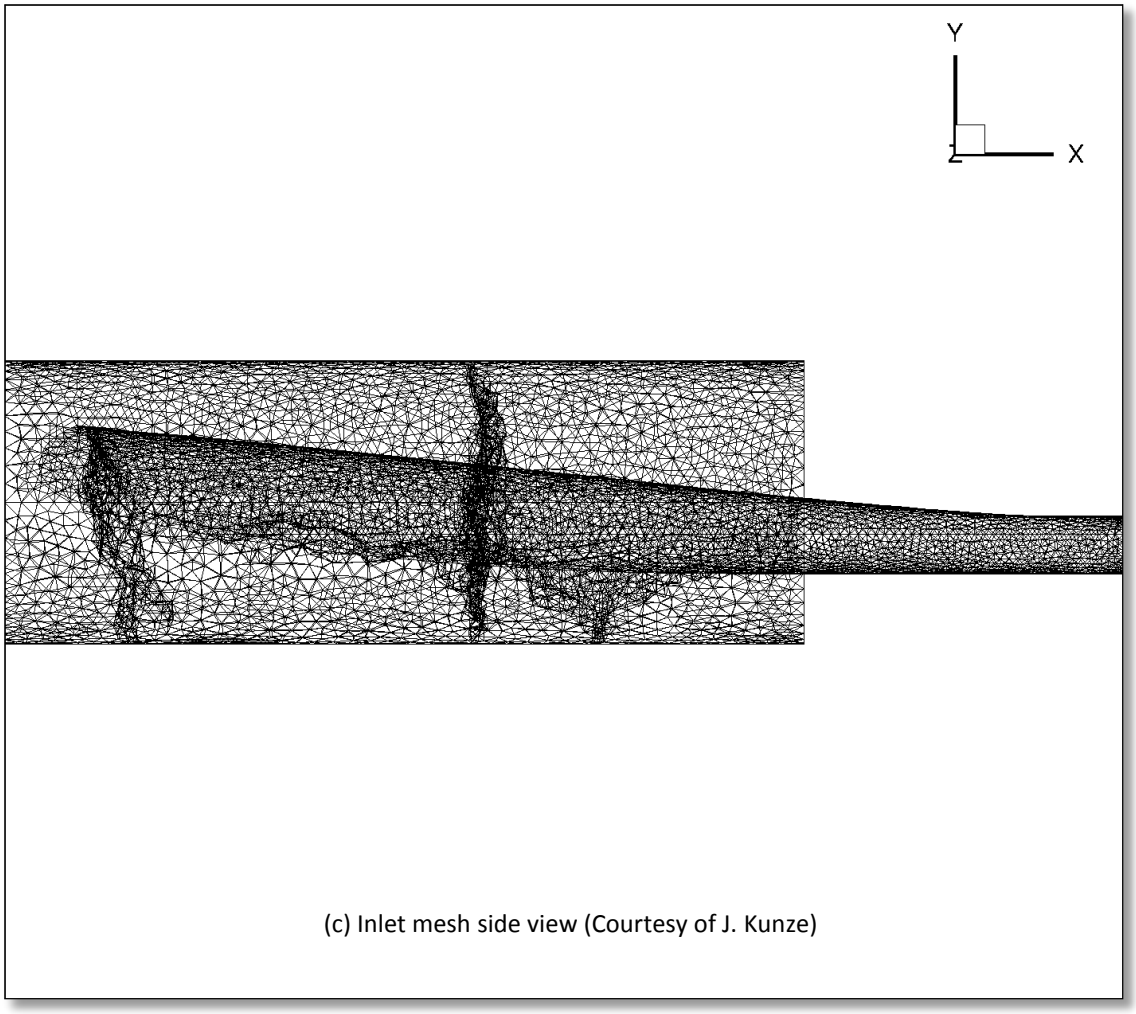

(c) Inlet mesh side view (Courtesy of J. Kunze)